

# **Photo-induced charge generation in mono- and bimetallic nanoparticles deposited on titanium dioxide**

Dissertation  
zur  
Erlangung des akademischen Grades  
doctor rerum naturalium (Dr. rer. nat.)  
der Mathematisch- Naturwissenschaftlichen Fakultät  
der Universität Rostock

vorgelegt von  
Sandra Peglow  
aus Greifswald

Rostock, May 18, 2018

**Gutachter:**

1. Gutachter:

Professor Dr. Stefan Lochbrunner  
Institut für Physik, Universität Rostock

2. Gutachter:

Dr. Volker Brüser  
Leibniz-Institut für Plasmaforschung und Technologie e.V., Greifswald

3. Gutachter:

Professor Dr. Holger Kersten  
Institut für Experimentelle und Angewandte Physik, Christian-Albrechts-Universität zu  
Kiel

**Datum der Einreichung:** 21.11.2017

**Datum der Verteidigung:** 27.04.2018



## Contents

<b>1</b>	<b>Introduction</b>	<b>1</b>
<b>2</b>	<b>Fundamentals</b>	<b>4</b>
2.1	Localized surface plasmon resonance . . . . .	4
2.1.1	History and scientific description of nanoparticles . . . . .	4
2.1.2	Localized surface plasmons . . . . .	4
2.1.3	Quasi-static approximation . . . . .	6
2.1.4	Mie theory . . . . .	7
2.1.5	Nanoparticle size . . . . .	8
2.1.6	Nanoparticle shape . . . . .	9
2.1.7	Bimetallic nanoparticle-influence of material composition . . . . .	10
2.1.8	Dielectric constant of surrounding medium . . . . .	10
2.1.9	Plasmon coupling . . . . .	10
2.2	Plasmon-induced energy transfer . . . . .	11
2.2.1	Hot electron injection . . . . .	12
2.2.2	Near-field enhancement . . . . .	13
2.2.3	Nanoparticle scattering . . . . .	13
2.3	Metal and semiconductor materials . . . . .	14
2.3.1	TiO <sub>2</sub> . . . . .	14
2.3.2	Drude-Sommerfeld Theory . . . . .	14
2.3.3	Au and Ag nanoparticles . . . . .	15
2.4	Plasma . . . . .	15
2.4.1	General plasma properties . . . . .	15
2.4.2	Plasma frequency . . . . .	16
2.4.3	Motion of charged particle in magnetic and electric field . . . . .	17
2.4.4	Magnetron sputtering . . . . .	18
2.5	Thin film deposition, growth and nanostructure formation . . . . .	19
2.5.1	Thin film growth modes . . . . .	19
2.5.2	Structure zone model . . . . .	20
2.5.3	Solid state dewetting . . . . .	21

<b>3</b>	<b>Literature Study</b>	<b>23</b>
3.1	Au nanoparticles preparation . . . . .	23
3.1.1	Deposition . . . . .	23
3.1.2	Annealing . . . . .	24
3.1.3	Facetting . . . . .	24
3.2	Localized surface plasmon resonance . . . . .	24
3.2.1	Increase in Au loading . . . . .	25
3.2.2	Influence of titania . . . . .	25
3.2.3	Non-spherical shape . . . . .	26
3.3	Bimetallic Au-Ag nanoparticles . . . . .	26
3.4	Photocatalysis and photoelectrochemistry . . . . .	28
3.4.1	Mechanism . . . . .	28
3.4.2	Hot electron injection . . . . .	30
3.4.3	Electric field enhancement . . . . .	30
3.4.4	Catalytic effect of metal nanoparticles . . . . .	31
3.4.5	Photoelectrochemical characteristic . . . . .	32
<b>4</b>	<b>Experimental</b>	<b>33</b>
4.1	Material and methods . . . . .	33
4.1.1	Magnetron sputter recipient . . . . .	33
4.1.2	Tube furnace . . . . .	34
4.1.3	Substrates . . . . .	34
4.2	Sample preparation . . . . .	36
4.2.1	Preparation of Au nanoparticles on TiO <sub>2</sub> . . . . .	36
4.2.2	Bimetallic Au-Ag nanoparticles . . . . .	36
4.2.3	Au nanoparticles on spincoating TiO <sub>2</sub> . . . . .	37
4.2.4	Variation in thermal annealing parameter . . . . .	37
4.2.5	Au nanoparticles on atmospheric pressure chemical vapor deposition (AP-CVD) TiO <sub>2</sub> . . . . .	38
<b>5</b>	<b>Analytical methods</b>	<b>39</b>
5.1	UV-vis spectroscopy . . . . .	39
5.1.1	Basic parameters . . . . .	39
5.1.2	Set-up of the Lambda850 UV-Vis spectrometer . . . . .	39
5.1.3	Operation parameter . . . . .	41
5.2	Scanning electron microscopy (SEM) . . . . .	41
5.2.1	Acceleration voltage and wavelength of electrons . . . . .	41
5.2.2	Interaction of electrons with a specimen . . . . .	41
5.2.3	Set-up of Jeol SEM . . . . .	42
5.2.4	Operating conditions . . . . .	43
5.3	Transmission electron microscope (TEM) . . . . .	43
5.3.1	Relativistic correction for electron wavelength . . . . .	43
5.3.2	Set-up of TEM . . . . .	43
5.3.3	Dark field, bright field and contrast . . . . .	44
5.3.4	Energy dispersive spectrometer (EDS) . . . . .	44
5.3.5	Operation parameter . . . . .	44
5.4	Profilometer . . . . .	45
5.5	X-ray diffraction . . . . .	45

5.5.1	Bragg diffraction . . . . .	45
5.5.2	Set-up for Bragg-Brentano . . . . .	46
5.5.3	Operation parameter . . . . .	46
5.6	Photoelectrochemical half-cell . . . . .	46
<b>6</b>	<b>Results and discussion</b>	<b>48</b>
6.1	Au nanoparticles on TiO <sub>2</sub> . . . . .	48
6.1.1	Nanoparticle formation: magnetron sputtering-deposition and thermal annealing . . . . .	48
6.1.2	Cycling for homogenous particle growth . . . . .	52
6.1.3	Shape and size distribution on TiO <sub>2</sub> surface . . . . .	53
6.1.4	Localized surface plasmons of Au nanoparticles . . . . .	53
6.1.5	Summary: Au nanoparticles on TiO <sub>2</sub> . . . . .	58
6.2	Variation of thermal treatment . . . . .	58
6.2.1	Scanning electron microscopy . . . . .	59
6.2.2	UV-vis spectroscopy . . . . .	62
6.2.3	X-ray diffraction . . . . .	62
6.2.4	Transmission electron microscopy . . . . .	63
6.2.5	Summary: variation of thermal treatment . . . . .	63
6.3	Bimetallic Au-Ag nanoparticles . . . . .	66
6.3.1	Preparation of Au-Ag bimetallic nanoparticles . . . . .	66
6.3.2	Core-shell structure . . . . .	68
6.3.3	Plasmon excitation in core-shell particles . . . . .	68
6.3.4	Summary: bimetallic nanoparticles . . . . .	73
6.4	Photocurrent generation . . . . .	74
6.4.1	Variation of Au loading on DC sputtered TiO <sub>2</sub> . . . . .	74
6.4.2	Optimal annealing parameter for enhanced photocurrent generation . . . . .	77
6.4.3	Variation of the TiO <sub>2</sub> substrate to investigate the influence of Au/TiO <sub>2</sub> interfaces . . . . .	79
6.4.4	Photocurrent density increase by bimetallic AuAg and AgAu nanoparticles . . . . .	81
6.4.5	Decrease in photocurrent by Au decoration . . . . .	84
6.4.6	Summary: photocurrent generation . . . . .	84
<b>7</b>	<b>Conclusion</b>	<b>86</b>
<b>8</b>	<b>Acknowledgement</b>	<b>88</b>
<b>9</b>	<b>Appendix</b>	<b>106</b>
9.0.7	Uniformity and reproducibility of metal deposition . . . . .	106
9.0.8	Particle sizes of annealed Au (6.6 nm, 1) . . . . .	106
9.0.9	Reproducibility of LSPR peak position in UV-vis . . . . .	109
9.0.10	Variation in thermal annealing: transverse excitation . . . . .	110
9.0.11	Modulation in XRD . . . . .	111
9.0.12	Ag nanoparticle formation . . . . .	112
9.0.13	UV-vis spectra of Ag nanoparticles . . . . .	113
9.0.14	Optical properties of TiO <sub>2</sub> . . . . .	113
9.0.15	Cyclic voltammetry of DC sputtered TiO <sub>2</sub> . . . . .	114
9.0.16	Reflectivity of Au nanoparticles . . . . .	115
9.0.17	UV-vis absorbance of Au/AP-CVD TiO <sub>2</sub> . . . . .	116

9.0.18	Stability of sample surface . . . . .	116
9.0.19	Incident photon-to-current efficiency . . . . .	119
9.0.20	SEM of Au decorated spincoated TiO <sub>2</sub> . . . . .	119
9.0.21	Stability of photocurrent density . . . . .	120

### Acronyms and abbreviations

Notation	Description
UV	Ultraviolet
LSPR	Localized surface plasmon resonance
SEM	Scanning electron microscopy
TEM	Transmission electron microscopy
EDX	Energy dispersive X-ray spectroscopy
XRD	X-ray diffraction
PEC	Photoelectrochemical
AP-CVD	Atmospheric pressure chemical vapor deposition
ITER	International thermonuclear experimental reactor
fcc	Face centered cubic
NHE	Normal hydrogen electrode
SERS	Surface-enhanced Raman spectroscopy
NP	Nanoparticle
CB	Conduction band
UV-Vis	Ultraviolet-visible
ITO	Indium tin oxide
DC	Direct current
TOAB	Tetraoctylammonium bromide
HRTEM	High-resolution transmission electron microscopy
FWHM	Full width at half maximum
RHE	Reversible hydrogen electrode
EIS	Electrochemical impedance spectroscopy
FTO	Fluorine doped tin oxide
IPCE	Incident photon-to-current efficiency
RF	Radio frequency
PMT	Photomultiplier tube
NIR	Near-infrared

<b>STEM</b>	Scanning transmission electron microscopy
<b>HAADF</b>	High-angle annular dark-field
<b>ABF</b>	Annular bright-field
<b>BF</b>	Bright-field
<b>EELS</b>	Electron energy loss spectra
<b>SE</b>	Secondary electron
<b>SEI</b>	In-lens secondary electron detector
<b>GIXRD</b>	Grazing incident X-ray diffraction
<b>PTFE</b>	Polytetrafluorethylen
<b>SHE</b>	Standard hydrogen electrode
<b>LED</b>	Light-emitting diode
<b>OCV</b>	Open-circuit voltage
<b>CV</b>	Cyclic voltammetry
<b>SCE</b>	Saturated calomel electrode
<b>RH</b>	Rapid heating

## Symbols

Symbol	Description
$R_p$	Particle radius
$r$	Distance from the particle center (such that $r = R_p$ describes the particles surface)
$\epsilon(\omega)$	Dielectric function of the nanoparticle
$\epsilon_m$	Dielectric constant of the medium
$P_l(\cos \theta)$	Legendre polynomial of the order $l$
$l$	Polynomial order
$\theta$	Angle between the vector $r$ and the $z$ -axis
$A_l$	Coefficient determined by boundary conditions
$B_l$	Coefficient determined by boundary conditions
$C_l$	Coefficient determined by boundary conditions
$\Phi_{out}$	Potential outside of the particle
$\Phi_{in}$	Potential inside of the particle
$E_0$	Incident electric field
$\mathbf{p}$	Dipole moment
$\alpha$	Polarizability
$n$	Running index
$\sigma_{ext}$	Extinction cross section
$\sigma_{sca}$	Scattering cross section
$\sigma_{abs}$	Absorption cross section
$a_n$	Mie coefficient
$b_n$	Mie coefficient
$\mathbf{k}$	Wave vector

$\psi_n$	Riccardi-Bessel function
$\eta_n$	Riccardi-Bessel function
$\mathbf{n}_{particle}$	Refractive index of the particle
$\mathbf{n}_{Medium}$	Refractive index of the medium
$\mathbf{m}$	Ratio of the particle refractive index and the medium refractive index
$\lambda$	Wavelength of incident electromagnetic light
$\epsilon_1$	Real part of the particles dielectric constant
$\epsilon_2$	Imaginary part of the particles dielectric constant
$\lambda_D$	Debye length
$\mathbf{n}_e$	Electron number density
$\mathbf{T}_e$	Electron temperature
$\mathbf{F}$	Restoring electric force
$\mathbf{k}_{sp}$	Spring constant
$\mathbf{x}$	Distance
$\vec{E}$	Electric field vector
$E$	Magnitude of electric field
$\mathbf{F}_{driving}$	Driving force
$\omega_{pe}$	Electron plasma frequency
$\vec{F}_L$	Lorentz force vector
$\vec{B}$	Magnetic field
$\vec{v}$	Velocity
$\mathbf{v}_{  }$	Velocity component parallel to the magnetic field
$\mathbf{v}_{\perp}$	Velocity component perpendicular to the magnetic field
$\mathbf{q}$	Charge
$\mathbf{m}$	Mass
$\mathbf{B}$	Magnetic field
$\gamma_i$	Surface energy per unit area at substrate-film interface
$\gamma_s$	Surface energy per unit area at substrate-vapor interface
$\gamma_f$	Surface energy per unit area at film-vapor interface
$\theta_{cont}$	Contact angle
$\mathbf{T}_s$	Substrate temperature
$\mathbf{T}_m$	Melting temperature
$\mathbf{I}_0$	Initial intensity of the electromagnetic irradiation
$\mathbf{I}_r$	Reflected intensity of the electromagnetic irradiation
$\mathbf{I}_t$	Transmitted intensity of the electromagnetic irradiation
$\mathbf{I}_a$	Absorbed intensity of the electromagnetic irradiation
$\mathbf{R}$	Reflectance
$\mathbf{T}$	Transmittance
$\mathbf{A}$	Absorption
$\mathbf{A}_b$	Absorbance
$\mathbf{O}_D$	Optical density
$\epsilon$	Molar extinction coefficient
$\mathbf{c}$	Concentration
$\mathbf{d}$	Layer thickness
$\theta_{diff}$	Diffraction angle
$\mathbf{a}_0$	Lattice parameter
$\mathbf{d}_x$	Nominal layer thickness of x
$\mathbf{p}_e$	Impulse

$h_1$	Miller index
$h_2$	Miller index
$h_3$	Miller index
$\omega$	Angular frequency

## Constants

Symbol	Name	Value
<b>eV</b>	Electron-volt	$1.602176565(35) \times 10^{-19} \text{ J}$
<b>e</b>	Elementary charge	$1.6021766208(98) \times 10^{-19} \text{ C}$
$\epsilon_0$	Vacuum permittivity	$8.8541878176 \times 10^{-12} \text{ F/m}$
<b>k</b>	Boltzmann constant	$1.38064852(79) \times 10^{-23} \text{ J/K}$
<b>m<sub>e</sub></b>	Electron mass	$9.10938356(11) \times 10^{-31} \text{ kg}$
$\pi$	Ludolph's constant	3.14159
<b>h</b>	Planck constant	$6.62607004 \times 10^{-34} \text{ m}^2 \text{ kg/s}$



## Introduction

Nanoparticles exhibit a high surface-to-volume ratio and show behavior that varies considerably from that in their bulk state, for instance lower melting points. Some metals that possess a certain electron configuration can feature localized surface plasmon resonance (LSPR) within the visible region of light in their nanoparticulate state. In Au and Ag nanoparticles, conduction electrons can show collective oscillations under irradiation by near ultraviolet and visible light if the incident light matches the corresponding resonance frequencies. The increase in absorption and scattering cross sections of the nanoparticles in addition to the formation of electric fields in their vicinity [1] lead to a sizable photocurrent. The amplitude and excitation frequency are strongly influenced by the dielectric function of the metal and the surrounding medium, the nanoparticles shape, size and size distribution as well as by inter-particle distances [2][1][3][4][5].

Because of their LSPR, combinations of Au or Ag nanoparticles with a semiconducting metal oxide such as  $\text{TiO}_2$  provide very interesting materials for applications in solar water splitting or photovoltaics. Exposure of such samples to irradiation within a defined wavelength range of visible light leads to generation of charge carriers driving chemical reactions or electric current generation. Charge carrier generation is driven not only by a high catalytic activity that is commonly exhibited by metallic nanoparticles but also by plasmon-induced mechanisms such as hot electron injection, near-field enhancement and scattering. The charge generation depends on the metal-metal oxide interface that is crucial for charge transport as well as the spectral overlap between the particles LSPR and the semiconductors band gap absorption. An overall aim of recent research efforts in this area is to identify the preparation protocol that results in the highest photocurrent density; i.e. the largest amount of usable photocharge carries.

Different synthesis pathways are known for nanoparticles preparation e.g. lithography [6][7][8], thermal evaporation [9], sputtering [10][11][12] and chemical reduction [13][14]. Nanostructures are further formed by taking advantage of Ostwald ripening and/or solid state dewetting induced by thermal annealing of magnetron-sputtered thin films. The thermal treatment drives surface diffusion [15], particle coalescence and solid state dewetting, i.e. the segregation of thin films to nanoislands in order to minimize the surface energy density of the system. Physical methods such as magnetron sputtering have the advantage of homogenous, reproducible and controlled deposition of thin films without organic additives as e.g. used in chemical synthesis pathways. The homogenous deposition of large areas with minimal waste products makes this preparation method especially interesting for large-scale applications.

There is already fundamental knowledge on annealing of metal layers on substrates like silicon [16][8][17][15], silica [18][17][19][20][21][22][23], polytetrafluoroethylene [11], sapphire [24][25] or

single-crystal MgO substrates [26] that exhibit smooth surfaces. Applications such as catalytic water splitting, however, need porous supports with large surface areas. The surface topology of TiO<sub>2</sub> deposited by direct-current (DC) magnetron sputtering could possibly lead to inhomogeneous nanoparticle growth and location-dependence of particle properties. This hypothesis needs testing because the correlation between nanoparticle plasmonics and substrate topology could contribute to improve the design of sensors and catalytic systems.

The attractiveness of this preparation method for industrial manufacturing critically depends on whether even small fluctuations in the initial parameter lead to significant deviation in nanoparticle properties; in other words if the chosen method is robust. In the literature, thermal annealing of metal layers were mainly investigated under variation of the applied temperature [16][27][28][21][29][30][31][32], layer thickness [33][18][21][29][30] or substrate crystallographic orientation [26]. Three additional parameters are worth investigating, namely the annealing time, the applied temperature ramp and the composition of the gas atmosphere (oxygen and argon). Their influence on nanoparticles morphology, optical response and charge carrier generation needs attention.

Bimetallic nanoparticles have raised strong interest especially in surface plasmon-enhanced Raman spectroscopy and heterogeneous catalysis. They can appear as alloys, in a raspberry structure or core-shell structure. Au/Ag core-shell structures are commonly prepared chemically. Their preparation by a combination of magnetron sputtering and annealing introduces a truly novel, innovative synthesis method with advantages such as absence of solvent and chemical waste as well as homogenous large-area deposition. The absence of stabilization and capping agents such as cetyltrimethylammonium bromide (CTAB) or polyvinylpyrrolidone (PVP) is critical for sensing applications that focus on the interaction of target molecules with the nanoparticle surface atoms [34].

The first chapter outlines the aims and the structure of this thesis before chapter two introduces basic ideas and relevant concepts such as the phenomenon of localized surface plasmon resonance, possible plasmon-induced energy transfer mechanisms, intrinsic properties of TiO<sub>2</sub>, Au and Ag, characteristics of physical plasmas, thin film growth and nanostructure formation. Chapter three summarizes the current state-of-the-art for Au/TiO<sub>2</sub> and AuAg/TiO<sub>2</sub> systems. Chapter four describes the materials and synthesis methods applied in this work including a detailed description of the magnetron-sputtering processes and annealing regimes. The fifth chapter focuses on analytical tools for material characterization, for instance UV-vis spectrometer, scanning electron microscopy, transmission electron microscopy, profilometry, X-ray diffraction and photoelectrochemical half-cell tests. Chapter six presents the main results and discusses them. First, the morphological and plasmonic properties of Au/TiO<sub>2</sub> are discussed and correlated with the TiO<sub>2</sub> topology. Furthermore, the role of annealing time, temperature ramp and the composition of the gas atmosphere on the particles properties is investigated by studying nanoparticles morphology, plasmon resonance frequency, crystallinity and photocurrent generation. The next section introduces a preparation method to synthesize bimetallic Au-core Ag-shell nanoparticles with varying elemental ratio and compares their morphology and optical absorption. Based on these results, parameters such as metal loading and annealing regimes are further optimized for enhanced photocurrent generation as described in a final section of Chapter six. Results of this work are summarized in a final conclusion given in Chapter seven. The appendix contains additional information detailed data.

The results of this PhD work are published or will be submitted to peer-reviewed journals as follows:

1. Sandra Peglow, Marga-Martina Pohl, Angela Kruth and Volker Brüser "Plasma based synthesis, electron microscopy, and optical characterization of Au-, Ag-, and Ag/Au-core-shell

nanoparticles"

*J. Phys. Chem. C*, 2015, 119 (1), pp 563-572

2. Angela Kruth, Sandra Peglow, Antje Quade, Marga-Martina Pohl, Rüdiger Foest, Volker Brüser and Klaus-Dieter Weltmann "Structural and photoelectrochemical properties of DC magnetron-sputtered TiO<sub>2</sub> layers on FTO"  
*J. Phys. Chem. C* 2014, 118, 25234-25244
3. Angela Kruth, Sandra Peglow, Nils Rockstroh, Henrik Junge, Volker Brüser and Klaus-Dieter Weltmann "Enhancement of photocatalytic activity of dye sensitised anatase layers by application of a plasma-polymerized allylamine encapsulation"  
*J. Photochem. Photobiol. A Chem.*, 2015, 290 , 31-37
4. Sandra Peglow, Alexander Müller, Michael Karnahl, Angela Kruth, Volker Brüser, Henrik Junge and Christina Scheu "Au and Au/Ag nanoparticles on titania layers: correlation of deposition method, morphology and photo(electro)-catalytic properties"  
*to be submitted in 2017*

Results were also presented at following conference talks and poster presentations:

1. 10-th Symposium on Vacuum based Science and Technology, Kolobrzeg, 2017, "Plasma-vapour-deposition synthesis of Au and Au-Ag core-shell nanoparticle on metal oxide semiconductors"  
*oral presentation*
2. 22nd International Symposium on Plasma Chemistry (ISPC), Antwerp, 2015, "Plasma-Vapour-Deposition Synthesis of Au, Ag and AuAg Core-Shell Nanoparticle on Metal Oxide Semiconductors"  
*oral presentation*
3. SolarFuel15, Mallorca, 2015, "Physical Vapour Deposition Synthesis of Au, Ag, and Au/Ag Core-Shell Nanoparticles on Metal Oxide Semiconductors for Photocatalytic Applications"  
*poster presentation*

This work was carried out in close collaboration with colleagues from INP (Greifswald), MPIE (Düsseldorf), LIKAT (Rostock) and Fraunhofer IWS (Dresden). Dr. Angela Kruth and Dr. Harm Wulff (INP) carried out X-ray diffraction and crystallite size calculation. Dr. Marga-Martina Pohl (LIKAT) and Dr. Alexander Müller (MPIE) performed TEM and EDX analysis including preparation of sample cross sections. Daniel Köpp (INP) synthesized TiO<sub>2</sub> substrates by reactive direct current (DC) magnetron sputtering and Thomas Abendroth assisted by preparation of atmospheric pressure chemical vapor deposition (AP-CVD) TiO<sub>2</sub> samples.

## 2.1 Localized surface plasmon resonance

### 2.1.1 History and scientific description of nanoparticles

Metal nanoparticles have already been used in ancient times because of their unique properties. Clear and lustrous colors of glass, ceramics, china and pottery was achieved by incorporation of nanoparticles. A well-known example is the Lycurgus cup manufactured in the 4<sup>th</sup> century AD [35] that is presently exhibited in the British Museum in London (figure 2.1). The glass appears green in reflecting light and red on light transmission through the glass induced by embedded Au-Ag alloy nanoparticles with a size of about 70 nm. A further example of ancient use of metal nanoparticles for coloring is Saint Chapelle in Paris with its stunning church windows.

The scientific background for this phenomenon was, however, not provided until the 19<sup>th</sup> century by Michael Faraday in 1857 [36]. He produced Au colloids and observed a different coloration of the solutions varying from ruby red to amethyst. He achieved a breakthrough in scientific understanding by concluding that the color of the solution was due to different sizes of the Au particles rather than a result of a chemical reaction.

The science of nano-sized particles connects classical solid state physics and quantum mechanics. Quantum mechanic effects have to be considered for structures below 5 nm and inter-particle distances below 1 nm (tunnel effect). Although plasmons are considered as bosonic quasi-particles, the classical description is valid for the huge number of electrons in significantly large nanoparticles. Conventionally, their quantum mechanic properties are hidden in the dielectric constants that are usually gained from experiments.

### 2.1.2 Localized surface plasmons

Two types of plasmons can be distinguished: propagating surface plasmons along a metal-dielectric interface and localized surface plasmons confined to a nanostructure. This PhD thesis only discusses the localized surface plasmon resonance (LSPR) and refers the reader to excellent resources such as Sarid and Challener [38] for insights into propagating plasmons.

Electromagnetic light can directly excite surface plasmons in metal nanostructures [39]. The free electrons follow the electromagnetic field lines, which results in an accumulation of negative charges on one side of the particle surface. The opposite surface becomes positively charged due to the ion lattice that is depleted from the electrons. An electric field is induced across the particle



**Figure 2.1:** Embedment of Au-Ag alloy particles with 50-100 nm diameter give this roman glass vessel, known as the Lycurgus cup, a dichroic property [35]: the glass appears red in transmission (left) and green in reflection (right). Image from Savage et al. [37]

between both charges and generates a restoring Coloumbic force. This restoring force would induce an oscillating motion of the electrons, if the external excitation would vanish, until they reach their former equilibrium. The frequency of this oscillation is the resonance frequency of the system analog to a simple harmonic damped oscillator. The external electromagnetic field of the light itself oscillates and therefore drives an oscillating displacement of the free electrons in the nanoparticle (figure 2.2). If the electromagnetic frequency approaches the resonance frequency of the system, the extinction cross section of the nanoparticle increases and can even exceed its geometrical cross section [40]. For comparison, the scattering flux of a metallic nanoparticles with a size of about 80 nm is found to be of the same magnitude as that of  $10^6$  fluorescein molecules [41]. The resonance frequency is determined by the strength of the restoring force and the effective mass of the electrons [42], but it also depends on the particle size [43][42][40], shape [43][42][40], distance to neighboring particles, the refractive index of the surrounding medium [42][40] and its composition [40].

Plasmon excitation induces electric fields in the nanoparticle that can couple with adjacent atoms, molecules or neighboring nanoparticles. These induced electromagnetic fields are divided into a far-field and a near-field. The far-field is related to macroscopic effects such as the absorption and scattering of light, whereas the near-field allows plasmon-coupling of nearby particles and interaction with the environment, e.g. with adsorbed molecule [44]. The oscillating electron density at excitation of LSPR creates an intense, non-homogeneous electric field in the vicinity of the nanoparticles that is opposite to the incident field of the radiation [43][41][45]. Inside the particle, polarization and related electromagnetic field are constant [45]. At the surface, however, there are electromagnetic fields that are about 100 times stronger than the incident light. Their decay is described by  $\left(\frac{r}{R_p}\right)^{-6}$  with  $R_p$  as the particle radius and  $r$  defined as the distance from the particle center such that  $r = R_p$  describes the particles surface [45]. Within a distance of 20-30 nm from the particle surface, the field intensity decreases exponentially, continuing linearly further away [43]. That leads to a high concentration of light energy in a very focused volume around the

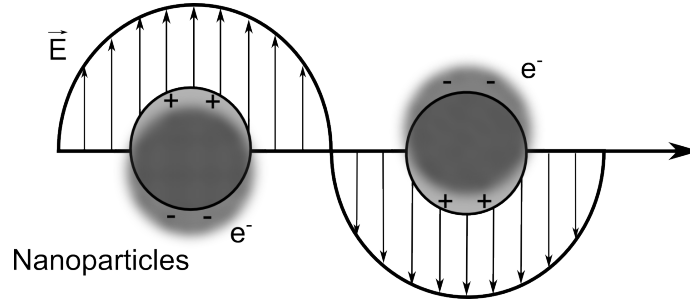


**Figure 2.2:** Resonant excitation of electron oscillation in a confined nanostructure is called localized surface plasmon resonance [46][47].

nanostructure [43]. Particles exhibiting non-spherical geometries with sharp edges and tips are of specific interest because high surface curvatures significantly enhance electric field generation.

### 2.1.3 Quasi-static approximation

The interaction between nanoparticle and electromagnetic field can be described for the simple case when the particle exhibits a diameter that is much smaller than the wavelength of the incident illumination. In this simplification, the particle senses an electromagnetic field that has the same phase over the entire volume of the particle. This reduces the problem to an electrostatic field, neglecting phase retardation and higher multipole excitation and adding a harmonic time dependence afterwards (quasi-static). If the wavelengths of the incident light is within the UV-Vis region, the approximation is valid for plasmonic nanoparticle dimensions of up to 100 nm. Another requirement for the quasi-static approximation is that the nanoparticle is an isotropic, homogenous sphere with a dielectric function  $\epsilon(\omega)$  surrounded by a non-absorbing isotropic medium with a dielectric constant  $\epsilon_m$ . The incident electric field should be static, uniform and in z-direction. The argumentation for the quasi-static approximation is taken from [39]. Here only the relevant intermediate steps will be recapitulated.

The aim of the quasi-static approximation is to calculate the nanoparticle polarization and to formulate the resonance condition. This approach starts by determining the potential and calculating the solutions for the Laplace equations. A general solution for the potential includes the Legendre polynomials  $P_l(\cos \theta)$ :

$$\Phi(r, \theta) = \sum_{l=0}^{\infty} \left[ A_l r^l + B_l r^{-(l+1)} \right] P_l(\cos \theta) \quad (2.1)$$

Here,  $l$  is the polynomial order and  $\theta$  the angle between the vector  $r$  from the particle center to point  $O$  and the  $z$ -axis. In the following, the potential is distinguished for the outer (out) potential and the one inside (in) the particle.

$$\Phi_{in}(r, \theta) = \sum_{l=0}^{\infty} A_l r^l P_l(\cos \theta) \quad (2.2)$$

$$\Phi_{out}(r, \theta) = \sum_{l=0}^{\infty} \left[ B_l r^l + C_l r^{-(l+1)} \right] P_l(\cos \theta). \quad (2.3)$$

Several boundary conditions allow to determine the coefficients  $A_l$ ,  $B_l$  and  $C_l$ . Furthermore, since the normal components of the displacement fields are equal, the dielectric constants of the medium  $\epsilon_m$ , the vacuum permittivity  $\epsilon_0$  and the dielectric function of the particle  $\epsilon(\omega)$  are introduced. For a more detailed analysis, the reader is referred to electromagnetic textbooks like "Classical Electrodynamics" by Jackson [48]. The final result of the calculation is:

$$\Phi_{in} = -\frac{3\epsilon_m}{\epsilon + 2\epsilon_m} E_0 r \cos\theta \quad (2.4)$$

$$\Phi_{out} = -E_0 r \cos\theta + \frac{\epsilon - \epsilon_m}{\epsilon + 2\epsilon_m} E_0 R_p^3 \frac{\cos\theta}{r^2} \quad (2.5)$$

The potential for the outer field is a superposition of the external incident field  $E_0$  and an induced dipole from the nanoparticle. The particles dipolar nature can be expressed by a dipole moment  $\mathbf{p}$ . Hence, it can be written as

$$\Phi_{out} = -E_0 r \cos\theta + \frac{\mathbf{p} \cdot \mathbf{r}}{4\pi\epsilon_0\epsilon_m r^3} \quad (2.6)$$

with the dipole moment  $\mathbf{p}$  defined as

$$\mathbf{p} = 4\pi\epsilon_0\epsilon_m R_p^3 \frac{\epsilon - \epsilon_m}{\epsilon + 2\epsilon_m} \mathbf{E}_0. \quad (2.7)$$

The induced dipole moment is proportional to the applied electric field.

$$\mathbf{p} = \epsilon_0\epsilon_m \alpha \mathbf{E}_0. \quad (2.8)$$

This finally introduces the polarizability:

$$\alpha = 4\pi R_p^3 \frac{\epsilon - \epsilon_m}{\epsilon + 2\epsilon_m}. \quad (2.9)$$

The polarizability shows a resonant enhancement when its denominator gets minimal, so the resonance condition is

$$\text{Re}[\epsilon(\omega)] = -2\epsilon_m \quad (2.10)$$

with  $\text{Re}$  indicating the real part of  $\epsilon(\omega)$ . This relationship is called the Fröhlich condition and it is valid for a small or slowly changing imaginary part of the dielectric function  $\text{Im}(\epsilon(\omega))$ .

The polarization never shows a singularity, i.e. it cannot get infinitely large [39], because the denominator in the polarizability, the imaginary part of the dielectric function, does not reach zero. The imaginary part defines the plasmons optical bandwidth, whereas the real part of the metals dielectric function determines the LSPR position [49].

### 2.1.4 Mie theory

The Mie theory provides a theoretical explanation for the occurrence of different colorations of metal colloids and represents an analytical solution of the Maxwell equations. In 1908, Mie presented this theory that was valid for all particle sizes and wavelengths, unlike the theory of Rayleigh [50]. He calculated elastic scattering by an homogenous, isotropic, uncharged spherical particle that could be absorbing or non-absorbing and is embedded in a non-absorbing medium. After finding the appropriate boundary conditions for the Maxwell equations, Mie derived a series expansion of spherical harmonics ( $n=1$  is for dipole). The cross sections of extinction, scattering and absorption can be found as

$$\sigma_{ext} = \frac{2\pi}{|k|^2} \sum_{n=1}^{\infty} (2n+1) \text{Re}[a_n + b_n] \quad (2.11)$$

$$\sigma_{sca} = \frac{2\pi}{k^2} \sum_{n=1}^{\infty} (2n+1) \left[ |a_n|^2 + |b_n|^2 \right] \quad (2.12)$$

$$\sigma_{abs} = \sigma_{ext} - \sigma_{sca} \quad (2.13)$$

with  $k$  being the wave vector. This interpretation origins from Debye. The Mie coefficients  $a_n$  and  $b_n$  are introduced by the multipole extension ( $n=1$  is for dipole) and are defined as

$$a_n = \frac{m\psi_n(mx)\psi'_n(x) - \psi_n(x)\psi'_n(mx)}{m\psi_n(mx)\eta'_n(x) - \eta_n(x)\psi'_n(mx)} \quad (2.14)$$

$$b_n = \frac{\psi_n(mx)\psi'_n(x) - m\psi_n(x)\psi'_n(mx)}{\psi_n(mx)\eta'_n(x) - m\eta_n(x)\psi'_n(mx)} \quad (2.15)$$

$\psi_n$  and  $\eta_n$  are the Riccardi-Bessel functions that use the refractive index of the nanoparticle  $n_{Particle}$  and the medium  $n_{Medium}$

$$m = \frac{n_{Particle}}{n_{Medium}} \quad (2.16)$$

and

$$x = \frac{2\pi R_p}{\lambda} \quad (2.17)$$

and  $R_p$  being the particle radius and  $\lambda$  the wavelength of the incident electromagnetic light. The extinction cross section can alternatively be described by distinguishing the real part of the particles dielectric constant  $\epsilon_1$  and the corresponding imaginary part  $\epsilon_2$

$$\sigma_{ext} = \frac{24\pi^2 R_p^3 \epsilon_m^{2/3} \epsilon_2}{\lambda(\epsilon_1 + 2\epsilon_m)^2 + \epsilon_2^2} \quad (2.18)$$

which results in the well-known resonance condition.

$$\epsilon_1 = -2\epsilon_m \quad (2.19)$$

Mie theory delivers an analytical solution for spherical particles and infinitively long cylinders. Later, extensions were introduced, e.g. by Gans, to describe elliptical particle shapes.

### 2.1.5 Nanoparticle size

Three different particle size regimes dominate the optical properties of metal nanoparticles due to quantum size effects, intrinsic size effects by scattering of the oscillating electrons at the particles surface and extrinsic size effects when the particle diameter and the exciting wavelengths are of the same order of magnitude or larger and lead to retardation.

Quantum size effects have to be considered for particle diameters below 2 nm where the distance between energy states near the Fermi level exceeds  $kT$  and the particle loses its metal properties and can be better described as a semiconductor [40]. If the particle size is smaller than the electron mean free path length during an oscillation period, the electron scatters at the particle surface and introduces a size dependent damping that broadens the LSPR extinction peaks. This intrinsic size effect is relevant for particle dimensions between 4 nm and 45 nm. These two effects are solely determined by the particle properties and do not affect the resonance position [51].

In contrast, retardation effects occur if the particle size is in the order of the excitation wavelength or even larger. Here, the quasi-static approximation is no more valid since the particles



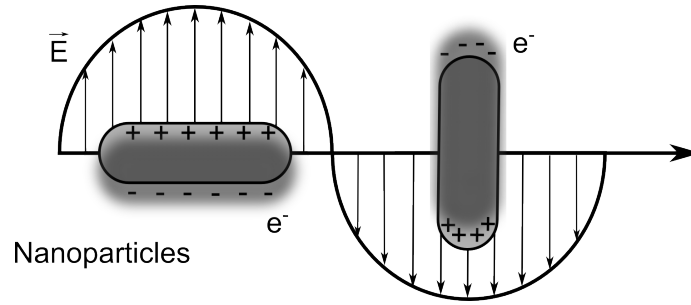


**Figure 2.3:** Electrons in a nanorod can oscillate along the major axis (longitudinal mode) and minor axis (transverse mode) upon excitation of LSPR.

experience a spatially inhomogeneous electric field that gives rise to multipole excitation [41] (quadrupole, etc.), which manifests as additional peaks that are red-shifted compared to the dipole excitation [45][47] [40]. This extrinsic size effect starts to get relevant for particle dimensions of 30 nm and dominates for 50 nm.

The contribution to the optical extinction is size-dependent as it is a sum of absorption and scattering as was discussed and derived in the previous section. Mie theory found a dominance of the absorption cross section to the overall extinction for small nanoparticles while scattering is the major contribution to the extinction for large sizes [45]. The extinction cross section depends linearly on the particle volume. Hence, if a distribution in particle size is present the optical properties of a nanoparticle ensemble are dominated by large particles.

### 2.1.6 Nanoparticle shape

It might seem contra intuitive but a deviation in particle shape has a much stronger effect on the LSPR position than a variation in particle size [40]. In experiments, most nanoparticles deviate from perfectly spherical geometries which could be an advantage for some application.

The Mie-Gans solution can be applied to elliptical and specifically to oblate and prolate spheroids. Elongated particles can be described as cylinders with a longitudinal axis along the longer side and a transverse axis at the shorter dimension. In a prolate spheroidal the two minor axis are equal (cigar) whereas an oblate shape has two equally long major axis (pancake). Electrons are able to oscillate both along the large and the short axis resulting in two separate resonance peaks [39] (figure 2.3). For excitation along the major axis, the oppositely charged surfaces are separated at a larger distance. The restoring force is reduced meaning a lower energy is necessary to excite the resonance. Two distinct absorption peaks are present in the absorption spectrum, the longitudinal one along the major axis being red shifted [41] compared with the plasmonic resonance of a spherical particle with the same volume, and sensitive to the aspect ratio of the particle [40]. The LSPR for the transverse mode in the minor axis is found at a similar position than for a spherical particle [47]. The energetic separation between both absorption bands varies with the aspect ratio of the particles and gets zero in case of spherical particles. The resonance intensity for Au nano-rods is maximal for aspect ratios between 0.3 and 0.4 [52]. The presence of particles with a distribution in aspect ratios leads to a broadening in the longitudinal plasmon peak [40].

### 2.1.7 Bimetallic nanoparticle-influence of material composition

Bimetallic nanoparticles can be alloys or form core-shell nanoparticles. The position of the LSPR depends on the composition and the shell thickness of the system. Monometallic Ag has a plasmon resonance frequency at 400 nm and Au at 520 nm [49]. For alloys, there is only one LSPR peak, that shifts position with a change in molar fraction [53], whereas core-shell nanoparticles exhibit two plasmon peaks [54].

If the Ag layer on a Au core is increases, the Ag related peak will red-shift and is the only observable peak for a very thick shell. Meanwhile the Au related peak shows a non-linear blue-shift [53].

### 2.1.8 Dielectric constant of surrounding medium

The dielectric constant of the surrounding medium influences the resonance frequency [45]. The resonance frequency is reached, when the polarizability has a maximum. Therefore, the denominator has to become zero which leads to the resonance condition that  $\epsilon_1 = -2\epsilon_m$ . With increasing angular frequency  $\omega$  of the incident light, the dielectric function of the metal nanoparticles decreases [45]. With increasing dielectric constant of the medium a decrease in resonance frequency is related [45][44]. If the dielectric constant is increased (from a particle in a vacuum to a substrate such as  $\text{TiO}_2$ ) the resonance condition requests  $\epsilon_1$  to decrease which it does at longer wavelengths. To sum it up, an increase in  $\epsilon_m$  results in a shift of the resonance frequency to longer wavelength. The sensibility of the absorption peak position from the surrounding medium is important for sensing applications.

### 2.1.9 Plasmon coupling

One of the assumptions made by Mie theory is the complete isolation of the nanoparticles. In laboratory and industrial practice, vastly high numbers of nanoparticles are usually present in a solution, immersed in a three-dimensional host matrix, deposited on a two-dimensional surface or aligned in a row, either randomly orientated or in a well determined pattern. Therefore, interactions of neighboring particles due to their plasmon-induced electromagnetic fields have to be considered [41].

High intensities in the order of 1000 times the intensity of the incoming photon flux can be reached at the surface of an isolated particle, and even an enhancement of  $10^6$  between two particles spaced with 1 nm is possible [43]. Such locations with high electric field intensities between plasmonic nanostructures are called „hot spots“ [43][45].

Regarding a pair of neighboring particles with Fröhlich resonances, different kind of dipole-dipole interactions are possible, depending on the relative orientation of the incident light and the dimer axis. Some researcher describe plasmon modes as a hybridization process in analogy to molecular orbits. A collective electron oscillation perpendicular to the particle axis is called a transverse mode and an oscillation along the axis results in a longitudinal mode (figure 2.4). The coupling of nearby particles along their axis in the longitudinal mode can lead to the aforementioned Hot spots between them - areas of strongly enhanced electromagnetic fields. In the hybridization model, this is considered as the binding mode. In contrast, no large field enhancements are generated between the particle gap if transverse modes are excited, that could be seen as degenerated modes[44][45].

To find the optimum distance of two particles to obtain the highest enhancement in field intensity is found by considering two competitive processes. At small separation distances, the Förster resonance energy transfer from non-radiative energy dissipation near the metal surface

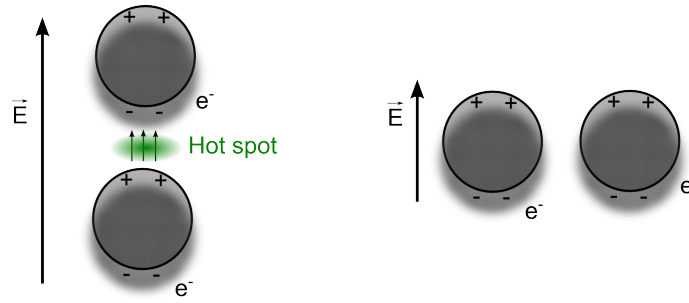


**Figure 2.4:** *Neighboring plasmonic nanoparticles can couple in a longitudinal (left) and transverse (right) mode [45]. Excitation of the longitudinal mode can lead to "hot spots", i.e. regions with enhanced electric near-field, between the particles.*

leads to a loss in energetic charge carriers. At large separation, the electric field can be neglected, leading to an optimum in field intensity between metals separated for some nanometers. In experiments by Linic et al, the maximum in field intensity for Ag nanoparticles in  $\text{TiO}_2$  was found at 2-6 nm distance [43].

The excitation of a longitudinal mode leads to a shift of the absorption peak (of an isolated particle) to longer wavelength whereas the transverse oscillation leads to a blue-shift. The observed shift in peak position gets larger for stronger plasmon-coupling by increasing the particle distance. Such a plasmon coupling only affects the optical properties of the material if the excited oscillations are in phase [45].

### Applications for LSPR

The synthesis of nanoparticles with selective and well-defined properties promoted the use of these materials in various applications such as surface-enhanced Raman spectroscopy [55], single molecule detection [56], biosensors [46], fluorescence enhancement [57], medical photothermal therapy [49], solar cells [58], photoacoustic imaging [59], visible-light sensitive photocatalysis [60]. The sensibility of the LSPR to the dielectric environment of the nanoparticles for instance makes them attractive as sensor materials that can even detect single molecules, while their high scattering and the absence of bleaching are used for labeling applications [41]. The temperature increase due to phonon-phonon decay of the plasmon excitation is applied in photothermal therapy to damage cancer cell by laser excitation [40].

## 2.2 Plasmon-induced energy transfer

Plasmonic nanoparticles can transfer energy to a semiconductor, with a shared interface, via three mechanisms. These are the direct injection of "hot electron" into the conduction band of the semiconductor [43], the generation of electron-hole pairs in the semiconductor due to an enhanced near-field from the nanoparticle, and scattering of the incident light by the nanoparticle for enhanced semiconductor absorption [61][43]. The following paragraphs will focus mainly on Au/ $\text{TiO}_2$  and mentions Ag/ $\text{TiO}_2$  systems where appropriate.

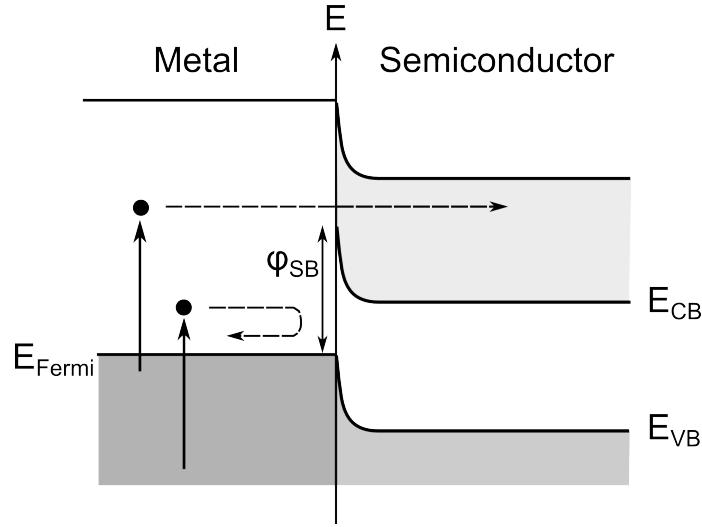


**Figure 2.5:** Hot electron can possess enough energy to overcome the Schottky barrier between the metal nanoparticle and the semiconductor and inject to the semiconductors conduction band. Image created after Clavero [62]

### 2.2.1 Hot electron injection

Au nanoparticles (as well as Ag nanoparticles) and  $\text{TiO}_2$  form a Schottky barrier at their interface. After getting in contact, electrons diffuse from the  $\text{TiO}_2$  to the metal nanoparticle to equalize their Fermi levels. This creates a small region in the titania that is depleted from electrons and therefore positively charged. This space-charge region generates an electric field to prevent further charge transfer [3] and built a so-called Schottky barrier. This barrier prevents the recombination of charges that are created or transferred near the nanoparticle/ $\text{TiO}_2$  interface.

Electrons generated by plasmon-induced intraband transitions in the Au nanoparticle need to overcome the Schottky barrier to be injected to the semiconductor (figure 2.5). Au and Ag can create hot electrons with energies between 1-4 eV [43]. If their energy is higher than the Schottky barrier (with an energy barrier height of approximately 1.0 eV between Au and  $\text{TiO}_2$  [63]) they can migrate to the conduction band of the semiconductor. The  $\text{TiO}_2$  conduction band has a high density of state, which makes this semiconductor highly electron acceptable and provides very fast electron injection [63]. Interestingly, Mubeen et al. [64] proposed a "quantum tunneling effect" that allows the transfer of electrons with energies lower than the Schottky barrier. Since the energy of the LSPR which initiate charge injection into the semiconductor is lower than the semiconductor band gap, the sensitivity of the metal-semiconductor system for light absorption is increased. This process is similar to dye sensitization where the nanoparticles play the role of the light absorbing and charge transferring dyes. Hydrogen evolution e.g. requires energetic electrons, making this energy transfer mechanism especially important for this application [43].

Several requirements have to be fulfilled to enable hot electron injection. This charge injection is only possible when both plasmonic metal and semiconductor are in direct contact [43]. For electron injection, the direction of the electrons momentum has to be normal to the metal/semiconductor interface. Embedment in the semiconductor matrix should therefore increase the amount of injected electrons. Moreover, ultrafast hot electron transfer is needed to prevent energy loss of the hot electrons due to scattering. Ag is easily oxidized and does therefore not support electron

injection. Furthermore, the bands have to be properly aligned in order to provide low Schottky barriers relative to the hot electrons energy. The hot holes present in the nanoparticle after electron injection need to be compensated (charge balance). To prevent the hot electrons from injecting back into the metal, an upwards bended conduction band is used in the semiconductor that drives the electrons towards the bulk. Hence, an n-type semiconductor is preferred.

Damping is the loss of coherence of the oscillating electrons either by energy decay or by scattering. However, scattering on impurities, lattice defects, phonons, electrons and the particle surface does not result in a change in energy but in momentum since only the direction is changed. The Damping process can be divided into radiative and non-radiative damping. Radiative damping contains the emission of photons such as in scattering events. The radiative decay depends on the size of the particles. Non-radiative damping is due to electron-hole pairs (intraband and interband excitation) via Landau damping. Furthermore the oscillation can decay into heat.

Plasmons decay on different time scales. Within 100 fs, the electron, sharing a non-Fermi distribution, relax through electron-electron interactions. After 1-10 ps electron-phonon interact and finally phonon-phonon interactions take place in a time frame of approximately 100ps. Furube et al observed electron transfer from Au NP to TiO<sub>2</sub> conduction band (CB) within 240 fs (with was the time resolution possible in their experiments). They concluded the transfer happening before or during the electron-electron thermalization mechanism. They estimated the injection efficiency to be 40% [63]. However, even up to 1 ns back transfer from electrons to the Au NP were observed. It was suggested, that this back transfer is suppressed by an appropriate electrolyte [63].

### 2.2.2 Near-field enhancement

Plasmon-induced electric fields at nanoparticle surfaces can transfer energy to an adjacent semiconductor. This mechanism was demonstrated for a system that separated the metal nanoparticles and the semiconductor by a thin isolated film to prevent direct electron injection. In this case, the energy was transferred through near-field radiation [43].

The plasmon-induced oscillation creates an electric field (as described in section 2.1.2) that interacts with the semiconductor near the metal nanoparticles. This transferred energy is determined by the amount of overlap between the LSPR and the optical transition in the semiconductor, the near-field intensity and the semiconductor volume that is penetrated by this field. If the LSPR overlaps with the interband transition energy of the semiconductor, the field will excite electron-hole pairs in the semiconductor [43]. Applications such as photocatalysis traditionally use semiconductors with large band gaps and often rely on the existence of defect states that are positioned within the band gap for this mechanism [65].

The generated near-field of the nanoparticles can be 10 to 1000 times larger than the incident electric field [61]. The photocharge generation rate is proportional to  $|E|^2$  with E being the local intensity of the electric field, which makes „hot spots“, areas of concentrated electric fields [43], particularly interesting.

### 2.2.3 Nanoparticle scattering

Plasmons can decay radiatively and emit a photon that is scattered from the nanoparticles surface. Similarly to near-field enhancement, the absorption of the metal nanoparticles and the semiconductor need to overlap for this mechanism [43]. The scattered photons can be absorbed by the semiconductor to excite an electron from the valence to the conduction band [66]. Scattering is dominant in large particles of approximately 50 nm [43]. However, the contribution of this mechanism to the total energy transfer efficiency is proposed to be negligible [61].

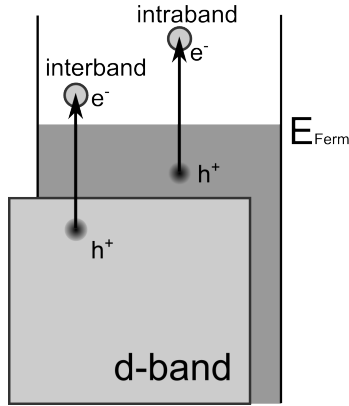


**Figure 2.6:** Excited electrons can undergo inter- and intraband transitions. Image created after Trügler [52]

## 2.3 Metal and semiconductor materials

Au/TiO<sub>2</sub> and AuAg/TiO<sub>2</sub> systems are the focus of this thesis. The combination of both materials lead to exceptional performance enhancement in photocatalysis, sensing and photovoltaic because of energy and charge transfer mechanisms. This paragraph describes the properties of TiO<sub>2</sub>, Au and Ag materials. It introduces the band gap of TiO<sub>2</sub> that determines its absorption, describes the Drude Sommerfeld model of quasi-free electrons in a metal and shortly presents the properties of Au and Ag.

### 2.3.1 TiO<sub>2</sub>

Titanium dioxide (also titanium (IV) oxide or titania) is a metal oxide semiconductor with a face-centered cubic (fcc) crystal lattice. It contains oxygen and titanium atoms that form TiO<sub>6</sub> octahedra with shared edges in a tetragonal cell for the metastable anatase modification. TiO<sub>2</sub> can further appear in the likewise metastable brookite modification and as the stable polymorph rutile, however, photocatalytic activity is solely reported for anatase and rutile [67][68].

The valence electrons of this semiconductor are shifted towards the highly electronegative oxygen that forms a strong polar or even ionic bond with the titanium [69]. Hence, the valence band is mainly formed by O 2p orbitals [69][70][71], whereas the conduction band is composed of Ti d orbitals [70].

TiO<sub>2</sub> is classified as an n-type semiconductor because of the excess electrons from oxygen defects [72][3] and possesses a band gap of 3.2 eV, corresponds to an absorption of wavelengths below 386 nm [67], for the anatase phase [73][67][68].

### 2.3.2 Drude-Sommerfeld Theory

The motion of electrons were theoretically describes by Drude, who developed a theory that was extended by Lorentz, Sommerfeld and Bethe. The original Drude model assumed an electron gas as an aggregation of free, independent particles that do not interact with nuclei or other electrons. However, collisions with the ion lattice had to be considered in an extended Drude-Sommerfeld theory by introducing a damping in form of a mean free time (30 fs for Au) [74]. As a result, the

electrons are merely quasi-free. Between collisions, the negatively charged electrons could be accelerated by electric and magnetic fields [75].

Although the Drude-Sommerfeld model described the dielectric properties of materials in the infrared region according to experiments, it lacked to describe UV-vis behavior because electron intraband transition (inside the sp-band) and interband transition (from deep d-band to sp-band) need to be considered in this wavelength region (figure 2.6) [76].

### 2.3.3 Au and Ag nanoparticles

Au and Ag are transition and noble metals from the 11th group of the periodic table with an electronic configuration of [Xe] 4f<sup>14</sup> 5d<sup>10</sup> 6s<sup>1</sup> and [Kr] 4d<sup>10</sup> 5s<sup>1</sup>, respectively [77]. This notation shows that both metals possess a completely filled d-subshell (Ag: 4d; Au: 5d) and a half-filled s-subshells (Ag: 5s, Au: 6s). The s-electrons are part of a sp-hybridized band that is filled up to the Fermi energy and are regarded as quasi-free according to the Drude-Sommerfeld model.

Au is inert to chemical reactions, a good electric and thermal conductor, catalytically active at low temperature and exhibits the lowest electrochemical potential and highest electronegativity of all metals [78]. Ag is less chemically stable than Au [79].

## 2.4 Plasma

Physical plasma, referred to as the fourth state of matter [80], is a central aspect of this thesis. Electron oscillation observed in a plasma resulted in the definition of the term "plasma frequency" [80][81]. This physical value is important to describe the collective oscillation of the quasi-free conduction electrons in localized surface plasmon resonance. Moreover, the ions generated by a low-temperature plasma in magnetron sputtering were used in this thesis to knock-out atoms from a Au or Ag target and to deposit these metals. This paragraph introduces general plasma properties such as quasi-neutrality and collective behaviour and it defines the plasma frequency. It discusses the motion of charged particles in electric and magnetic fields in order to understand the advantages of a magnetron in thin film sputtering deposition.

### 2.4.1 General plasma properties

Plasma is defined as a quasi-neutral gas that consists of both charged and neutral species exhibiting collective behavior. In contrast to neutral gases where interactions between particles are only controlled by collisions (under the assumption that the gravitational force can be omitted), local concentrations of electric charges in the plasma can generate long-ranging Coulombic field. These fields influence the motions of several particles even in great distance and give the plasma its collective characteristics [82][80].

The quasi-neutrality aspect of a plasma is illuminated by introducing the concept of the Debye length. A local positive or negative electric charge that is emerged in a plasma will generate an electric field that attracts oppositely charged particles to reduce it. This displacement leads to the formation of polarization charges that shield the plasma from the initial charge. This mechanism is referred to as Debye-Shielding and ensures the global quasi-neutrality of the plasma. The electric potential is present over the distance  $\lambda_D$  from the initial charge that is called the Debye lengths. It is determined by the electron density  $n_e$  and their temperature  $T_e$ :

$$\lambda_D = \sqrt{\frac{\epsilon_0 k T_e}{n_e e^2}}. \quad (2.20)$$

In this equation,  $\epsilon_0$  is the vacuum permittivity,  $k$  the Boltzmann constant and  $e$  the electron charge. A sphere with the radius of the Debye length is termed "Debye sphere" and contains approximately  $10^4$  to  $10^7$  electrons in low-temperature plasma. Outside the Debye sphere, the charges of negative and positive species will balance and the system will appear as quasi-neutral. It can be clearly seen that a system has to have larger dimensions than the Debye length in order to exhibit plasma-like behavior [82]. Most atoms are singly ionized and the number density of ions and electrons are therefore considered equal.

To obtain the plasma state, some atoms of a material, usually a gas, have to receive energy higher than their ionization energy that results in the formation of positive heavy ions and light negative electrons. The random kinetic energy of the system has to be higher than the average electrostatic energy to ensure the existence of an unbound gas. This can be achieved by ignition of an electric discharge (e.g. direct current, radio frequency or micro-wave), exposition to energetic photons or application of thermal energy. Generally, the plasma has to be both excited and sustained by an external energy source to balance the recombination of the charged species to neutral atoms. The application of an electric field accelerates both the positive ions and the negative electrons. Since the electrons mass is considerably lower than the ion mass, they absorb the external energy more efficiently and drive the ionization and dissociation of the neutral particles by inelastic collisions [80].

The species found in a plasma are generally divided into light species (the electrons) and heavy species such as neutral atoms, molecules, molecule fragments and positive ions. Their temperature is described by their average kinetic energy [80]. In a non-magnetized non-thermal plasma, both particle entities are commonly in quasi-equilibrium among themselves [80]. The temperature of the electrons could be high (in the order of  $10^4$ K or several eV [82]) although the heavy neutral atoms and positive ions can have room temperature because the energy transfer with electron densities of typically  $10^{10} \text{ cm}^{-3}$  is not sufficient. Those plasmas are termed "low-temperature plasmas".

### 2.4.2 Plasma frequency

Although global charge neutrality is assumed in a plasma, the charges could be disturbed by electric fields. The electrons mass is significantly lower than the mass of the ions, hence, the electrons will respond faster an external field and are displaced by a distance  $\Delta x$  from the positive background of the ions. A restoring force  $F$  establishes to retain the equilibrium position, analog to a spring, and can be described by Hooke's law

$$F = -k_{sp}\Delta x \quad (2.21)$$

with  $k_{sp}$  being the spring constant. In a plasma, the restoring force will be an electric field  $E$  that is determined by applying Gauss law such that

$$E = \frac{n_e e \Delta x}{\epsilon_0}. \quad (2.22)$$

Similar to a spring that is displaced and released, the electrons will start to oscillate until reaching equilibrium, which is described as a harmonic oscillator [80]. The driving force is the external electric field  $E$

$$F_{driving} = (-e)E. \quad (2.23)$$

It is equal to Newtons second law:

$$m_e \frac{d^2 \Delta x}{dt^2} = (-e)E = -\frac{n_e e^2}{\epsilon_0} \Delta x. \quad (2.24)$$



with  $m_e$  being the electron mass. Rearranging the equation results in the description of a harmonic oscillator

$$\frac{d^2 \Delta x}{dt^2} + \left( \frac{n_e e^2}{\epsilon_0 m_e} \right) \Delta x = 0 \quad (2.25)$$

with the square of the oscillation frequency (the electron plasma frequency  $\omega_{pe}$ ) given as the term in parentheses

$$\omega_{pe} = \sqrt{\frac{n_e e^2}{\epsilon_0 m_e}}. \quad (2.26)$$

It is characterized by the electron number density  $n_e$  of the system. The Debye shielding described in the previous paragraph is an example of a rather static collective behavior of plasma, whereas plasma oscillation shows the dynamic aspect of plasma collectivity. The product of the plasma frequency and the Debye lengths is approximately equal to the average thermal velocity of the electrons [80]. For excitation frequencies below the plasma frequency, the electrons are able to follow the forced perturbation and the wave is reflected. In the case of frequencies higher than the plasma frequency, the electrons cannot follow the perturbation and thus cannot shield the charges. That is why low-energy radio waves are reflected by the ionosphere (a natural low-temperature plasma) and can be detected by radio stations behind the horizon. High energy electromagnetic waves however are necessary to communicate from a ground station to an orbiting satellite [83].

### 2.4.3 Motion of charged particle in magnetic and electric field

Consider a particle with charge  $q$  and mass  $m$  moving with a non-relativistic velocity  $\vec{v}$  in a spatially and temporally constant magnetic field  $\vec{B}$  pointing in the  $z$  direction. The magnetic field imposes a Lorentz force  $\vec{F}_L$

$$\vec{F}_L = q(\vec{v} \times \vec{B}). \quad (2.27)$$

on the charge. The Lorentz force is zero, if the particles trajectory is parallel to the magnetic field lines ( $v_{||}$ ) and thus the particles motion is undisturbed. However, if the particle enters the field perpendicular to the field lines ( $v_{\perp}$ ), the cross product leads to a constant Lorentz force always perpendicular to both velocity vector and magnetic field vector. The particles trajectory describes a circle with the Larmor-radius  $r_L$  defined as

$$r_L = \frac{mv_{\perp}}{|q|B}. \quad (2.28)$$

The direction of the rotation is determined by the sign of the charge, with positive charges rotating in left hand sense and negative charges in right hand sense [80]. In case a charge enters the magnetic field under an arbitrary angle relative to the field lines, its velocity vector is separated into a parallel ( $v_{||}$ ) and a perpendicular ( $v_{\perp}$ ) part. The parallel velocity  $v_{||}$  is not effected by the Lorentz force whereas  $v_{\perp}$  forces a circular motion. If both parts are non-zero, the particle is carrying out a helical trajectory around a guiding center.

In many application the charged particle is not only exposed to a magnetic but also to an electric field. As was mentioned above, a charged particle with no  $v_{||}$  circulates around a magnetic field line in a constant distance described by the cyclotron radius. If an electric field perpendicular to the magnetic field line is added it exerts a force on the charge. An electron that moves in the direction of  $\vec{E}$  during its rotation will be decelerated by the electric field and its velocity and Larmor radius will decrease according to equation 2.28. However, it will be accelerated if it moves opposite to  $\vec{E}$  and the increase in velocity will cause a larger radius  $r_L$ . The electron will execute a drift in the direction perpendicular to both  $\vec{E}$  and  $\vec{B}$  called the  $\vec{E} \times \vec{B}$ -drift. The direction of the drift is independent from the particle charge  $q$  [84].

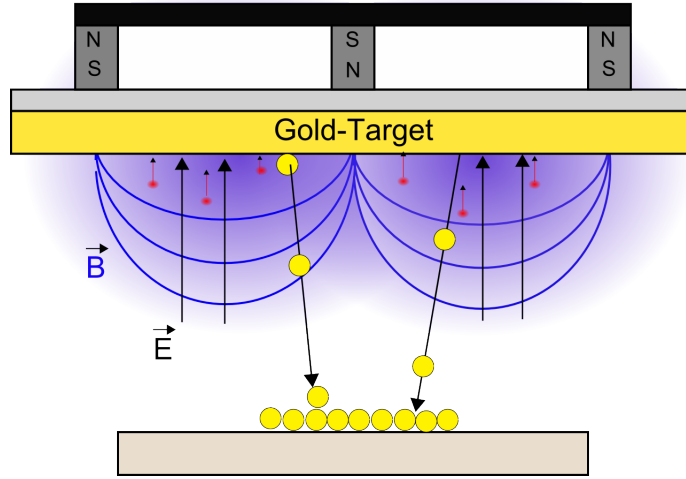


**Figure 2.7:** Magnetrons create an magnetic field to trap electrons near the target and increase the sputter yield.

#### 2.4.4 Magnetron sputtering

Magnetron sputtering is a plasma-based method for thin film deposition for films that are decorative [85], corrosion-resistant [86], hard [87] and wear-resistant [88], have low friction [89] or tailored electrical properties [90]. This section starts by describing the direct current (DC) sputtering process before it continues with sputtering processes that use alternating, radio frequency (RF) potentials. Finally, the mechanisms and advantages of a magnetron is presented.

Direct current (DC) sputtering is done by igniting a glow discharge between a cathode (target) and the anode which is either the substrate or the chamber wall. The cathode is made of the target material or such a target is placed on top of the cathode. The applied potential results in plasma formation near the cathode surface [91]. The positive ions are drawn towards the negatively charged cathode and remove neutral atoms from the surface of the target due to their impact [92] [93]. The neutral atoms are not influenced by electromagnetic fields and move in straight lines towards the substrate that is placed opposite of the target. There they are deposited and could form clusters, grow to large islands or complete films, depending on the process parameter and experimental set-up. Additionally, secondary electrons might be emitted from the target surface during ion impact. These ensure that the plasma state is sustained during the process. The whole process is performed at low working gas pressures to generate ions with high energies and ensure sufficiently large mean free path lengths for the sputtered atoms [92].

Radio frequency (RF) sputtering at 13.56 MHz reverses the polarity of the applied potential periodically. The potential drop described near the cathode in DC sputtering is now formed alternatively on the cathode and anode, respectively. A potential that exhibits a large peak-to-peak voltage can be capacitively coupled to the electrode results in a periodically changing positive and negative potential at the surface. One polarity accelerates the ions to the target material and causes sputtering. The reverse polarity attracts the electron towards the target that prevents charging of the target surface [91]. An impedance matching network regulates the power absorbed by the plasma [92].

A special sputter source uses magnetrons that are placed behind the target and orientated such that one magnetic pole is located at the center of the target and a second pole forms a ring around it (figure 2.7). The magnetic field is mostly parallel to the target surface and electrons could

be trapped by following an  $\vec{E} \times \vec{B}$ -drift in a closed loop above the target surface [94]. Hence, the electron density increases the probability for ion generation in the vicinity of the target, leads to increased ion bombardment events and hence to an increased sputter yield [95]. The efficient ion bombardment allows to use magnetron sputtering at low pressure and low operation voltages, enables high deposition rates, high film adhesion and uniform film deposition on large substrate surface areas [92].

## 2.5 Thin film deposition, growth and nanostructure formation

A neutral atom that approaches a surface within a few atomic distances will be attracted by the Van-der Waals force and follow a potential well downwards [96]. In the immediate vicinity of the surface, however, it gets repelled from the potentials of the nuclei. An atom that does not have enough energy to escape the well is trapped in this potential and referred to as an adatoms. If it is physisorbed, the weak bond to the surface allows the adatom to migrate [96] and diffuse in a random walk [97]. Surface diffusion increases with increasing substrate temperature and the introduction of ion bombardment during deposition and is hindered by surface diffusion barriers. An example of a diffusion barrier that is located at steps is called the Ehrlich-Schwoebel barrier and can impede interlayer "down-hill" diffusion [98]. Adatoms can be further trapped at active surface sites such as atomic steps, impurities or crystallographic defects.

These adatoms can nucleate and form nanoparticles. There is a critical size for a nanoparticle where smaller particle spontaneously decompose while particles exceeding this critical size are stable and grow. This critical size is caused by a maximum in the free enthalpy as a function of number of atoms in the particle [99].

Two nanoparticles can coalesce to minimize the overall energy which is referred to as Smoluchowski ripening. Very small particles nucleate like liquid drops [100], while for larger, crystalline particles both islands deform elastically and/or diffuse towards each other, form a grain boundary and create a neck connection.

Large immobile nanoparticles can grow on the expense of smaller particles by a process called Ostwald ripening. A nanoparticle is surrounded by a two-dimensional "gas" of adatoms that constantly detach and attach. Small particles are surrounded by a higher density of low coordinated mobile adatoms than larger particles, which drive surface diffusion of adatoms from the small particle to the larger one. This process can also be illustrated as a decrease in the chemical potential of small particle.

### 2.5.1 Thin film growth modes

Surface energy is a key concept in explaining and predicting the wetting of a surface. The atoms in a bulk are bond to each other chemically or by van-der-Waals forces and breaking these bonds requires energy that is stored as surface energy per area.

Three surface energies per area are relevant for thin film growth: the surface energy per area at the interface between the film and the substrate  $\gamma_i$ , the substrate and the vapor phase  $\gamma_s$  and at the film and vapor phase  $\gamma_f$ . The surface energy densities for substrate-vapor and substrate-film interfaces are constants whereas the surface energy density of the film-vapor interface depends on the crystallographic orientation of the film.

The wetting properties of a system is described the surface energies and the wetting angle (figure 2.8). The following consideration assumes no kinetic limitation for the surface diffusion, isotropy of  $\gamma_f$  is [101], a defect free substrate surface and no interface inter-diffusion [102]. The

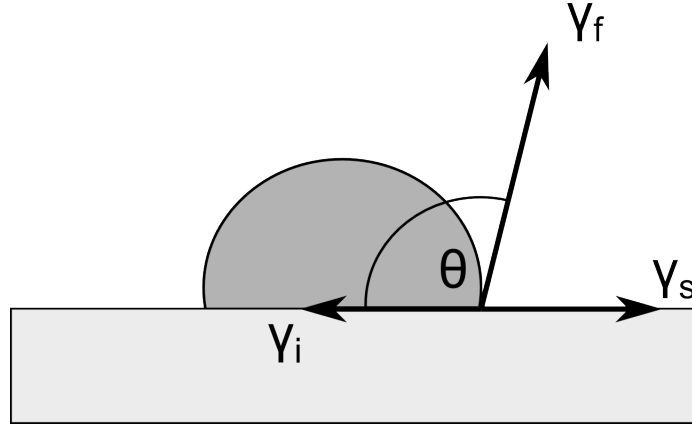


**Figure 2.8:** The wetting behaviour of a film on a substrate is described by the surface energy per areas at the interface between film and substrate  $\gamma_i$ , between the film and the vapour phase  $\gamma_f$ , between the substrate and the vapour phase  $\gamma_s$  and the contact angle  $\theta_{cont}$  (image created after Thompson [101]).

equilibrium shape of a nanoparticle is described by Young's equation:

$$\gamma_i + \gamma_f \cos \theta_{cont} = \gamma_s \quad (2.29)$$

The contact angle  $\theta$  is measured between the film and the substrate surface.

A film wets the support if there is a strong bond at the film-substrate interface. Strong bonds and low  $\gamma_i$  are reached by either a reactive substrate surface or if the substrate and film exhibit similar bond types. A closed film coverage is promoted if the sum of the surface energy per area for the film and the interface is lower than for the bare substrate:

$$\gamma_f + \gamma_i < \gamma_s \quad (2.30)$$

This smooth layer-by-layer growth is termed Frank-van-der-Merwe growth (figure 2.9).

On the contrary, Volmer-Weber growth promotes island formation if there is weak interaction between the film and the substrate but a strong bond between the adatoms. This growth is driven by maximizing the area of the substrate.

$$\gamma_s < \gamma_f + \gamma_i \quad (2.31)$$

In the Stranski-Krastanov mode, the adatoms firstly form a closed layer followed by subsequent island growth [102][99][91].

## 2.5.2 Structure zone model

The self-organized structure of a thin film during physical vapor deposition is determined by the homologous temperature, i.e. the ratio of substrate temperature  $T_s$  to film melting temperature  $T_m$  in Kelvin, and by additional energy to activate diffusion processes [91].

In Z1, the  $T_s/T_m$  ratio is low and surface diffusion can be neglected. Hence, the immobile adatoms form plenty nucleation sites that grow to small grains and the film forms amorphous fibrous columns with many defects that are separated by voids that originate from shadowing of the material [91]. An example for this film microstructure is  $\text{TiO}_2$  layer prepared by reactive DC magnetron sputtering and used in this work as a nanoparticle support.

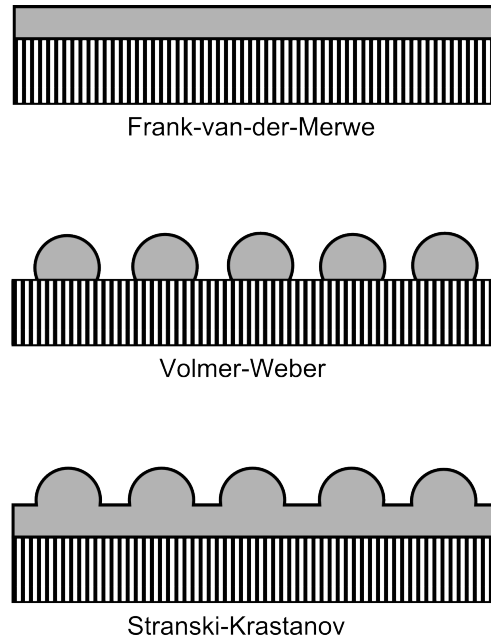


**Figure 2.9:** Three thin film growth modes are distinguished: Frank-van-der-Merwe, Volmer-Weber and Stranski-Krastanov mode. Image created after Grabow and Gilmer [103]

An additional mode, the ZT, evolves with the introduction of energy to the film for instance during sputter deposition that increases the mobility of the adatoms as well as the nucleation rate [100]. There is still no surface diffusion and the columns possess defects. However, no domes or voids are formed.

An increase in the substrate temperature to approximately  $T_s/T_m > 0.3$  enables surface diffusion and zone Z2 develops. Columns are still formed but they are separated by dense grain boundaries and not voids. They show less defects and exhibit typically facets at their surface.

A homologous temperature of  $T_s/T_m$  reaches  $> 0.5$  starts bulk annealing. The film shows isotropic crystallite shapes and the surface is smooth except for grooves at the grain boundaries [104].

### 2.5.3 Solid state dewetting

Thin solid films that are annealing well below their melting temperature can form isolated particles by thermally induced atomic diffusion in a process called solid state dewetting. This process is driven by a minimization of surface energy densities that results in the formation of equilibrium shapes [105][106][107].

Thin films deposited at room temperature do commonly not appear in their equilibrium shape but possess large surface-to-area ratios with varying chemical potentials at the surface. Those gradients in chemical potentials induce capillary forces that drive a mass flow in order to establish an equilibrium.

Therefore, solid state dewetting of thin films starts at surfaces with high curvatures because the chemical potential is proportional to the curvature for isotropic materials. Surface diffusion transports material from the edge (having a high curvature) to the flat surface near the edge until

the wetting angle at the three-phase-boundary reaches the equilibrium angle in a process called edge retraction. The rim thickness increases and a valley is formed behind the rim [26] that can finally touch the substrate and lead to film pinches-off in a mechanisms called mass shedding. The repeated processes of edge retraction, rim formation and film pinch-off could result in the formation of isolated nanoparticle.

Different crystallographic orientation of the film near the edges could introduce irregular edge retraction and the formation of fingers, called "fingering instability", that can further undergo Rayleigh instabilities and segregate into isolated nanoparticles. Anisotropic materials can further form stable facets at the edges that reduces the retraction and is referred to as "faceting instability".

The topics of nanoparticle preparation, localized surface plasmon resonance (LSPR) of metal nanoparticles and their role played in photoelectrochemistry and photocatalysis have been widely investigated. Research has been done for thin film growth of both Au and Ag by using e.g. thermal evaporation or sputtering. To alter their structure and morphology they were exposed to high temperatures. It was found that the properties of the particles such as their shape, symmetry, size and size distribution as well as their interaction with the surrounding medium have a huge influence on the number of LSPR peaks, their positions and widths. In the last two decades, much research has been done to take advantage from the catalytic properties of metal nanoparticles as well as plasmon-induced charge generation.

## 3.1 Au nanoparticles preparation

### 3.1.1 Deposition

Schaub et al [108] deposited thin Au films on glass by evaporation and noticed the formation of electrically continuous films only above 10 nm thickness.

The group around Ballarin [109] used radio frequency sputtering at 60°C to deposit Au nanoparticles and manipulate their dimensions only with the deposition time. The Au nanoparticles were distributed homogeneously over the electrode and their morphology was strongly influenced by the ITO substrate. Increasing the deposition time led to an increase in particle size and a transformation from spherical to slightly elliptical shapes due to aggregation.

Chen et al. [110] annealed thin continuous Au films to form isolated nanoparticles. An initial layer thickness of 5 nm led to the formation of spherical particles between 25-50 nm. An increase in initial film thickness to 10 nm resulted in irregular shaped particles with an increased size distribution of 40-95 nm while the height of the particle was found to be 20 nm. The highest Au amount with a nominal layer thickness of 20 nm resulted in elongated nanostructures of 120-300 nm. It was observed that an increase in film thickness increased the particle separation and decreased the substrate coverage. Increasing the Au amount led to a red-shift of the LSPR from 600nm to 700nm as well as a broadening of the peak which was ascribed to an increase in particle size and size distribution, respectively.

### 3.1.2 Annealing

To investigate both film growth as well as the effect of thermal annealing, Zhang et al. [111] thermally evaporated thin Au films on  $\text{TiO}_2$  (110). For a nominal layer thickness below 1.5 nm, circular droplet-like islands appeared that could be described by the Vollmer-Weber growth mode. Increasing the Au layer led to worm-like nanostructures due to partial coalescence. At layer thicknesses of 8.5 nm, percolation was observed and from 12 nm on a rough but continuous film was found. By increasing the Au layer thickness, a decrease in island density was observed. Furthermore, after reaching a thickness of 1.5 nm, they found saturation in particle separation. Annealing decreased the substrate coverage and increased the particle size that was attributed to Ostwald ripening and island thickening. As a result of thermal annealing, facet structures having mostly hexagonal shapes were observed. Moreover, it was found that deposition on oxygen-deficient substrates led to smaller particle size and higher density than at stoichiometric titania and heterogeneous nucleation was assumed.

Moreover, deposited thin Au films on glass substrates using diode sputtering were used by Siegel et al. [10] to analyse their behaviour after thermal annealing at 300°C for 60min. 15 nm thick Au films were found to form worm-like structures that transformed to large isolated electrically non-connected metal islands under post-annealing. The authors suggested enhanced diffusion rate and coalescence to appear at high temperatures. For 71nm, film thickness discontinuous Au films with cracks are visible under SEM that formed a smoother film with large solitary holes after annealing.

### 3.1.3 Facetting

Wang et al. [112] investigated the effect of the annealing temperature on chemically prepared Au nanoparticles. Therefore, TOAB-stabilized Au nanoparticles of spherical shape with less than 10% of them showing facets were prepared. They observed that annealing at 100°C for 30min led to the formation of facets in nearly all particles. HRTEM analysis found single crystalline particles with a corresponding shape of cubo-octahedron, cube and isocahedron with 111 and (100) facets. They argued that thermal annealing reduces the high surface energy of the as-synthesized spherical particles by introducing facets with low energy surface energy, which are 111 followed by 100, respectively. Besides, elongated particles as well as particles with twinning defects are observed. At 300°C the nanoparticles are found to coalesce into elongated, bigger ones showing twinning. In further experiments, an increase in annealing time at a temperature of 200°C resulted in particles that were more elongated and larger, hence, a greater coalescence was achieved.

## 3.2 Localized surface plasmon resonance

Metal nanoparticles exhibit localized surface plasmon resonance (LSPR) in the visible and near-infrared light that could be observed as strong extinction in UV-Vis spectroscopy. The number of absorption peaks, their position and broadening are dependent on the particles properties such as shape, size and size distribution and composition. Furthermore, the optical spectra of nanocomposites are severely determined by the refracting index of the supporting or enfolding matrix, e.g. a semiconductor like titanium dioxide.



### 3.2.1 Increase in Au loading

Naseri et al. [113] prepared Au:TiO<sub>2</sub> nanocomposites by a sol-gel method and investigated their properties as a photoanode. Upon thermal annealing, an increase in LSPR peak intensity and a red-shift was observed and explained by Au particle formation and agglomeration. Au:TiO<sub>2</sub> nanocomposites with low Au loading up to 1% did not show a plasmonic peak. A further increase in Au concentration led to the formation of LSPR peaks with increasing intensity at the same spectral position. From the single absorption peak, the authors suggested the presence of spherical particles. It was further found that an increase in Au loading led to a decrease in band gap energy for the composite from 3.3 eV for pure TiO<sub>2</sub> down to 2.5eV for samples containing 10% Au.

To distinguish between plasmonic and catalytic effects of metal nanoparticles Haro et al. [114] prepared spherical Au nanoparticles of approximately 9nm size that are embedded in TiO<sub>2</sub>. UV-Vis measurements showed a symmetrical LSPR absorption peak at 548nm that gained in amplitude by increasing deposition cycles but did not shift in position. This suggested that the additional particle all had the same size and were uniformly distributed throughout the titania matrix with enough distance to prevent plasmonic coupling.

The possibility that the red-shift is caused by the simple increase in particle size is a controversial debate in the literature. Kang et al. [22] and Ballarin et al. [109] argued, their observed red-shift is related to an increase in nanoparticle diameter. Kelly states in his feature article that the oscillation frequency is dependent on the size of the charge distribution [115]. In more detail he states that the LSPR gets red-shifted if the particle size increased over 30 nm [115]. They argued that although the quasistatic theory is size-independent, a correction (dynamic depolarization) introduces a red-shift to this theory [115]. Huang says that an increase in particle size increases its polarizability (by the cubic power) [116]. Haiss argued that the LSPR only depend on particles with diameters smaller than the electrons mean free path lengths [117]. Baset on the other hand used the width of the Lorentz profile on Ag particle absorption for the determination of the nanoparticles size [118]. He argued that the plasmon width is determined by  $\epsilon_2$  and thus on the particle radius [118]. Peng reported an interesting behaviour in the small Ag nanoparticle regime: for nanoparticles smaller than 20 nm the LSPR blue-shifted and starts to strongly red-shifted for sizes lower than 12 nm [119]. They explained this phenomenon by a loss of electron conductivity at the outmost Ag atomic layer because of chemical interaction. However, an increase in size should not influence the LSPR position and only lead to a broadening.

### 3.2.2 Influence of titania

Au loaded TiO<sub>2</sub> thin films were prepared by Deki et al. [120] using a liquid-phase deposition. Increasing the annealing temperature led to an increase in particle size distribution. A red-shift in LSPR was observed for increasing thermal annealing temperature that was explained by the change in refractive index/relative permittivity of the semiconductor during transformation from amorphous to anatase phase.

Buso et al. [121] prepared Au/TiO<sub>2</sub> composites using a sol-gel method to introduce 10 nm sized Au nanoparticle into a titania matrix. They observed a red-shift of the plasmon-induced absorption peak of the composite material compared to the same Au nanoparticles in aqueous solution. This was related to the higher refractive index of the TiO<sub>2</sub> matrix. Increasing the annealing temperature led to an increase in red-shift for the LSPR position. For thermal annealing at 400°C the plasmon related peak was found at 604nm. Since the Au nanoparticles showed no altering in shape or size in TEM observations and a constant FWHM on the corresponding peaks in XRD, the observed red-shift was correlated to a change in the refractive index of TiO<sub>2</sub>. An increase in Au concentration led to an enhancement in absorption peak but not in peak position.

The later phenomenon was explained by the low doping of the Au nanoparticles and hence the missing coupling of the plasmon with the titania.

Furthermore, a colloidal technique was used by Gaspera et al. [122] to prepare Au/TiO<sub>2</sub> thin films. The increase in annealing temperature is accompanied with a red-shift of the plasmon resonance peak for Au. No morphological change in the Au particle during annealing was observed by the authors that related the red-shift to the measured increase of the refractive index of the titania matrix, fully covering the nanoparticle, due to film densification. A comparison of the refractive index measured experimentally for the titania matrix with the calculated refractive index from the LSPR position using Mie theory, suggested that the porous TiO<sub>2</sub> is denser around the Au nanoparticles. Since both, calculated and experimentally determined refractive index increase in difference as the annealing temperature is raised, it was suggested that the contact area between Au nanoparticles and titania matrix increase. Furthermore, an increase in temperature leads to a broadening in the LSPR peak. Since no particle agglomeration was observed, this observation was taken as further evidence for an increase in interaction between Au and TiO<sub>2</sub> by increasing their interface.

### 3.2.3 Non-spherical shape

To investigate their applicability in NO oxidation, Bannat et al. [123] prepared Au-TiO<sub>2</sub> nanocomposites by either impregnating a mesoporous titania matrix with spherical Au nanoparticle or by using pulsed cathodic electrodeposition to produce dendritic Au nanostructures. For the spherical particles synthesized by impregnation, no red-shift of the plasmon resonance absorption band as a result of interaction with the semiconductor was observed. In contrast, dendritic Au structures grown by pulsed electrodeposition exhibit a strong plasmon peak with a maximum at 590 nm which was explained by excitation of longitudinal plasmons in addition to the transverse mode.

## 3.3 Bimetallic Au-Ag nanoparticles

Bimetallic nanoparticles have been prepared as alloy [124][125], Au-core Ag-shell [124][126][127] [34][128] [129][130][131] [132][133][134][135][136][137] and Ag-core Au-shell nanoparticles configurations [54][125]. A common method to confirm core-shell formation is by contrast differences in TEM [127].

Alloy have been prepared by a simultaneous reduction of Au(III) and Ag(I) ions [125], by laser ablation, galvanic replacement or digestive ripening. The method of digestive ripening was even used to form alloys from previous core-shell structures [124].

The preferred method for homogenous core-shell nanoparticles is the reduction of Ag on pre-formed Au seeds. The reduction can occur in the presence of chemicals such as citrate, borohydrate, ascorbic acid or Neem leaves or due to laser heating, UV light and microwave [138]. Another approach is the electro-deposition of Ag layer onto Au nanoparticles [126]. The shape of the Au core strongly determines the shape of the Ag layer [127]. Ag nanoparticles have stronger LSPR enhancement, Raman enhancement, refractive index sensitivity and solar energy conversion efficiency than Au nanoparticles [34]. However, homogenous monodisperse synthesis is challenging [131][135]. Homogenous Au nanoparticles preparation on the other hand is established. Therefore size and shape controlled Au nanoparticles are used as seeds for Ag reduction. The bimetallic nanoparticles exhibits Ag-like optical behavior due to the dominant shell metal [34]. Au-core Ag-shell particles have been synthesized as nanocubes [129], nanoprisms, nanorods and decahedron, octahedral, nanorods, nanodumbbells, nanoshuttel citeBai2014 and nanoboats. The Ag shell is protected from oxidation by charge transfer with the Au [139].

The opposite configuration of forming a Au shell on Ag seeds is challenging, because chemically prepared Ag nanoparticles are commonly polydispers and easily oxidize [124][34][131]. Nevertheless, Ag seeds were synthesized by reducing  $\text{AgNO}_3$  and the Au shell was added by subsequent reduction of  $\text{HAuCl}_4$  with oleylamine (oleylamine was used both as a reducing agent and stabilizing surfactant) [140]. Au shells are easily grown on Ag by galvanic replacement reaction [129]. Calculations showed, that the formation of a Au shell around a Ag core is preferred upon the reverse configuration [141].

Beside Au, Ag is often used in metal oxide composites. Therefore, Adochite et al. [142] prepared Ag: $\text{TiO}_2$  nanocomposites by reactive DC magnetron sputtering. Upon annealing, the authors noticed diffusion from Ag nanoparticle both to the  $\text{TiO}_2$ -substrate interface and to the semiconductor surface and concluded enhanced diffusion through the matrix at elevated temperatures. Furthermore, the particles grew irregular in shape and increased in size distribution.

Intense investigations were carried out to understand the growth of metal thin films from isolated island that become connected with increased deposition to finally form an electrically continuous films. The structure and morphology of the films could be altered by thermal annealing. In the stage before percolation, thermal treatment was found to lead to an increase in particle size and a decrease in substrate coverage as well as the appearance of facets.

Ag nanoparticles were prepared by Renteria-Tapia et al. [143] after thermal annealing of a Ag ion containing silica film first in hydrogen- and subsequently in oxygen containing gas. It was found that annealing in a reducing atmosphere leads to a blue-shift of the Ag nanoparticle absorption peak in contrast to annealing under oxygen atmosphere which results in a red-shift. The red-shift and damping was explained by the formation of Ag-core  $\text{Ag}_2\text{O}$ -shell structures detected by HRTEM images. From calculations they expect, that annealing either in oxygen or hydrogen-rich atmosphere does not alter the size and shape of the Ag nanoparticles. However, annealing in oxygen leads to the formation of a  $\text{Ag}_2\text{O}$  shell that increases until saturation is reached, determining the optical properties of the particles.

Banerjee et al. [144] chemically prepared Au@Ag core shell nanoparticles to invest their antibacterial activity. Upon increasing the thickness of the Ag shell, a blue-shift of the absorption band for pure Au nanoparticles from 520nm to 420nm was observed. The existence of a single LSPR peak in contrast to two peaks corresponding to the plasmon resonances of Au and Ag was seen as evidence for the formation of core-shell nanoparticles. TEM revealed that, although the particles were spherical, the Ag shell did not grow uniformly around the Au seed. However, no mono-metallic Ag particles were detected.

The possibility to specifically modify the absorption properties of nanocomposite materials entailed much research in the last decades. The interaction of plasmonic nanoparticles with the supporting semiconductor was used to shift their absorbance to visible or near-infrared regions. Combinations of Au and Ag either as alloy or as core-shell nanoparticles were investigated for LSPR peak-shifting. It was further shown that non-spherical symmetries e.g. triangles and cubes or hollow nanostructures add more degrees of freedom for nanoparticle engineering.

Kracker et al. [20] sputtered Ag and Au thin layers on soda-lime glass and observed the formation of isolated alloy nanoparticles after thermal annealing at 400°C for 1h. They observed the formation of a single absorbance peak that was attributed to the excitation of localized surface plasmon resonance of the alloy. The position of the LSPR peak shifted by varying the elemental metal ratio. However, they observed that the deposition of a thin Ag layer on top of a Au layer prevented the formation of an alloy that was ascribed to the oxidation of the Ag layer during thermal annealing in air.

Zhu et al. [145] simulate the optical response of elongated Au-Ag core-shell nanoparticles. Pure Au nanoparticles with an elongated shape exhibit transverse and longitudinal LSPRs that both

get blue-shifted and more intense at deposition of a Ag shell. Moreover an additional plasmon peak corresponding to the longitudinal mode of the just formed Ag shell is established at low wavelengths. This additional peak gets red-shifted and more intense by an increase in Ag shell thickness. The transverse mode belonging to the Ag shell is assumed too weak to be observable in the experiment.

Ag-Au alloys were prepared chemically e.g. by reduction of chlorauric acid ( $\text{HAuCl}_4$ ) and  $\text{AgNO}_3$  with sodium citrate as was done by Link et al. [146]. The alloy formation was confirmed by the appearance of only one plasmon peak that shifted towards smaller wavelengths with increasing Ag content.

Lu et al. [134] used a similar protocol to synthesize Au-core Ag-shell nanoparticles. First Au seeds were precipitated by reducing  $\text{HAuCl}_4$  with ascorbic acid followed by a reduction of  $\text{AgNO}_3$  to form a Ag shell. An increase in Ag amount led to a blue-shift of the LSPR peak induced by the Au core and the formation of an additional peak characteristic for Ag nanoparticle LSPR.

Csapo et al. [125] prepared both Ag/Au alloy particles as well as Ag-Au core-shell nanoparticles by chemical reduction. The plasmon resonance of the alloy particles could be shifted between the LSPR of pure Ag and Au, respectively, by variation of their metal composition. The absorbance of Ag nanoparticles shifted to longer wavelengths with increasing thickness of the coated Au shell.

Radio frequency magnetron sputtering was used by Barreca et al. [147] to sputter Au thin films on silica followed by Ag deposition and thermal annealing at  $500^\circ\text{C}$  for 3h under nitrogen or 4%  $\text{H}_2/\text{N}_2$  atmosphere, respectively. This process enabled the synthesis of Au-Ag alloy nanoparticles which was suggested by the presence of a single LSPR peak. In agreement with other research, an increase in LSPR intensity and a blue-shift was observed with increasing Ag content. Furthermore they observed a more extensive alloying under 4%  $\text{H}_2/\text{N}_2$  atmosphere that they explained by the reduction of  $\text{Ag}(1)$  to  $\text{Ag}(0)$ .

### 3.4 Photocatalysis and photoelectrochemistry

Metal/semiconductor systems such as Au nanoparticles deposited titania have been intensively investigated since 2006 for applications such as NO and  $\text{H}_2\text{O}_2$  degradation, glucose sensing or water splitting. The enhanced photoactivity could be attributed to particle morphology, the resulting plasmonic properties and the interaction between the particle and the matrix.

#### 3.4.1 Mechanism

Tatsuma et al. [148] decorated nanoporous  $\text{TiO}_2$  structure with Au nanoparticles. While illuminating with visible light, they saw a negative potential shift and observed a correlation between the action spectra and the absorption. They proposed, that electrons from the Au nanoparticles are transferred to the  $\text{TiO}_2$ . The present electron donor  $\text{I}^-$  subsequently injects electrons to the metal nanoparticle. Tatsuma clearly differentiates this mechanism from the image of Au nanoparticles as an electron sink as was suggested in previous publications. This paper is cited by many groups.

Cronin et al. [65] argues that charge transfer cannot drive reduction or oxidation half-reactions. Metal nanoparticles do not possess HOMO-LUMO for cluster sizes needed to exhibit LSPR.

This research was extended by variation of different electron donors. In 2005 Tatsuma et al. [149] showed an IPCE of 26% for Au- $\text{TiO}_2$  samples with the addition of  $\text{Fe}^{2+/3+}$  as an electron mediator. They underlined the importance of an electron donor. Without a donor, the electrons injected from the metal nanoparticle to the semiconductor would gradually migrate back.

Au-loading enhanced the photocatalytic oxidation of NO compared to the pure semiconductor sample. It was suggested by Bannat et. al. [123], that the formation of a Schottky barrier between

the metal nanoparticle and the semiconductor led to a separation of the photogenerated charges. Electrons might be trapped at the metal nanostructures whereas the holes reacted with  $\text{OH}^-$  or water molecules at the surface to form hydroxyl radicals for the decomposition of NO. By comparing two samples with the same Au loading but prepared by either impregnation or pulsed electrodeposition, the same efficiency in NO oxidation was found. It was concluded, that the morphology of the particles had no effect on the investigated photocatalytic activity of the samples. Increasing the Au-TiO<sub>2</sub> ratio led to a decrease in activity that was attributed to Au nanostructures blocking the pores of the TiO<sub>2</sub> for the gas. Furthermore, enough electrons might be captured in the metal; hence, no more photogenerated charges were able to be injected into the nanostructures.

Yoko et al. [150] observed an increase in anodic photocurrent for both Ag and Au particles embedded in TiO<sub>2</sub> under visible light. However, under UV light the anodic photocurrent decreased for Au/TiO<sub>2</sub> and showed an initial increase followed by a decrease for Ag nanoparticle with increasing loading. The authors listed several beneficial mechanisms that are expected to increase the photocurrent: the catalytic effect of metal nanoparticles, the introduction of surface states and LSPR excited electrons. The photocurrent could be decreased due to the reduced mobility of the electrons due to the presence of the Schottky barriers at the interface of the embedded metal nanoparticles in the bulk (retarded transfer) as well as recombination at the introduced surface states.

Photoelectrochemical measurements using 1M H<sub>2</sub>SO<sub>4</sub> as a cathodic and 1M KOH as an anodic electrolyte showed an increase in photocurrent at positive potentials for Au-loaded TiO<sub>2</sub> compared to pure titania under visible light. The authors [113] claimed that the addition of the metal nanoparticles increased the conductivity of the composite, supporting the transfer of charges through interfaces. Moreover, the observed decrease in band gap enhanced the light absorption and hence the amount of photogenerated charge carriers. An additional beneficial effect stems from the formation of a Schottky barrier that promotes charge separation. O<sub>2</sub> evolution therefore takes place both at the TiO<sub>2</sub> and the Au nanoparticles, the latter acting as a catalyst. Analysis of I-t measurements enabled the authors to calculate transient times. They found that an increase in Au concentration decreases the transient times, hence, promotes recombination. Comparing the photoelectrochemical activity of Au:TiO<sub>2</sub> composites with increasing Au content showed an optimum at 5% Au with the photocurrent decreasing with lower and higher concentration. This phenomenon was explained by the balance of positive contributions of Au (enhanced absorption, conductivity) with the negative ones (coverage of TiO<sub>2</sub> surface, enhanced recombination due to particle agglomeration).

TiO<sub>2</sub> nanotubes were electrodeposited with Au nanoparticles and investigated by Jana et al. [151]. During deposition, a reduction peak for  $[\text{AuCl}_4]^-$  to Au was observed at -1.08 V vs Ag/AgCl as well as a corresponding oxidation peak at -1.0 V vs Ag/AgCl. A LSPR peak at 530nm established and the peak broadening was explained by the authors due to the presence of titania. Under visible light, I-V curves revealed an enhancement of the photocurrent for Au loaded TiO<sub>2</sub> nanotubes compared to pure TiO<sub>2</sub> which was reasoned by the authors as an enhancement in electron/hole pair generation and separation. The onset of the cathodic current was attributed to the reduction of Na<sup>+</sup> ions coming from the Na<sub>2</sub>SO<sub>4</sub> electrolyte and its participation in a Helmholtz double layer. Mott-Schottky analysis revealed that the Au-TiO<sub>2</sub> samples had a higher charge carrier density and more efficient charge separation and transport characteristics than the pure TiO<sub>2</sub>, the two last ones being held responsible for the high photoactivity. Chopped white light illumination at 0.8V vs Ag/AgCl showed also an increase in photocurrent for nanoparticle decoration which was attributed to an increase in amount of charges due to the introduction of Au. It was concluded, that upon plasmon excitation, electrons were injected into the TiO<sub>2</sub> whereas the missing electrons in the metal nanoparticles were refilled by electron donors present in the

electrolyte. The electric field enhancement at the metal surface was thought to support charge separation at the metal/semiconductor interface. Moreover, the presence of Au makes the charge transfer between electrode and electrolyte easier.

In a paper published in 2006 Yu et al. [152] explored the effect of the Au nanoparticle size on  $\text{TiO}_2$  on its activity. Under visible light illumination, Au loading enhanced the anodic photocurrent of the  $\text{TiO}_2$  sample. Comparing the photocurrent measured at different Au loadings, an optimum could be found which was explained by the balance of advantageous increased absorption and disadvantageous increase in shadowing of the nanoparticles and increased scattering as the size increases. The authors argued that large particles are advantageous because their high contact area leads to a wider space charge layer to separate the charges, however, a particle size of 15nm in diameter was proposed to be the best under investigation. A match between IPCE spectra and absorbance spectra was interpreted by the authors as evidence for plasmon induced photocurrent enhancement.

### 3.4.2 Hot electron injection

Under UV light, Au decoration decreased the photocurrent generation of  $\text{TiO}_2$  that was explained by Chen et al. [110] by the coverage of active surface sites of the  $\text{TiO}_2$  that are in direct contact with the electrolyte and furthermore shield these areas from light. Under visible light, pure  $\text{TiO}_2$  showed a very low photoactivity which was correlated to the low absorption in this region. Au-deposition resulted in a great enhancement of the photocurrent under visible light. This phenomenon was ascribed to LSPR that could on the one hand lead to electric-field enhancement at hot spots and could on the other hand transfer hot electrons from the metal NP to the CB of the  $\text{TiO}_2$ . Comparing the photocurrent generation of different Au amounts, an optimum for 10 nm initial layer thickness was found. This was motivated by the authors as reaching an equilibrium between LSPR intensity and particle density. A match between absorption and IPCE spectra indicated that the LSPR is responsible for the enhancement under visible light. Furthermore, Au loading showed improved hydrogen evolution under UV-visible light.

Wu et al. [153] used a hydrothermal synthesis for the preparation of  $\text{TiO}_2$  nanotubes that were deposited with Au nanoparticles by seed mediation. Au deposition enhanced the photocurrent measured under visible light. A strong match between IPCE action spectra and the corresponding extinction spectra lead the authors to the conclusion, that LSPR was responsible for the enhancement. Photocurrent enhancement were observed for wavelengths with energies that are lower than the band gap of the  $\text{TiO}_2$ . The author concluded that hot electron injection took place since an enhancement from electric field generation or scattering would only work at higher energies.

Moskovits argued that electrons from plasmon decay can be injected to the semiconductor via quantum mechanically tunneling through the Schottky barrier [154].

### 3.4.3 Electric field enhancement

An increase in photocurrent or photocatalysis was ascribed by several authors to plasmon-induced electric field enhancement.

Zhang et al. [155] suggest both electron injection as well as electric field enhancement possible in their Au- $\text{TiO}_2$  bilayers. The close contact between both metals, a plasmon energy that exceeds the Schottky barrier as well as visible light absorption of  $\text{TiO}_2$  due to defects in the semiconductor are given as arguments.

### 3.4.4 Catalytic effect of metal nanoparticles

In J-V curves a cathodic current observed below 0.4V vs RHE was attributed by Haro et al. [114] to the reduction of oxygen to  $\text{OH}^-$ . A distinct cathodic peak at 0.02 V vs RHE was related to the transfer of electrons through an inter-bandgap state in the  $\text{TiO}_2$  during the potential sweep. This peak lost its dominance under illumination that was explained by recombination of photogenerated holes with the electrons present in those states. Furthermore, an increase in anodic photocurrent was observed for Au-decoration. Regarding the enhancement of photocurrent, an optimum in Au-loading was found. The observed decrease in photoactivity for a high Au content was related to the coverage of titania active sides, shadowing from incident light and increased recombination at the metal nanoparticles. To exclude the effect of the  $\text{TiO}_2$  substrate, a UV-filter was used. No enhancement in IPCE at the LSPR wavelength could be observed which led the authors to the conclusion that LSPR did not contribute to the photocurrent. The observed low enhancement in photocurrent for the presence of Au nanoparticles still observed under visible light was attributed to a catalytic effect of the metal nanoparticles. Additional EIS analysis revealed a decreased charge transfer and charge transport resistance for Au: $\text{TiO}_2$  samples.

Li et al. [156] created  $\text{TiO}_2$  (rutile) nanorods that were grown on Au-covered FTO and finally deposited with Au NP by electrodeposition and described them as Au/ $\text{TiO}_2$ NRs/Au. Under visible light Au loading increased the photocurrent generation up to a point, when additional Au loading did not give further significant enhancement. Likewise, Au deposited  $\text{TiO}_2$ -NR exhibited more photocurrents than pure  $\text{TiO}_2$  NRs under UV light. The Au between the FTO and the  $\text{TiO}_2$ NRs enhanced the performance of Au/ $\text{TiO}_2$ NRs both in the visible and UV light. This was attributed by the authors to a faster electron transport. However, pure  $\text{TiO}_2$ NRs are superior under UV light to those NRs grown on Au NP, because Au decorated FTO substrates led to the growth of less dense titania NRs.

Khan et al. [157] observed a decrease in band gap from 3.1eV for P25  $\text{TiO}_2$  to 2.4eV for Au nanoparticle deposition. They concluded that new atomic energy levels in the band gap below the conduction band of the  $\text{TiO}_2$  were formed. Au@ $\text{TiO}_2$  nanocomposites enhanced the photocatalytic reduction of methyl orange under visible light that was attributed to the increased absorption due to LSPR and the observed band gap decrease. Cyclic voltammetric measurements at a scan rate of 0.05V/s, oxidation and reduction peaks at -0.062V vs Ag/AgCl and -0.89V vs Ag/AgCl, respectively, were only observed in the presence of Au. Furthermore, EIS measurements detected a decrease in resistance for Au@ $\text{TiO}_2$  composites.

To investigate the ability of Au- $\text{TiO}_2$  systems to produce hydrogen Jose et al. [158] deposited Au nanoparticles via solvated metal atom dispersion onto different types of titanium dioxide, namely anatase, rutile and P25 (75% anatase, 25% rutile). Under UV-visible light using sacrificial electron donors, the presence of Au led to higher hydrogen evolution compared to pure  $\text{TiO}_2$ . It was stated, that the holes produced in the semiconductor were consumed by the sacrificial agent whereas the photogenerated electrons were captured by the Au nanoparticles. They acted as electron sinks because their Fermi level were more positive than the conduction band of titania. Therefore, the metal nanoparticles were active centers for the hydrogen catalysis. When cutting off wavelengths below 400nm only titania in the rutile modification was still photoactive and the observed enhancement effect of Au on rutile was explained as before. By dismissing sacrificial agents they still observed enhanced hydrogen production for Au decoration under UV-Visible light, confirming their hypothesis, that Au nanoparticle act as an electron sink for the photogenerated electrons in the semiconductor. In this scenario, the generated holes are now captured by water molecules. However, even though no hydrogen was generated with pure P25 without a sacrificial agent, the presence of ethanol led to a small activity. They concluded, that charge separation for

titania needs either sacrificial agents or metal nanoparticle acting as electronic sinks.

### 3.4.5 Photoelectrochemical characteristic

In the work of Ballarin [109], Au nanoparticles were deposited on ITO. At a scan rate of 50 mV/s and in a 0.5 M KOH electrolyte, a wide oxidation wave at +0.32-0.4 V vs SCE and a reduction peak at +0.00 V vs SCE was observed. These peaks were associated with the formation of Au oxides and their subsequent reduction in the cathodic sweep.

Kenanakis et al. [159] prepared TiO<sub>2</sub> thin films by sol-gel deposition without additional sensitizer. Cyclic voltammetry using NaOH as electrolyte and Ag/AgCl as a reference electrode showed cathodic peaks between -700mV and -1250mV that were interpreted to be due to irreversible sodium intercalation into TiO<sub>2</sub>. Addition of methanol broadened these peaks. Generally, the presence of methanol led to an increase in photocurrent under UV light that was attributed to refilling of holes. They further concluded that TiO<sub>2</sub> with high crystallinity as well as high surface area is advantageous for electrooxidation.

To reveal the influence of the Au-TiO<sub>2</sub> interface Rodriguez et al. [160] investigated Au nanoparticles on different supporting material as well as the reverse system of TiO<sub>2</sub> nanoparticles on Au electrodes. A polycrystalline Au electrode showed two oxidation peaks at 1.4 V vs RHE and 1.6 V vs RHE as well as a reduction peak at 1.18V vs RHE that were attributed to Au surface oxide generation and its removal. Au nanoparticles, however, showed a broad "oxidation wave" that was additionally shifted towards more positive potentials independent on the supporting substrate. A difference in cathodic peak position as well as the missing first oxidation peak were attributed by the authors to contamination of the substrates. Independent from their substrate, Au nanoparticles showed a lower onset potential for CO oxidation compared to bulk Au electrodes, which was associated with the high activity of low coordinate sites at the nanoparticles. There is an electron transfer from the TiO<sub>2</sub> to the Au nanoparticles that results in the transfer of oxygen vacancies from the interior of the semiconductor towards the surface. By depositing TiO<sub>2</sub> nanoparticles on a Au electrode, it was observed that the Au oxide peak is shifted to positive potentials with increasing TiO<sub>2</sub> amount. The authors claimed that Au NP/TiO<sub>2</sub> and TiO<sub>2</sub> NP/Au systems are equal, leading to the conclusion that the catalytic activity of such systems is founded in their interfacial interaction and not a consequence of Au size.

Hussain et al. [161] prepared Au loaded TiO<sub>2</sub> microspheres by hydrothermal synthesis for hydrogen peroxide degradation and non-enzymatic glucose detection. Under UV light, Au/TiO<sub>2</sub> nanocomposites were faster in RhB decomposition than pure TiO<sub>2</sub>. This was attributed by the authors to the high surface area and good charge separation for Au/TiO<sub>2</sub> composites. Cyclic voltammetry showed the appearance of oxidation and reduction peaks at 0.45 V vs Hg/Hg<sub>2</sub>SO<sub>4</sub> and 0.01 V vs Hg/Hg<sub>2</sub>SO<sub>4</sub>, respectively, after Au deposition on TiO<sub>2</sub> coated glassy carbon electrode. Those peaks increased after addition of glucose.



## 4.1 Material and methods

This section describes the devices, substrates and protocols used to manufacture Au-TiO<sub>2</sub> and Au-Ag-TiO<sub>2</sub> systems. The nanoparticles were prepared by a combination of magnetron sputtering and thermal annealing so the used magnetron sputtering recipient and the furnace tube are presented. Commercial fluorine-doped tin oxide coated on sodalime glass was used as a substrate and covered by DC sputtered, spincoated and atmospheric-pressure chemical-vapour-deposition TiO<sub>2</sub>. These TiO<sub>2</sub> samples were used as a support for Au and Au-Ag nanoparticles. The preparation method for the mono- and bimetallic nanoparticles are described below.

### 4.1.1 Magnetron sputter recipient

Nanoparticles were prepared by radio frequency (RF) magnetron sputtering in a low-pressure recipient followed by subsequent thermal annealing. This paragraph introduces the magnetron sputter deposition of Au nanoparticles and ultra-thin Au layers before focusing on Ag, and refers to the following section for details on the thermal annealing.

The recipient (figure 4.1) contained two magnetron sputter sources (figure 4.1). One magnetron was equipped with a 3 mm thick Au disc (MaTeck, purity of 99.999 %) having a 2 inch diameter as well as a 2 inch iron disc (purity of 99.95 %, MaTeck) having a thickness of 1 mm that was inserted between the Au target and the magnetron to reduce the sputter yield. The sample was positioned on a sample holder at a distance of 9.3 cm from the sputter target. The vacuum chamber was evacuated to  $8.3\text{--}7.9 \times 10^{-3}$  Pa before argon was purged for at least an hour at a flow rate of 15 sccm and a gas pressure of 5 Pa. The plasma was ignited in argon atmosphere by applying a power of 48-50 W (70 W was inserted and 20-22 W was reflected). The nominal film thickness of the deposited Au film was controlled by the deposition time.

The second magnetron was equipped with a 3 mm thick Ag target from MaTeck having a 2 inch diameter and purity of 99.999 %. Again, a 1 mm thick iron disc (purity of 99.95 %, MaTeck) was placed between the magnetron and the Ag target to reduce the magnetic field. The target was positioned at a distance of 5.5 cm from the sample holder. Analog to the Au deposition, the vacuum chamber was evacuated and subsequently purged with argon to attain a working pressure of 5 Pa. Ag was deposited at a magnetron power of 49 W with 50 W inserted and 1 W reflected power.

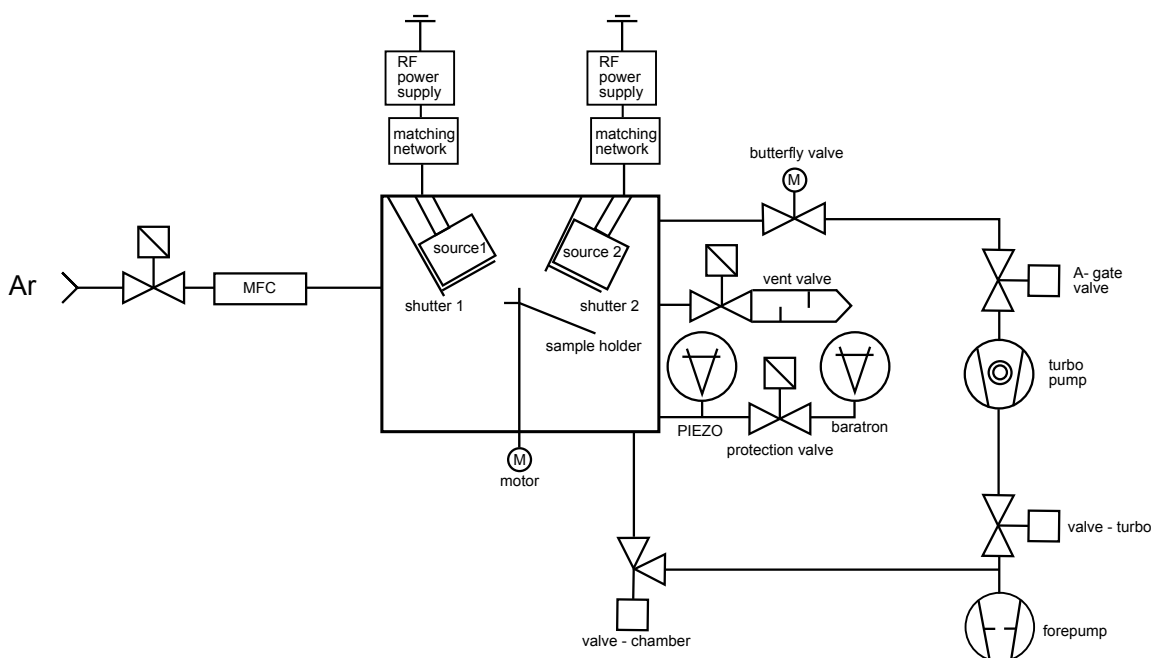


**Figure 4.1:** The plasma recipient used in this study that is equipped with two magnetrons to deposit Ag and Au.

### 4.1.2 Tube furnace

The as-deposited metal/TiO<sub>2</sub> samples were thermally annealed in a tube furnace to alter their nanostructures. For this purpose, the samples were placed on a combustion boat (65563, CoorsTek) made of high-alumina and heated in a Eurotherm 2416-controlled tube furnace. The heating ramp ( $\Delta K/min$ ), gas atmosphere and treatment time was varied for a Au/TiO<sub>2</sub> series discussed in the section 6.2 using parameter ranges described in paragraph 4.2.4. Otherwise, the tube furnace was purged with a 0.050 slm oxygen flow supplied by a multi gas controller 647B (MKS Instruments) both prior to the heat treatment (to ensure pure oxygen atmosphere in the tube) as well as during the annealing. The Au/TiO<sub>2</sub> and Au-Ag/TiO<sub>2</sub> samples were inserted directly into the furnace and remained inside for 30 min at 400°C before they were directly extracted and could cool down in ambient air.

### 4.1.3 Substrates

#### FTO glass

All metal nanoparticles were, unless otherwise stated, deposited on TiO<sub>2</sub>-FTO-glass. The thermally and chemically stable FTO acted as a conductive support for the TiO<sub>2</sub> film and is a transparent conducting oxide. Commercial fluorine-doped tin oxide (FTO, TCO22-7) layer with a surface resistance of 7  $\Omega/sq$  coated on 2.2 mm thick sodalime glass was purchased from Solaronix (Switzerland) and cut into squares with dimensions of 25 mm. The FTO-glass was thoroughly cleaning and all four corners of the FTO samples were covered with cellulose acetate prior to TiO<sub>2</sub> deposition to provide electrical contact for photoelectrochemical measurements.

### **DC sputtered TiO<sub>2</sub>**

TiO<sub>2</sub> was deposited, as described by Kruth et al. [162], using reactive direct current (DC) magnetron sputtering. A cylindrical titanium target (Ti-133, Bekaert Advanced Coatings NV, Belgium) served as a cathode and rotated at a speed of 15 rpm, while the samples were transported at a speed of 17 mm/s on a band-conveyor below the target. The chamber was evacuated to  $2.5 \times 10^{-6}$  mbar base pressure and the oxide layer on the Ti target was removed by igniting the plasma for 5 min at 8 kW in 3 Pa Ar while the samples were protected from sputtered atoms by a shutter. The gas mixture was adjusted to 6 sccm oxygen, 3 sccm nitrogen and 60 sccm argon with a total working pressure of 3 Pa. Importantly, the working point of the magnetron was kept between the metallic and oxidic mode during the deposition and the O<sub>2</sub> partial pressure was kept constant by matching the magnetron power. The deposition was started after reaching 5.6 kW (approximately 450 V). This value increased during the process to 8.2 kW (460 V). Twenty-four loops were conducted to achieve a titanium dioxide nominal layer thickness of 270 nm. All DC sputtered TiO<sub>2</sub> films were annealed under oxygen flow (0.050 slm) at 400°C for 60 min with a temperature ramp of 10 K/min to transform the amorphous as-sputtered titanium dioxide into anatase modification. A lower layer thickness was used for transmission electron microscopy, where a 30 nm thick TiO<sub>2</sub> layer was deposited on silicon nitride TEM grids and subsequently annealed to obtain the anatase phase, as described above.

### **Spincoated TiO<sub>2</sub>**

TiO<sub>2</sub> layers were prepared by sol-gel spincoating onto FTO glass. The FTO glass was thoroughly cleaned and mounted on the spincoater (WS-650SZ-6NPP/LITE, Laurell Technologies Corporation). Each spincoating synthesis consisted of two consecutive steps: the first rotation was performed at a speed of 500 rounds per minute (rpm) with an acceleration of 1000 for 60.0 s, followed by a faster rotation at 2000 rpm for 1 min at the same acceleration. The spincoating solution (Ti-Nanoxide D/SC 15111, Solaronix) consisted of approximately 3%wt opac TiO<sub>2</sub> (anatase) particles with diameters between 15 and 20 nm dissolved in alcohol, water and organic binders. A quantity of 100 µl was applied with a pipette onto the sample before starting the spincoating program. Three TiO<sub>2</sub> layers were coated as described above. After each of the first two layers, the sample was directly inserted to the preheated tube furnace and heated to 150°C for 30 min in oxygen (0.050 slm), while the third layer was annealed at 430°C for 60 min with a temperature ramp of 10 K/min, again under oxygen flow. The combination of the three deposition cycle and the corresponding annealing is stated as "one batch". The titania substrate used in the experiment consisted of three batches to ensure sufficient layer thickness (which adds up to a total of nine spincoating layers for every sample). All four corners of the particular samples were covered with cellulose acetate during spincoating to ensure electrical contact with the conductive FTO glass.

### **Atmospheric-pressure chemical-vapour-deposition (AP-CVD) TiO<sub>2</sub> with various layer thickness**

TiO<sub>2</sub> was synthesized in the anatase modification by Fraunhofer-Institut für Werkstoff- und Strahltechnik IWS Dresden using a self-developed chemical-vapour-deposition process at atmospheric-pressure [163][164]. A titanium-containing precursor and water vapour were introduced to the chamber with a flow velocity of at least 0.5 m/s and reacted chemically on the substrate that had a temperature of 250°C. Titania layers with thicknesses of 400 nm, 600 nm, 800 nm and 1000 nm, respectively, were deposited on FTO glass.

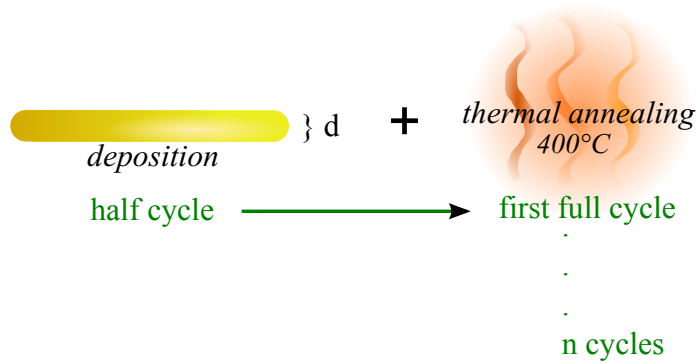


**Figure 4.2:** Isolated nanoparticles are prepared by depositing a thin metal layer with a nominal layer thickness  $d$  on the titania substrate and subsequently anneal the sample at  $400^{\circ}\text{C}$ , which is termed "one cycle". This cycle was repeated in order to increase the Au loading.

Particle diameter	nominal layer thickness $d$ for one deposition	number of cycles $n$
3-20 nm	1.7 nm	1
5-65 nm	6.6 nm	1
4-69 nm	6.6 nm	2
3-94 nm	6.6 nm	4

**Table 4.1:** Different Au loadings and nanoparticle size distributions were realized by varying either the initial nominal Au layer thickness or the number of synthesis cycles.

## 4.2 Sample preparation

### 4.2.1 Preparation of Au nanoparticles on $\text{TiO}_2$

Au nanoparticles were synthesized by a combination of magnetron sputtering and subsequent thermal annealing. Different Au loadings were realized by varying either the nominal Au layer thickness (i.e. applied sputter time) or the number of synthesis cycles. The term "cycle" summarizes one sputter-deposition-and-subsequent-thermal-annealing step (figure 4.2). Therefore, a convenient notation for Au nanoparticle classification was chosen as "Au (nominal layer thickness, number of cycles)" and will be used throughout the thesis.

An overview of the preparation protocol is given in table 4.1. The magnetron sputter times are 75 s for Au (1.7 nm, 1), 300 s for Au (6.6 nm, 1), two cycles with 300 s each for Au (6.6 nm, 2) and four cycles with 300 s each for Au (6.6 nm, 4). The samples were annealed at the end of each cycle at  $400^{\circ}\text{C}$  in oxygen as described in section 4.1.2.

### 4.2.2 Bimetallic Au-Ag nanoparticles

Ag-Au nanoparticles with three different elemental ratios, namely (1:5), (3:5) and (9:5), were prepared by deposition of Ag thin film followed by Au deposition and subsequent annealing at  $400^{\circ}\text{C}$  in oxygen (table 4.2). The elemental variation was realized by varying the sputter times: Ag:Au ratios of (1:5), (3:5) and (9:5) were achieved by sputtering 19 s for Ag and 293 s for Au, 36 s

Ag:Au ratio	$d_{Ag}$	$d_{Au}$	$d_{Ag/Au}$
(1:5)	1.3 nm	6.4 nm	7.8 nm
(3:5)	2.5 nm	4 nm	6.7 nm
(9:5)	4 nm	2.2 nm	6.2 nm

**Table 4.2:** AgAu nanoparticle with different elemental ratios were prepared by depositing a Ag layer on tempered DC sputtered TiO<sub>2</sub> followed by Au deposition and subsequent annealing at 400°C for 30 min in oxygen atmosphere.

Au:Ag ratio	$d_{Au}$	$d_{Ag}$	$d_{Au/Ag}$
(5:1)	6.4 nm	1.3 nm	7.8 nm
(5:3)	4 nm	2.5 nm	6.7 nm
(5:9)	2.2 nm	4 nm	6.2 nm

**Table 4.3:** This table presents the sputtering times for AuAg nanoparticles with the same elemental ratios as listed for the AgAu in table 4.2 but with reverse layer sequence. AuAg (5:3) sample was additionally prepared on titania coated TEM grids.

for Ag and 188 s for Au as well as 57 s for Ag and 98 s for Au, respectively. These nanoparticles were deposited on TiO<sub>2</sub> coated FTO glass as well as on 30 nm thick TiO<sub>2</sub> layer on silicon nitride TEM grids from SIMPore (SN100-A50Q33).

Similar samples were prepared by reversing the deposition sequence, hence Au deposition was followed by Ag deposition (table 4.3). The AuAg (5:3) preparation was additionally synthesized on a 30 nm TiO<sub>2</sub> layer on silicon nitride TEM grid.

### 4.2.3 Au nanoparticles on spincoating TiO<sub>2</sub>

Au nanoparticles were deposited on the TiO<sub>2</sub> surface or embedded in the TiO<sub>2</sub> matrix by alternating sputtering and titania coating, leading to Au/TiO<sub>2</sub> composite material. Three different amounts of Au were loaded onto the spincoated TiO<sub>2</sub> surface: Au (1.7 nm, 1) loading (sputter time of 75 s for one cycle), Au (6.6 nm, 1) loading (sputter time of 300 s for one cycle) as well as Au (6.6 nm, 2) sample having a sputter time of 300 s for each of the two cycles. Additionally, a composite Au-TiO<sub>2</sub> was prepared by adding Au (1.7 nm, 1) after every TiO<sub>2</sub> batch, resulting in TiO<sub>2</sub>-Au-TiO<sub>2</sub>-Au-TiO<sub>2</sub>-Au configuration. Here, the last Au (1.7 nm, 1) formed nanoparticles on the surface.

### 4.2.4 Variation in thermal annealing parameter

The influence of the annealing parameter were investigated on as-sputtered Au layers with a nominal layer thickness of 6.6 nm. While the annealing temperature was fixed to 400°C, the annealing time was varied from 30 min to 3 h, the gas flow from pure oxygen (0.050 slm) to pure argon (0.050 slm) flow and the sample was either inserted and extracted to/from the pre-heated furnace or was slowly heated and cooled with a temperature ramp of 2 K/min. This protocol corresponded to Au (6.6 nm, 1). TiO<sub>2</sub>-FTO-glass substrates were used as a substrate as well as 30 nm thick titania coated SiN TEM grids for transmission electron microscopy.

Annealing Time	Gas atmosphere	Temperature ramping
3h	Ar	no
3h	O <sub>2</sub>	no
30min	O <sub>2</sub>	
30min	Ar	no
30min	Ar	2K/min
30min	O <sub>2</sub>	no

**Table 4.4:** *This table summarizes the annealing procedure carried out on as-sputtered Au-TiO<sub>2</sub> with a sputter time of 300 s. The annealing time was varied between 30 min and 3 h, the atmosphere while heating was set as oxygen or argon flow, and either a slow heating ramp of 2 K/min or rapid temperature by insertion of the cool sample into the preheated furnace was applied.*

#### 4.2.5 Au nanoparticles on atmospheric pressure chemical vapor deposition (AP-CVD) TiO<sub>2</sub>

Atmospheric pressure chemical vapor deposition (AP-CVD) TiO<sub>2</sub> was decorated with Au (6.6 nm, 2) (section 4.2.1) as described above.

## 5.1 UV-vis spectroscopy

### 5.1.1 Basic parameters

A beam of electromagnetic radiation with an initial intensity  $I_0$ , that strikes a sample, will get partly reflected ( $I_r$ ), transmitted ( $I_t$ ) and/or absorbed ( $I_a$ ). These intensities normalized to  $I_0$  correspond to the reflectance  $R$ , the transmittance  $T$  and the absorption  $A$  [165][166].

$$R = \frac{I_r}{I_0} \quad T = \frac{I_t}{I_0} \quad A = \frac{I_a}{I_0} \quad (5.1)$$

The sum of these three parameters always adds up to one [166].

The transmittance allows to derive the optical density  $O_D$  [69][165], also termed the absorbance  $A_b$  :

$$A_b = O_D = -\log_{10} T = -\log_{10} \frac{I_t}{I_0}. \quad (5.2)$$

The absorbance is the product of the molar extinction coefficient (in Lcm/mol)  $\epsilon$  [166][167], the analytes concentration  $c$  (in mol/L for solutions) and the layer thickness  $d$  (in cm) according to Bouguer-Lambert-Beer law:

$$A = \epsilon c d. \quad (5.3)$$

### 5.1.2 Set-up of the Lambda850 UV-Vis spectrometer

Transmission and Reflection spectra between 250 nm and 900 nm were obtained by using a Lambda850 UV-Vis double beam spectrometer from PerkinElmer (figure 5.1). It consists of two light sources that are switched automatically during operation at 319.20 nm by a movable mirror. A TrueLife 1.5 deuterium lamp was used for a stable light intensity in the UV region between 250-319 nm, whereas a tungsten lamp was applied for the visible spectra between 319-900 nm. The light passes an optical filter before entering a slit assembly and reaching the monochromator. The monochromator consist of a holographic grating (Littrow configuration with 1440 L/mm), where the incoming light is dispersed and transformed into a spectrum. This grid rotates and selects a small part of the spectrum that passes the exit slit as nearly monochromatic. Low stray light level

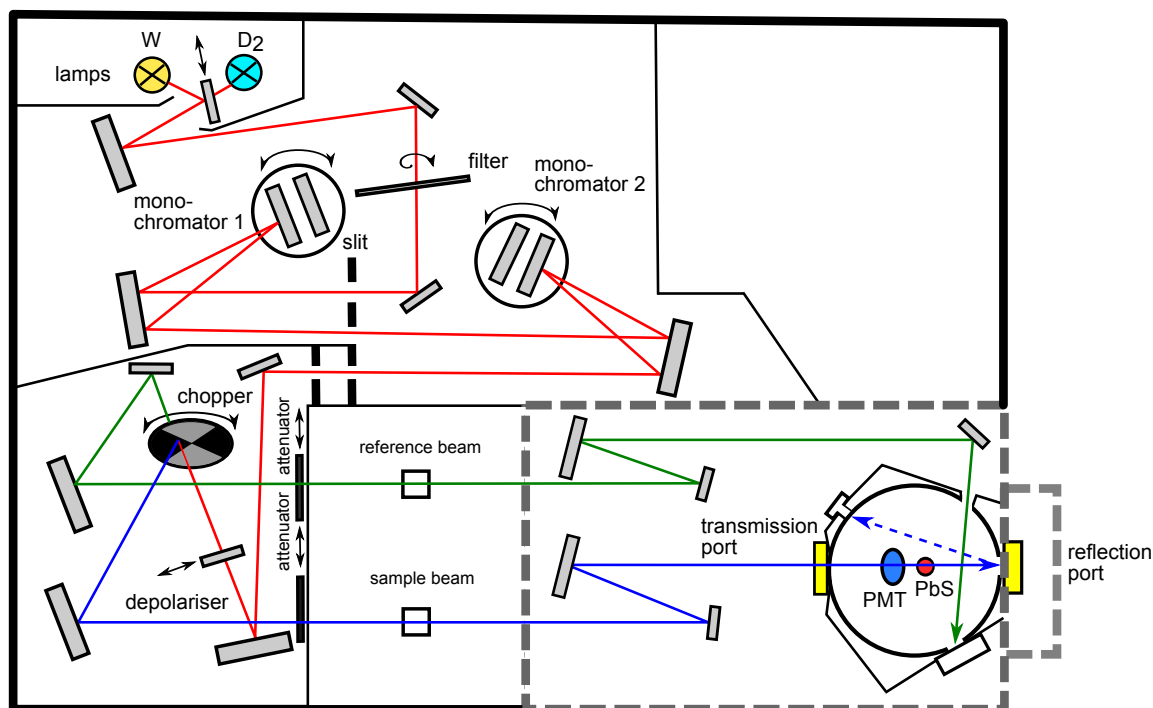


**Figure 5.1:** A double beam UV-vis absorption spectrometer with an integrated sphere was used to collect transmission and reflection spectra in the spectral range between 250-900 nm [168]

is realized by connected the first monochromator in series with a second, synchronized one. After leaving the second monochromator, the light passes a beam mask that is able to reduce its cross section, in case small illumination areas are needed. A chopper divides the incoming light beam into a reference and a sample beam. It contains a mirror segment to guide the sample beam, a window segment for the reference beam as well as two non-transparent segments. Finally, the light is directed to the sample compartment and to the detector.

Diffuse transmission and reflection are measured by using an integrating sphere with a diameter of 150 mm and walls covered by spectralon for high diffuse reflectivity of incident light. The diffuse transmission is determined by placing the sample at the entrance port of the sphere, while the reference beam enters the integrating sphere through a second port. The reflection port is covered with a white standard for the diffuse transmission measurement. The light transmitted through the sample enters the sphere and is homogeneously reflected at the spheres wall until it reaches the detector. The detector consists of one photomultiplier tube measuring from 200 to 860 nm and a Peltier cooled PbS cell for detection of the near-infrared region from 860 to 2500 nm.

The light, that is being reflected non-directional from the samples, is measured by removing the white standard and placing the sample at the reflection port. A protective cap prevents external light invasion. The diffusely reflected light from the sample reaches the above mentioned detectors and can be analyzed.



### 5.1.3 Operation parameter

Prior to every measurement session, a background over the whole wavelength range is measured and its intensity is set to 100% transmission. Every subsequent measurement is normalized to this internal calibration, to account for the present conditions in the sample compartment like air temperature, atmospheric pressure and humidity. To minimize sample alteration or damage, the spectrum is recorded starting from low energy wavelengths. The spectrometer measurements are controlled by the software UV WinLab from PerkinElmer. For transmission measurements, spectra from 250 to 800 nm were recorded, choosing a data interval of 1 nm, a slit width of the monochromator of 2.00 nm and a PMT response of 0.20s. For the determination of diffuse transmission and reflection, the integrating sphere was used and the light intensity was measured between 250 and 900 nm, with a data interval of 2 nm, a slit of 4 nm and a response of 0.4 s. An aperture was inserted in the sample compartment. To minimize light loss, the windows connecting sample and detector compartment were removed.

## 5.2 Scanning electron microscopy (SEM)

### 5.2.1 Acceleration voltage and wavelength of electrons

The technique of scanning electron microscopy (SEM) allows to investigate the morphology of a surface on the nanometer scale by two-dimensional scanning of the sample with an electron beam [169]. This high magnification below the diffraction limit of visible light is possible, because, according to Louise de Broglie, every electron is allocated to a wavelength depending on the particles momentum [170]:

$$\lambda = \frac{h}{p_e} = \frac{h}{mv}. \quad (5.4)$$

The kinetic energy of an electron can be regulated by applying an acceleration voltage [171]:

$$eV = \frac{mv^2}{2}. \quad (5.5)$$

Rearranging this equation for the velocity and substituting it into the de-Broglie equation 5.4 results in the dependency of the electrons wavelength from the applied acceleration voltage:

$$\lambda = \frac{h}{\sqrt{2meV}}. \quad (5.6)$$

### 5.2.2 Interaction of electrons with a specimen

An electron beam interacts with the electrons and nuclei of the specimen and penetrates the upper part of the specimens surface in a teardrop-shaped volume. The penetration depth is higher for material with low atomic number and density and can be further increased by application of a high acceleration voltage. The impact of the electron beam leads to the emission of several types of particles and rays such as secondary and backscattered electrons, Auger electrons, x-rays and cathodoluminescence light. These products originate from different penetration depths and provide specific information [172] [173].

Inelastic scattering of the incident electron beam removes valence electrons from the specimens, that are detected as secondary electrons. The majority of secondary electrons is generated by direct electron beam-sample surface interaction, however, they are also caused by backscattered electrons

formed inside the bulk and migrating to the sample surface, by interactions of backscattered electrons with the interior of the chamber or by interaction with beam electrons and the objective aperture [174]. Secondary electrons have low energies up to 50 eV and can only escape the material when they are generated close to the surface [172]. Hence, they provide information about the surface topology. The amount of secondary electrons collected by the detector depends on the incident beam angle, the presence of surface steps and edges as well as on charging processes on the samples surface [173][169].

Incident electrons can further be elastically scattered at the nuclei of the sample and reach the detector as backscattered electrons. They show a variety of energies: from nearly equal to the incident electron beam energy down to 50 eV, where they start to overlap with the secondary electron energy spectrum [169]. Their high energy provide information about deeper specimen regions than the secondary electrons. A backscattered electron has to change his direction at least by about  $90^\circ$ , to be detected, which is more probable by performing multiple elastic scatter events, hence far away from the surface [174]. Materials with a high atomic number or density increasingly scatter electrons, which makes it possible to distinguish elemental composition [169][172]. They are mostly scattered in high angles [174] so that the direction of specular reflection is the prominent one. Crystal orientation can also lead to a variation in intensity.

Recombination of knocked-out electrons from an orbit close to the nucleus can be accompanied by emission of an x-ray quantum or an Auger electron [174]. Auger electrons have energies comparable to backscattered electrons [169]. Light emission by refilling the knocked-out electron with an electron from the outer sphere is known as cathodoluminescence [170].

### 5.2.3 Set-up of Jeol SEM

The JSM 7500F field emission SEM device from Jeol provides an optical system for the generation and manipulation of an electron beam as well as a specimen chamber that are both kept under vacuum.

The electron beam is produced by a cold (cathode) field-emission gun made from a sharp tungsten tip (the emitter) with a curvature radius in the order of 100 nm [169]. An extraction voltage between the emitter and an extraction electrode is applied to enable tunnelling of the electrons [172][173]. The electron beam passes through a hole in the center of the extraction electrode to reach an accelerating electrode. A high electric potential of up to 30 kV is applied between the gun and the accelerating anode to adjust the beam energy. Part of the accelerated electrons can pass the anode via a hole in its center [169].

A combination of condenser lenses, an objective aperture and a semi-in-lens objective lens adjusts the diameter of the beam to achieve a fine spot size. A coil-shaped electric wire connected to a DC current acts as a magnetic lens to focus the electron beam. Its strength can be adjusted by the applied current. The focus of the beam is manipulated via the objective lens, with an increase in current leading to shift upwards [174], while the diameter of the beam is controlled by the condenser lens. Before the objective aperture, a scanning coil is introduced to realize the scanning of the observation area by electromagnetically deflecting the beam [175]. Finally, the electron beam reaches the specimen that is mounted on a eucentric specimen stage to enable three dimensional degrees of freedom as well as sample tilting and rotation.

Several detectors are applicable such as a secondary electron detector, a backscattered electron detector and a low angle backscattered electron detector. Low energy secondary electrons are detected by a positively charged collector electrode and accelerated towards the scintillation detector (Everhart-Thornley). The electrons hit a scintillator that is kept at high voltage in the order of 10 kV and generate photons that are guided to a photomultiplier tube. Here, the photons

are converted into electrons and are feed through an amplifier to a processing device. The detected event counts of the detectors are translated into grey levels and the magnification is depicted with a size bar [175].

A turbo molecular pump provides high vacuum throughout the optical column and the specimen chamber, to ensure a clean emitter tip and low scattering of the electron beam in the column. The specimen holder is manually moved between a pre-evacuation chamber and the specimen chamber for sample exchange to ensure high vacuum in the latter one. The system is cooled down by liquid nitrogen to obtain the required vacuum. The emitter is flashed every day to ensure a clean emitter surface.

## 5.2.4 Operating conditions

An accelerating voltage of 15 kV was used to achieve high resolution, a probe current of 20  $\mu\text{A}$  was chosen and the SEM and SEI detector selected. The samples were glued on a specimen holder using Ag conducting paste or carbon pads. Finally, the samples were vacuum-cleaned to ensure a dust-free surface. No further sample preparation was necessary.

## 5.3 Transmission electron microscope (TEM)

### 5.3.1 Relativistic correction for electron wavelength

Electrons used in a transmission electron microscope reach velocities that require a relativistic correction for their wavelength calculation:

$$\lambda = \frac{h}{\sqrt{2meV \left(1 + \frac{eV}{2mc^2}\right)}}. \quad (5.7)$$

This equation underlines that an increase in acceleration voltage leads to a decrease in electron wavelength [171].

### 5.3.2 Set-up of TEM

Similar to SEM, an electron beam is generated and manipulated using a magnetic lens system before it interacts with a specimen. The emitted products are analyzed using a detector while a high vacuum is required. Different kind of electron guns can be used e.g. thermionic or field-emission guns. The applied acceleration voltages are in the order of 20-100 kV and can create up to 1 MV in high voltage TEM [174], by far exceeding the 30 kV commonly used in SEM. The electron beam has to pass two or more condenser lenses where the cross section of the beam and its angle is controlled, influencing the brightness of the final image [170]. A condenser aperture is used to limit the amount of scattered electrons reaching the specimen to protect it against beam damage. The sample under observation is placed in a specimen chamber underneath the condenser lens system. It is introduced and regained using a pre-evacuation chamber to maintain a high vacuum in the TEM column during sample exchange. Liquid nitrogen cooling prevents contamination and decreases the chamber pressure. The specimen holder is able to move in three dimensions as well as tilt around one or two axis (although only one tilting axis can be kept eucentric). The specimen itself is placed closely above the objective lens which possesses a very short focus. This lens generates an image in the image plane as well as a diffraction pattern in the back focal plane. An objective aperture sets the resolution as well as the contrast of the image. A set of projector

lenses are used to enhance either the image plane or the back focal plane and project them onto the detector.

### 5.3.3 Dark field, bright field and contrast

The presence of an objective aperture selects the amount of particles that reach the detector, depending on its position and hole diameter. A bright field is established, when the center of the aperture is placed on the optical axis of the incident electron beam. Electrons scattered further away than a determined angle are absorbed. If no sample is present, all electrons would reach the detector and a bright field would be detected. In case of an existing sample an increase in thickness or density leads to an increase in electron scattering, hence less electrons reach the detector and the observation area appears dark. The aperture can also be centered on one of the diffraction reflexes that is scattered at a specific angle. Without any sample, no electron would be detected in this set-up which is therefore referred to as dark field. To obtain a sharp aberration free image, the electron beam is redirected so that the selected area is moved to the optical axis together with the aperture. The dark field therefore shows bright contrast for scattered electrons at the selected angle.

### 5.3.4 Energy dispersive spectrometer (EDS)

The interaction between the electron beam and the sample can lead to x-ray radiation that is categorized into characteristic x-rays and bremsstrahlung. If the incident electron knocks out an electron from an inner orbit, this vacancy can be refilled by an electron from an outer orbit. The energy difference between both states is converted into an emitted x-ray photon and is characteristic for this transition and the element. X-ray analysis mostly use the  $K\alpha$  doublet originating from the transition of an electron from an L orbit to a vacancy in the inner K orbital. However, the required energy to extract an inner electron increases with increasing atomic number, so that heavy elements have to be detected by using weaker x-ray signals from missing electrons in L or M orbitals.

The incoming electron can also convert a part of its energy into x-rays as it is slowed down by the Coulomb force inside the atoms. The resulting bremsstrahlung exhibits a spectrum with a wide energy range up to the energy of the initial electron. No information about the specimen composition is gained. An x-ray spectrum is an overlap between both kinds of x-rays.

### 5.3.5 Operation parameter

An aberration-corrected JEM-ARM200F TEM microscope from JEOL (corrector from CEOS) was performed at 200 kV by Dr. Marga-Martina Pohl at the Leibniz-Institut für Catalysis e.V. in Rostock to determine the shape and crystallinity of Au nanoparticles as well as size and structure of Ag-Au particles. The aberration-corrected scanning transmission electron microscopy (STEM) imaging in high-angle annular dark-field (HAADF) and annular bright-field (ABF) are done with a spot size of approximately 0.13 nm and a convergence angle of 30-36°. The collection semi-angles for HAADF were chosen as 90-170 mrad and for ABF as 11-22 mrad. Chemical analysis was possible with a JED-2300 (JEOL) energy-dispersive X-ray-spectrometer (EDX) attached to the TEM devise.

Furthermore, high resolution imaging of cross section preparation of Au, Ag and Au-Ag nanoparticles on  $\text{TiO}_2$  were performed with a FEI Titan 80-300 TEM by Dr. Alexander Müller from Max-Planck-Institut für Eisenforschung GmbH. A Gatan UltraScan 1000 CCD was used to record bright-field (BF) and high-resolution TEM (HRTEM) images whereas scanning TEM (STEM) used

a Fischione Model 3000 high-angle annular dark-field (HAADF) detector. Energy-dispersive x-ray (EDX) spectra for elemental analysis were collected with a EDAX detector and electron energy loss spectra (EELS) with a Gatan Tridiem image filter.

## 5.4 Profilometer

A Dektak<sup>3</sup> ST surface profiler was used to measure the film thickness and the vertical profile. A diamond stylus with a 2.5  $\mu\text{m}$  radius approaches the surface and scans the sample within a specific distance and with a defined contact force. The displacement of the stylus is detected as a function of its position to generate a digital height profile. Smooth microscope glass slides were used as a substrate and the differences between substrate height and layer height was measured either by definably scratching the layer or by removing a cellulose acetate strip that protected part of the substrate from deposition.

## 5.5 X-ray diffraction

X-ray diffraction allows to determine the crystal structure of materials, such as the interplanar spacing or defects in the lattice. X-rays are chosen because their wavelengths are compatible to the interatomic spacing.

### 5.5.1 Bragg diffraction

Braggs law determines the conditions under which strong diffraction of a wave on parallel crystallographic planes can occur. In the simplest case, two parallel (coherent) incident rays cover an incident and diffracted angle  $\theta_{diff}$  with the crystal plane. The diffraction occurs on two parallel planes having a interplanar distance  $d$ . Comparing the path length of both rays reveals, that the lower ray has to take an extra length of  $2d\sin\theta_{diff}$ . Constructive interference necessary for obtaining maximal signal can only take place, if the difference in path length between both rays is a multiple  $n$  of their wavelength  $\lambda$ :

$$2d\sin\theta_{diff} = n\lambda. \quad (5.8)$$

The distance  $d$  between the crystallographic planes are expressed using the Miller indices ( $h_1, h_2, h_3$ ) and the lattice parameter  $a_0$ :

$$d_{hkl} = \frac{a_0}{\sqrt{(h_1^2 + h_2^2 + h_3^2)}} [176]. \quad (5.9)$$

A combination of both equation allows the correlation between the observed angle-dependent diffraction peaks and the index of their planes:

$$\sin\theta_{diff} = \frac{\lambda n}{2a_0} \sqrt{h_1^2 + h_2^2 + h_3^2}. \quad (5.10)$$

Small crystal domains, such as in amorphous materials or nanoparticles, show a broadening in the diffraction angle distribution [177].

### 5.5.2 Set-up for Bragg-Brentano

Diffraction reflexes occur if the Bragg law is fulfilled. Polycrystalline samples contain plenty of randomly orientated domains so there is a high probability that under irradiation with monochromatic x-rays some crystallographic planes met the Bragg angle and that a diffraction signal is detected. The specimen as well as the detector are rotated to obtain an angle-dependent intensity diffractogram.

X-rays are produced using a vacuum tube containing a filament for thermionic electron emission. A voltage of about -40 kV [176] is applied to accelerate the generated electrons toward a grounded anode that needs to be cooled with water. A copper anode is used and monochromatic x-rays from the  $\text{CuK}\alpha$  line are emitted. All devices are mounted on a goniometer to control the mechanical movement of the sample and the detector relatively to the stationary x-ray tube. In the para-focussed Bragg-Brentano geometry [178], the detector and the x-ray tube are placed on a goniometric circle to ensure equal incident and diffracted angle at the specimen. The x-rays are generated in a tube and collimated horizontally and vertically by two corresponding slits before they reach the sample. Diffraction occurs and those that obey Bragg's law are collimated by two slits before entering the detector through a final slit. The detector used for collecting the x-rays is described in more detail in the EDS section 5.3.4 and scans through an angle of  $2\Theta$  while the sample only moves through  $\Theta$  to maintain the para-focusing geometry [179].

### 5.5.3 Operation parameter

A Bruker D8 Advance with a  $\text{Cu-K}\alpha$  source for grazing incident X-ray diffraction (GIXRD) was used to identify phases and crystallite sizes of the nanoparticles. Each diffractogram was measured in a  $2\Theta_{\text{diff}}$ -range of  $20\text{--}80^\circ$  at an incident angle of  $0.5^\circ$ , a step width of  $0.02^\circ$  and data collection time of 5 s per step.

## 5.6 Photoelectrochemical half-cell

A half-cell for a three-electrode set-up was used to carry out photoelectrochemical measurements alongside with an X-POT, a IM6e potentiostat and three light sources from ZAHNER-Elektrik GmbH & CoKG. The main body of the cell is made of polytetrafluorethylen (PTFE) and has outer dimensions of  $8\text{ cm} \times 6\text{ cm} \times 2.5\text{ cm}$  as shown in the left photograph of Figure 5.1. The inside of the cell can be filled with an electrolyte while an optical window allows light illumination through the solution. On the rear side, the electrolyte chamber is sealed by pressing and screwing the sample against an O-ring. Hence, the sample area in contact with the electrolyte is equal to the illuminated area during the experiments, so that additional dark current contributions are not expected. Furthermore, the sample is pressed against conductive foam for electrical contact because it acts as the working electrode. A platinum ring electrode is inserted as counter electrode and a calomel electrode (saturated KCl) is used as reference electrode. The calomel electrode has a potential of 0.242 V vs the standard hydrogen electrode (SHE) [180]. The working, counter and reference electrode are connected to the potentiostat.

Two LED light sources were used to investigate the photoactivity of the sample under 529 nm (GRL01) and 378 nm (UVS375) light. They are regulated by a photo sensor attached in front of the half-cell. A constant distance between the LEDs and the half-cell window was assured (right image in figure 5.1). The half-cell was protected from external illumination during the measurements.

All photoelectrochemical measurements were performed with a 0.1M  $\text{Na}_2\text{SO}_4$  electrolyte that was bubbled with nitrogen prior to the half-cell filling. At the beginning, a stream of 1.000 slm

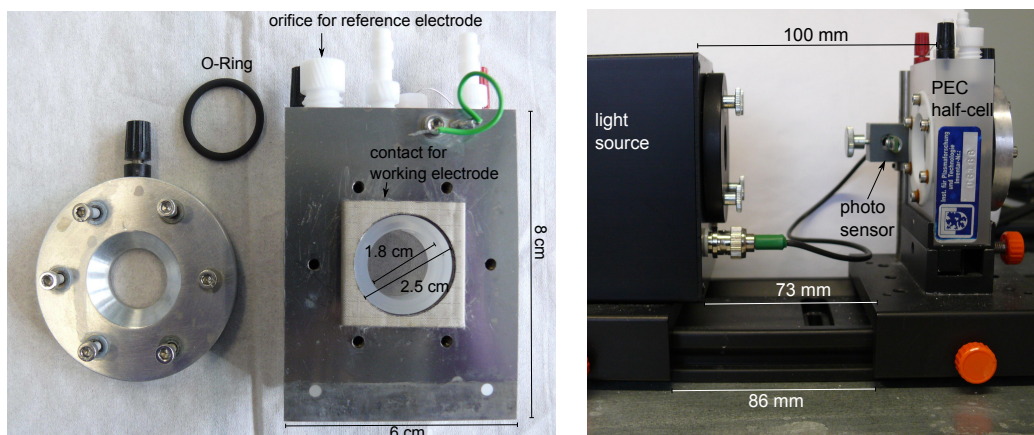


**Table 5.1:** The left photo shows a disassembled photoelectrochemical half-cell. For photocurrent density measurements and cyclic voltammetry, the half-cell was mounted at a fixed position (photo on the right) opposite of the LED.

nitrogen was used to flush the gas line for at least 2 and a half minute before the electrolyte was bubbled with 0.500 slm nitrogen for minimally 20 min. The empty half-cell was rinsed with double-distilled water and dried under nitrogen flow before inserting the sample. A syringe was used to first rinse the half-cell with the electrolyte and to subsequently completely fill it. No nitrogen purging was carried out during the measurement.

Every measurement session started by carrying out a cyclic voltammogram in the dark to condition the sample. Therefore, the potential was swept at a rate of 50 mV/s in three cycles gaining 200 samples per cycle starting from the open-circuit voltage (OCV) to 1.2 V vs NHE, reversed to -500 mV and returned to the OCV. The current range was chosen to be between -1 A in cathodic and 1 A in anodic regime, respectively. Furthermore, current-voltage curves at a slower scan rate of 5 mV/s and a resolution of 5 mV were obtained. In the anodic regime the potential was swept from the OCV to 1.2 V vs NHE before reversing to -200 mV and returning at the OCV. The potential was run from OCV to -500 mV before rising to 500 mV and returning to the starting potential (OCV) to characterize the cathodic behaviour. Again, a current range of -1 A and 1 A was chosen. Finally, the potential of the sample was held constant at 800 mV vs NHE and the photocurrent generated under chopped light was measured. The measurement was carried out for 25 min starting with one minute without illumination followed by six on/off cycles having a two minutes illumination and two minutes dark period. Between measurements, the sample was rested for 10-15 min for returning to the OCV, whereas setting a chosen potential was followed by a 5 min pause to assure sample equilibrium. The sample was exposed to 529 nm light during the 15 min for OCV stabilization prior to CV and I/E curves whereas 5 min equilibrium time was chosen for 378 nm light to reduce changes and possible damage of the sample.

A tunable TLS03 light source (ZAHNER-elektrik GmbH Co. KG) was used for incident photon-to-current efficiency (IPCE) measurements. It consists of 23 discrete LEDs that operated between 365 and 1020 nm in the wideband mode. IPCE measurements were performed by applying a current of 300 mA, a frequency of 10 Hz, an amplitude of 100 mA and a count rate of 100. The end of the glass rod from the TLS03 light source was in direct contact with the half-cell window.

## Results and discussion

### 6.1 Au nanoparticles on TiO<sub>2</sub>

Nanoparticles exhibit unexpected behavior compared to their bulk state (e.g. melting point depression [181]) because of their high surface-to-volume ratio. Different synthesis pathways are known for nanoparticle preparation e.g. chemical [182] or lithography [6]. Nanostructures are further formed by taking advantage of Ostwald ripening or solid state dewetting induced by thermal annealing of magnetron-sputtered thin films [30][32][31]. This physical preparation method results in homogenous deposition of large areas with minimal waste products and is especially interesting for large-scale applications.

There is already fundamental knowledge on annealing of metal layers on substrates like silicon [16][8][17][15], silica [18][17][19][20][21][22][23], polytetrafluoroethylene [11], sapphire [24][25] or single-crystal MgO substrates [26] that exhibit smooth surfaces. Applications such as catalytic water splitting, however, need porous supports with large surface areas. The surface of TiO<sub>2</sub> deposited by direct-current (DC) magnetron sputtering exhibits cauliflower-like columns with diameters of approximately 200 nm (figure 6.1a) that further consisted of domains smaller than 10 nm on the surface (figure 6.1b). This morphology could possibly lead to inhomogeneous nanoparticle growth and a location-dependence of particle properties. This section presents and discusses morphological and related plasmonic properties of Au nanoparticles on TiO<sub>2</sub> with a global cauliflower structure and nanometer surface roughness to test this hypothesis.

#### 6.1.1 Nanoparticle formation: magnetron sputtering-deposition and thermal annealing

Magnetron sputtering was used in this work to deposit nanometer-thin Au and Au-Ag films that are subsequently annealed to form nanoparticulate structures. The reproducibility of this process was checked (appendix section 9.0.7) in order to fulfill the requirement of a potentially large-scale industrial application.

##### Au with nominal layer thickness of 1.7 nm

A Au quantity equivalent to a thin Au film with nominal layer thickness of 1.7 nm was deposited on DC-sputtered TiO<sub>2</sub>. However, the Au did not cover the substrate as a closed film but rather nucleated to isolated particles. Au grows in islands because TiO<sub>2</sub> and Au exhibit dissimilar bond



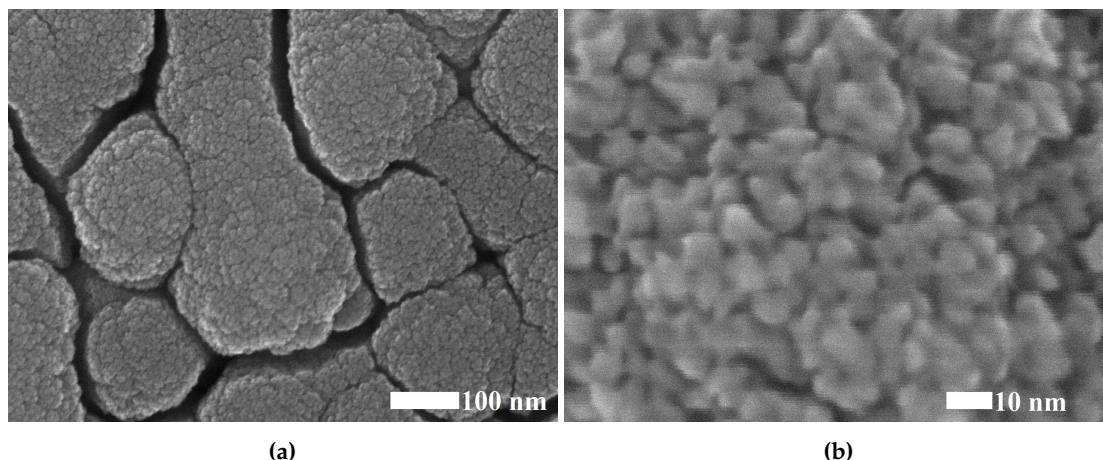


**Figure 6.1:** Top view SEM micrograph of sputtered  $\text{TiO}_2$  showing (a) growth of columns with diameters of approximately 200 nm as well as (b) nanoscale surface roughness with domains smaller than 10 nm.

types so that inter-metal bonds are preferred. These particles have diameters between 3 nm and 13 nm (figure 6.2a and 6.2b) and consisted of spherical islands with diameters below 5 nm and elongated, larger structures that probably formed by coalescence.

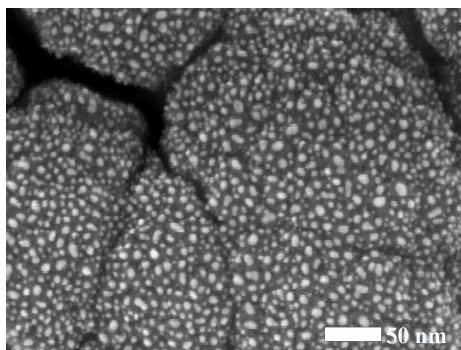
The particle density was high and the distance between the particles low. It is well known that adsorbed atoms have a low mobility [16] and are in a metastable state. The nucleation of adatoms could be kinetically limited because of low temperature during deposition as well as surface diffusion barriers introduced by the nanoscale surface roughness. This "pinning" of nuclei could explain the high island density.

Thermal annealing of these Au nanoparticles at 400°C for 30 min (figure 6.2c and 6.2d) resulted in an increase in particle diameter up to 20 nm. The nuclei migrated across the surface and coalesced with each other that was observed as particle pairs connected with a neck. Their mobility could, however, be hindered by the titania surface roughness, which would limit their growth due to Ostwald ripening. According to this mechanism, that does not require direct contact between the particles, larger nanoparticles grow on the expense of small nuclei. Small nanoparticles exhibit high surface energy per area and expose unsatisfied bonds. Their loosely bonded atoms diffuse on the substrate surface until they coalesce with larger particles. This particle growth is accompanied by an increase in particle distance and a decrease in particle density.

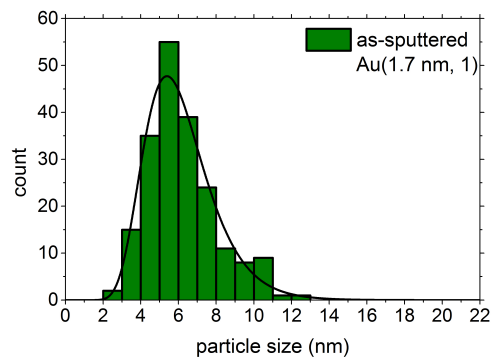
#### **Au with nominal layer thickness of 6.6 nm**

Increasing the Au loading to a nominal layer thickness of 6.6 nm (figure 6.3a) resulted in isolated irregular particles below 50 nm between a partially connected, branched network. This non-continuously connected film is yet below its percolation threshold due to incomplete particle coalescence.

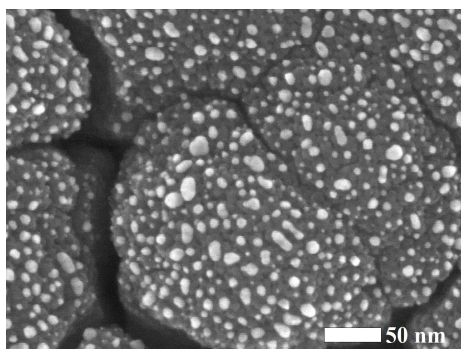
After thermal annealing, this network segregated into isolated spherical-shaped particles exhibiting faceting, a broad size distribution and particles up to 70 nm (figure 6.3b and section 9.0.8 in the appendix). In contrast to the 1.7 nm film described above, the thermal induced diffusion disintegrated the thin film into separated particles as the nanostructure changes its shape in order to minimize surface energy. This process is known as solid state dewetting.



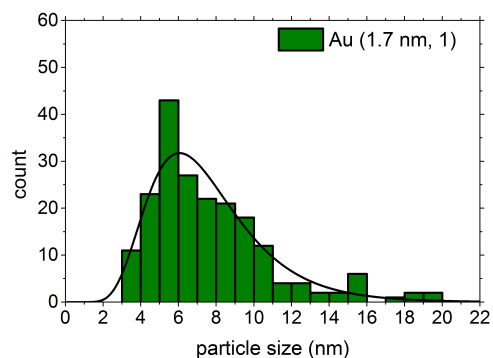
**(a)** As-deposited Au (1.7 nm, 1)



**(b)** Particle diameters between 2-13 nm

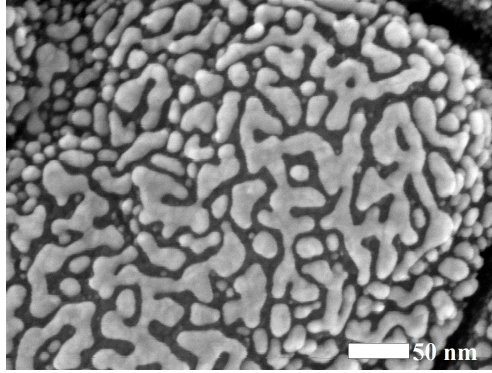


**(c)** After annealing of Au (1.7 nm,1)

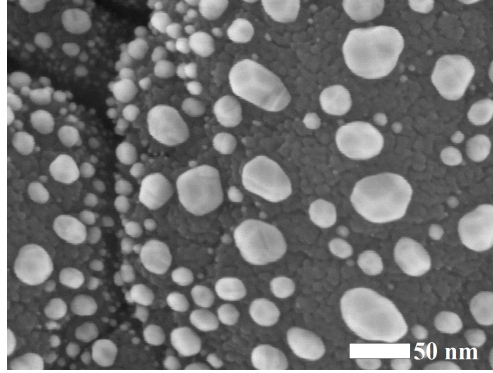


**(d)** Particle sizes up to 20 nm

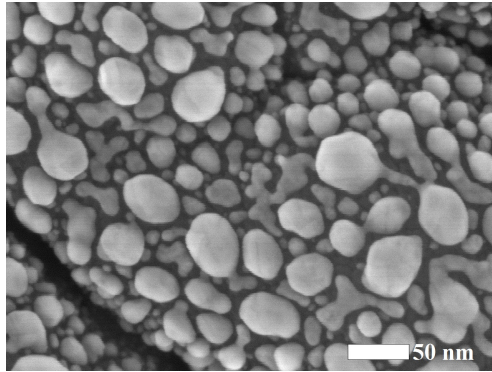
**Figure 6.2:** (a-b) As sputtered Au deposition with 1.7 nm nominal layer thickness formed isolated Au nano-islands with diameters between 2-13 nm. (c-d) Subsequent thermal annealing resulted in particle migration and possibly Ostwald ripening which was observed as a decreased island density and an increase in particle size to 20 nm.



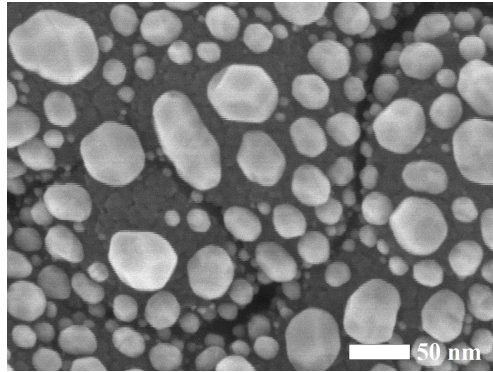
**(a)** *As-deposited Au (6.6nm, 1)*



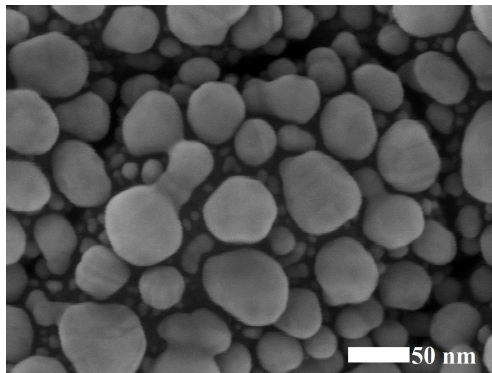
**(b)** *After annealing of Au (6.6 nm, 1)*



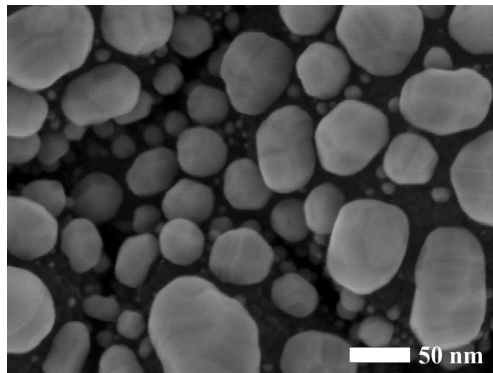
**(c)** *As-deposited Au (6.6nm, 2)*



**(d)** *After annealing of Au (6.6 nm, 2)*



**(e)** *As-deposited Au (6.6 nm, 4)*



**(f)** *After annealing of Au(6.6nm, 4)*

**Figure 6.3:** *Thermal annealing of sputtered Au thin films induced solid state dewetting i.e. the segregation to isolated (and faceted) particles.*



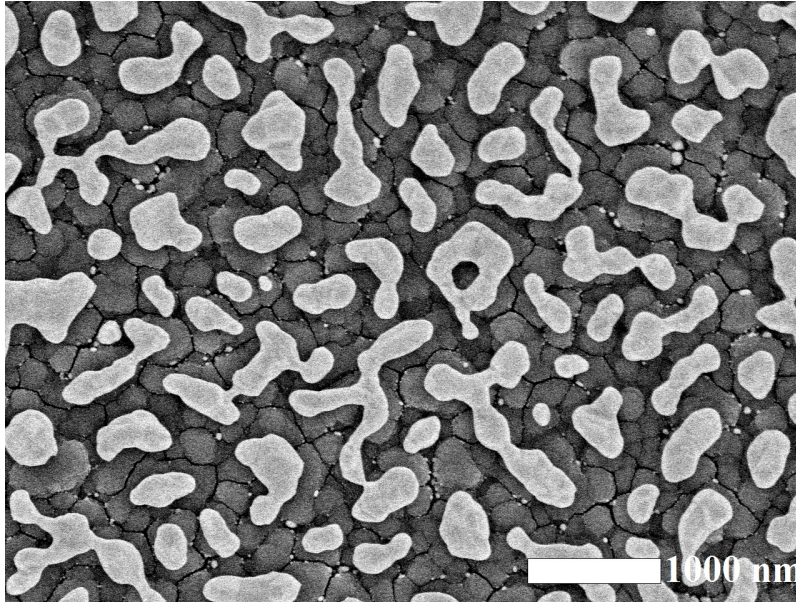


**Figure 6.4:** Thermal annealing of thick initial film layers resulted in worm-like Au nanostructures (100 s at 50 W and 5 Pa argon pressure, subsequent thermal annealing at 400°C for 60 min in oxygen with no iron disc for sputter rate reduction).

Facet formation was observed. Although the scanning electron microscope is not able to determine crystallographic orientation it is known that the fcc lattice structure of Au shows hexagonally closed packing if viewed from the  $\{111\}$  planes. These are the crystallographic planes with the lowest energy and are preferred in facet growth.

### 6.1.2 Cycling for homogenous particle growth

Initially thick Au layers of tens of nanometers can lead to irregular worm-like structures after thermal annealing. Figure 6.4 shows a thermally annealed film with a nominal layer thickness of approximately 50 nm that disintegrated into irregular nanostructures with dimensions in the micrometer scale and inter-particle distances of several hundred nanometers. The initially percolated film probably underwent solid state dewetting by void growth while the elongated structures in the SEM image indicated unfinished Rayleigh instabilities. For plasmonic applications, however, homogenous nanoparticle shapes with high density and small inter-particle distances are favorable [22]. These nano-gaps between the particles, so-called "hot spots", are regions of high electric near-fields and interesting e.g. for sensing applications [183].

To achieve such a homogenous particle growth, the above described deposition-annealing protocol (section 4.2.1) was repeated up to four times. The notation for a prepared nanoparticles system was chosen as Au (nominal layer thickness, number of deposition-annealing cycles). A second deposition of a 6.6 nm Au layer on already dewetted Au(6.6nm, 1) (having an initial layer thickness of 6.6 nm for the first cycle) showed several isolated spherical nanoparticles (some connected by necks) and between them irregular, flattened nanostructures. Additional nuclei absorbed between the particles but most importantly already existing Au nanoparticles grew or coalesced because the presence of pre-existing nanoparticles accelerated the particle coalescence

rather than the formation of new nucleation sites [22]. Again, after thermal annealing, isolated nanoparticles were formed for Au (6.6 nm, 2) (figure 6.3d).

Application of two, three and four cycles – each with 6.6 nm layer thickness – nearly conserved the inter-particle distances with increasing Au loading (figure 6.3d, 6.3e and 6.3f) [22] and increasing particle size distribution. The nanoparticles evolved a bimodal size distribution after performing three cycles, with a majority of nanoparticles having diameters up to 25 nm as well as larger particles with dimensions up to 100 nm (figure 6.5). The diameter of the larger particle increased with the Au loading as is expected from coalescence during deposition and annealing. The presence of small sub-25 nm nanoparticles indicated low surface diffusivity of these nuclei. For them, the observed surface roughness could have imposed high diffusion barriers or the nuclei were trapped at active surface sites because of crystal defects (e.g. oxygen vacancies) or impurities. In any case, the thermal energy or the time was not sufficient to perform Ostwald ripening. Another explanation for a bimodal size distribution could be the titania surface inclination which will be discussed in the next section.

### 6.1.3 Shape and size distribution on TiO<sub>2</sub> surface

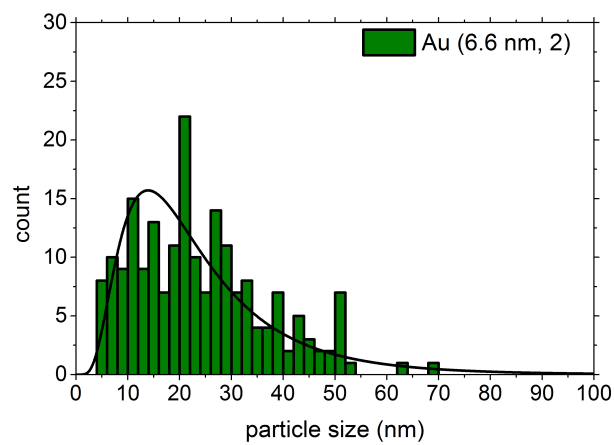
The global topology of DC sputtered TiO<sub>2</sub> is compellingly recognizable by a high resolution transmission electron microscopy cross sectional view (figure 6.6). The metal oxide showed a Z1 growth structure with typical dome-shaped fibrous columns separated by voids. The columnar growth could be further supported by the pyramidal shape of the FTO substrate that dominated the initial growth interface.

Au nanoparticles were clearly distinguished from the titania by their bright contrast (figure 6.6) and their size and shape were determined by their location on the substrate. The TEM image showed Au (6.6 nm, 2) and revealed the oblate shape of particles with diameters of approximately 50 nm that were located on top of the columns. Towards the inter-columnar voids the particle size decreased continuously and the shape became gradually spherical.

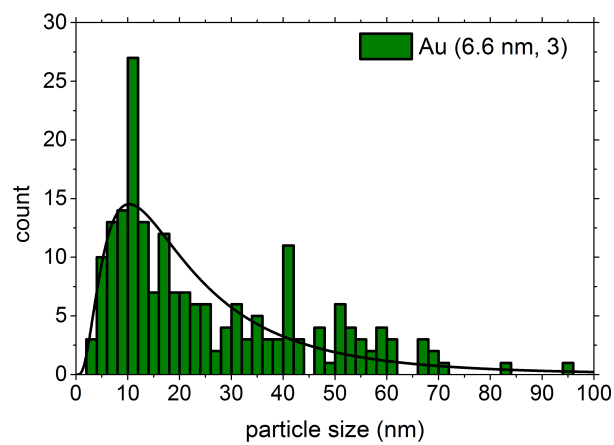
Location dependent particle sizes could be related to the substrate topology that determined the angle of incident deposition at the surface. A maximal nominal layer thickness is deposited on surfaces perpendicular to the incident sputter direction while the thickness decreases with increasing declination angle. The sputtered atoms impact on the titania substrate at an approximately constant angle. Therefore, the tilted column sides should be covered by a thinner nominal layer that led to small sized particles after thermal annealing as discussed in section 6.1.1. Additionally, the columns may shadow part of the voids from deposition. It could further be speculated that surface diffusion along the slopes during annealing is preferred in the direction of fiber growth (in analogy to the surface barrier for diffusing down a step in epitaxy that is known as Ehrlich-Schwoebel barrier).

### 6.1.4 Localized surface plasmons of Au nanoparticles

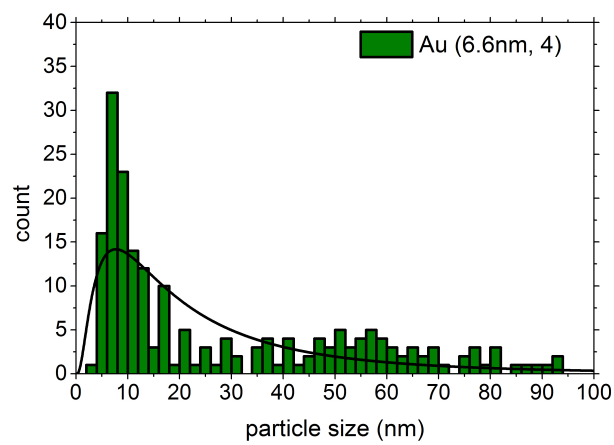
The previous section argued that the total Au amount and the location on the TiO<sub>2</sub> substrate determined the particle shape and size. These particle properties can further be observed using optical spectroscopy. The UV-vis spectra of Au(1.7 nm, 1), Au(6.6 nm, 1), Au(6.6 nm, 2) and Au(6.6 nm, 4) nanoparticles on DC sputtered TiO<sub>2</sub> (figure 6.7) were recorded in diffuse transmission and equation 5.2 was applied to calculate the corresponding absorbance. The absorbance of pure TiO<sub>2</sub> on FTO@glass was added to the figure as reference and dominated the optical properties of the system. The strong absorbance below 380 nm originates from the anatase band gap. For wavelengths larger than 387 nm [184], the excitation is low but does not fall to zero which can be



(a)



(b)



(c)

**Figure 6.5:** Increasing the Au amount results in the evolution of a bimodal size distribution.

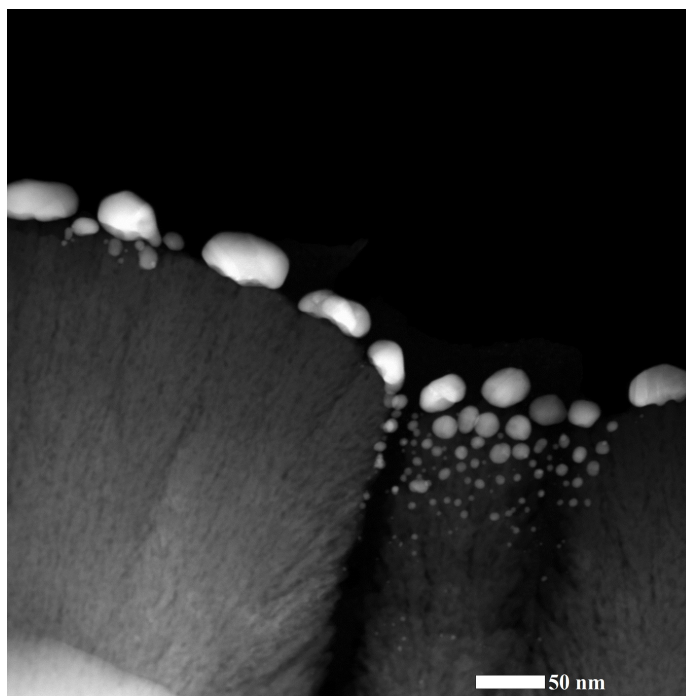


**Figure 6.6:** *This TEM cross section of Au(6.6 nm, 2) nanoparticles on TiO<sub>2</sub> shows the metal nanoparticles, the fibrous titania and the bright FTO substrate in the left corner that can be distinguished by contrast difference. A location dependent size distribution of the metal nanoparticles was observed.*

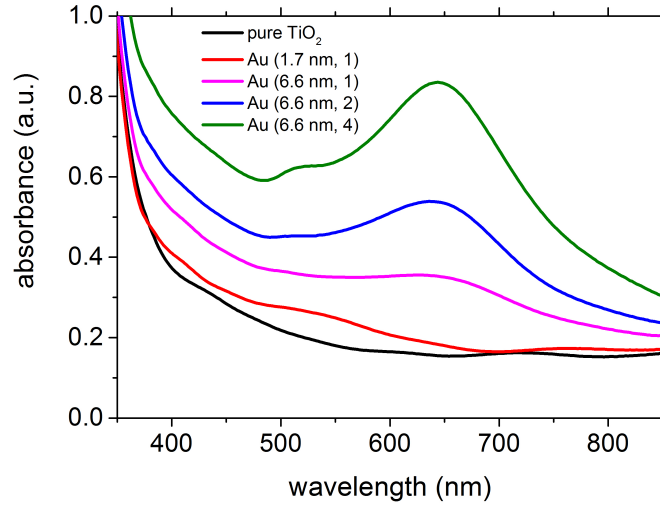


**Figure 6.7:** An increase in Au loading resulted in non-spherical nanoparticles with a longitudinale LSPR between 550-750 nm and the formation of a transverse resonance between 480-530 nm.

ascribed to scattering and/or the formation of bulk and surface vacancies or chemical impurities [110] that act as optical centers [60][185]. These features were observed in all investigated anatase substrates used in this work (see figure 9.9 in the appendix).

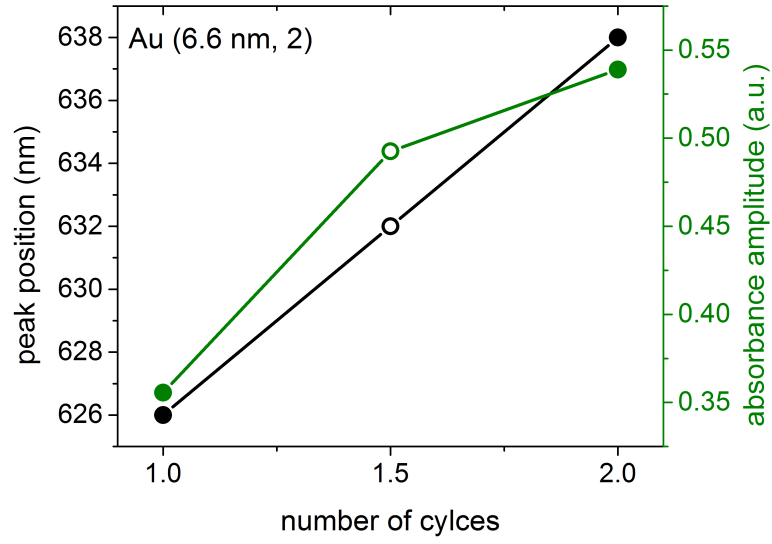
### Longitudinal and transverse excitation mode

Non-spherical nanoparticles such as observed in figure 6.6 section 6.1.3 exhibited two localized surface resonance (LSPR) peaks corresponding to the longitudinal (along the extended axis) and the transverse (excitation along the short axis) mode [186].

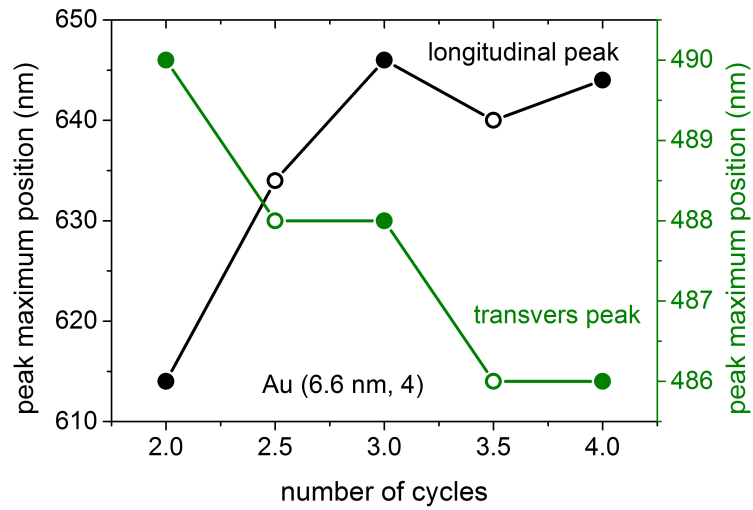
The presence of the longitudinal peak between 550-750 nm is observed for all samples prepared by using 6.6 nm as an initial Au layer thickness. For visualization (figure 6.8a), the absorbance spectra of the two first cycles with 6.6 nm as initial Au layer were smoothed and the null of the first derivative provided the peak maximum position and peak intensity. The resonance intensity increased after Au deposition as is expected from the higher Au amount on the TiO<sub>2</sub> (Lambert-Beer law [187]) and continued to increase with a lower slope after annealing (total intensity enhancement of  $\Delta I = 0.18$  a.u.). The second Au deposition e.i. deposition on already formed particles resulted in a linear red-shift that continued after sample annealing (a shift from 626 nm to 638 nm –  $\Delta\lambda = 12$  nm – was observed during this second cycle). The previous section argued that the particle transformed from small spherical to large oblate particles. This increasing eccentricity of the particle shape might be responsible for the red-shift, as the opposite surface charges are further separated and therefore exhibite a weaker restoring force [188]. Moreover, elongated particles are more sensitive to the refractive index of the surrounding medium i.e. the TiO<sub>2</sub> [186]. The particles morphological changes during particle growth which is reflected in a red-shift of the longitudinal mode.

The shift of the peak position apparently saturated at approximately 645 nm at a repetition of four deposition cycles (figure 6.8b). Notice that the LSPR positions for two full cycles, i.e. Au(6.6 nm, 2) nanoparticles in figure 6.8a and Au(6.6 nm, 4) nanoparticles in figure 6.8b did





(a)



(b)

**Figure 6.8:** (a) The longitudinal peak shifted continuously to longer wavelengths. (b) The dominant peak between 550 nm and 750 nm increased in intensity and shifted to larger wavelengths for the third cycle (approximately 645 nm peak maximum) and then stagnated. A smaller peak evolved between 480 nm and 550 nm, increased in intensity after Au deposition and shifted to smaller wavelengths (blue-shift).

not match because they represent two physically independent samples that showed a stochastic variation for identical preparation parameter. The longitudinal mode shifted approximately 30 nm to larger wavelengths for the third cycle, followed by a blue-shift upon the final deposition and a shift to higher wavelengths (643 nm) for the final annealing. If the initial red-shift is caused by an increase of the particle eccentricity, than this saturation might cause a slower increase in particle radius with increasing volume ( $r \propto \sqrt[3]{V}$ ). The retarded increase in particle radius with repeated cycling could explain the saturation.

The transverse LSPR between 480 and 530 nm is only apparent for the Au (6.6 nm, 4) and (weakly) for the Au (6.6 nm, 2) Au nanoparticles. It did not vary significantly in peak position upon annealing but shifted to shorter wavelengths upon sputter deposition with an overall blue-shift of 4 nm (figure 6.8b). The transverse mode has a lower intensity than the longitudinal mode because its resonance wavelengths lies close to the inter-band transition of Au that introduces a damping of the electron oscillation. The longitudinal peak was less effected by this inter-band transitions because it appeared at higher wavelengths.

This section posed the hypothesis that particle properties such as size and shape depend on the topography of the substrate. This is further supported by the absorbance spectroscopy of a Au/AP-CVD TiO<sub>2</sub> system, where the separation of two peaks is even apparent for Au (6.6 nm, 2) loading (figure 6.9). The first resonance located between 480 nm and 550 nm corresponds to the transverse LSPR while the absorbance peak between 550-680 nm indicated longitudinal excitation. The peak separation was not as strong as for the equivalently prepared particles on DC sputtered TiO<sub>2</sub>. This suggests that a majority of the Au nanoparticles deviate from the spherical shape to allow two electron oscillation directions with different restoring forces. However, compared to Au (6.6 nm, 2) on DC TiO<sub>2</sub>, the particles shape is expected to be less eccentric than the Au-DC-TiO<sub>2</sub> system as the peaks are not as separated. The SEM images of AP-CVD suggest that the porous titania morphology prevents the formation of prolate particles as were found on top of sputtered TiO<sub>2</sub> (figure 6.25 in the appendix). This higher degree of sphericity could be responsible for the closer peak positions.

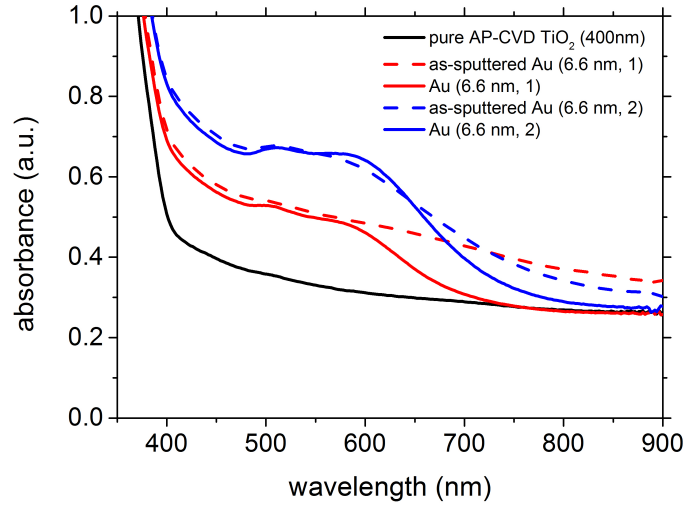
### 6.1.5 Summary: Au nanoparticles on TiO<sub>2</sub>

Au nanoparticles were prepared by combining a thin-film deposition technique by magnetron sputtering with subsequent thermal annealing. The TiO<sub>2</sub> substrate strongly determines the particle growth because of the global cauliflower structure as well as surface nano-roughness. Variation in initial Au layer thickness, shadowing effects and surface diffusion barriers results in large, oblate Au particle centered on top of the titania columns. The Au nanoparticles become smaller and more spherical closer to the columns edge. This deviation in particle size and shape became dominant for larger Au amounts and is reflected in a separation of longitudinal and transverse optical excitation modes.

Cauliflower-like structures are typical for sputter deposition processes and the phenomenon of increased nanoparticles size and shape distribution for high Au amounts has to be considered. Excitation of transverse and longitudinal LSPR of the oblate shaped particles can be advantageous if an extended part of the visible spectrum needs to be absorbed.

## 6.2 Variation of thermal treatment

It is important for large-scale applications of a nanoparticle preparation method whether small fluctuations in the initial parameters lead to significant deviations in the nanoparticle properties; in other words if the chosen method is robust. In the literature, thermal annealing of metal layers

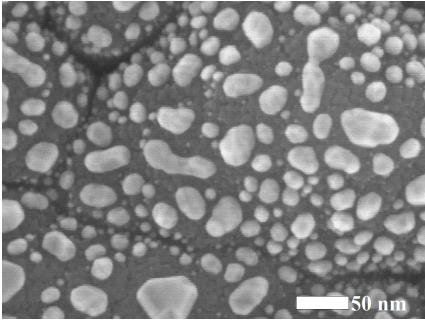
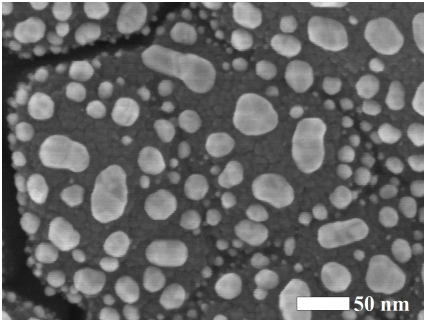
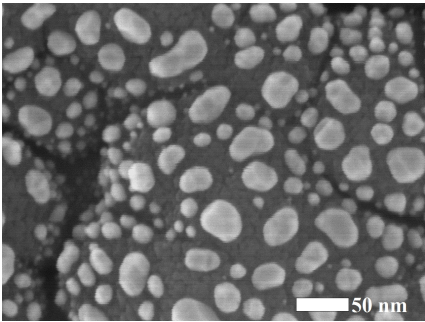
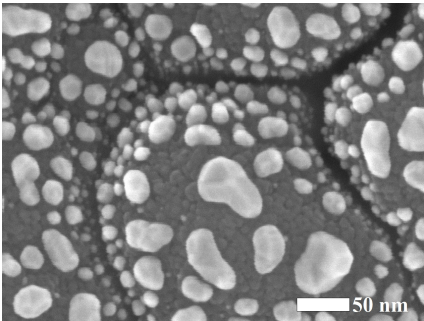
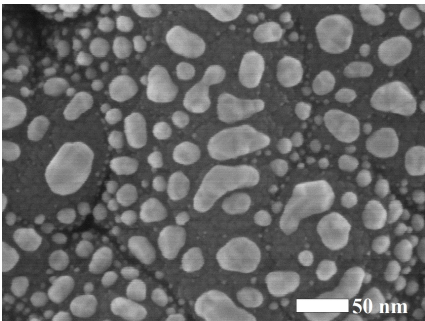
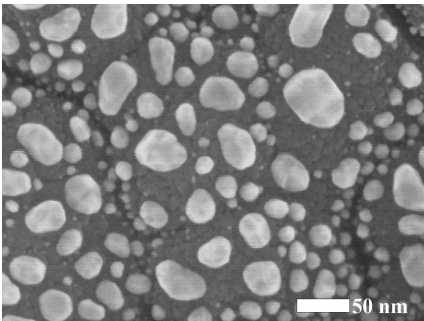


**Figure 6.9:** The evolution of two absorbance peaks was also observed at Au (6.6 nm, 2) nanoparticles on 400 nm AP-CVD TiO<sub>2</sub>. The longitudinal and transverse peaks were closer together and the longitudinal exhibited a lower intensity than the Au (6.6 nm, 2) nanoparticles on DC sputtered TiO<sub>2</sub>.

was mainly investigated under variation of the applied temperature [16][27][28][21][29][30][31][32], layer thickness [33][18][21][29][30] or substrate crystallographic orientation [26]. In this experimental series, a thin film of 6.6 nm nominal thickness was deposited and subsequently annealed at 400°C. Although an increase in temperature should enhance the surface diffusion lengths [189] and therefore significantly affect particle formation the temperature was kept at 400°C to inhibit diffusion of Sn atoms from the FTO substrate to the titanium dioxide [190]. Three parameters were varied namely the annealing time (30 min and 3 h), the temperature ramp (2 K/min or none) and the composition of the gas atmosphere (oxygen and argon). No temperature ramping refers to the immediate introduction and retrieval of the sample from the preheated furnace which will also be termed "rapid heating" (RH). The influence of this parameter variation was investigated by observing nanoparticles morphology, plasmon resonance frequency, crystallinity and photocurrent generation.

### 6.2.1 Scanning electron microscopy

Isolated nanoparticles (figure 6.1) formed with an expected stochastic and location depending size and shape distribution for all preparation conditions. Likewise, elongated nanostructures from incomplete particle coalescence were found in every case, however, mainly at argon 3 h, oxygen 30 min rapid heating (RH) and argon 30 min, 2 K/min. Au does not react with oxygen so it can dewet under oxygen-containing atmosphere [191]. There is controversy in the literature if oxygen reduces the mobility of Au atoms and hinders coalescence [192] or if it enhances surface diffusion and accelerates dewetting process [110]. Although oxygen-induced incomplete coalescence of Au atoms could be responsible for a preferred formation of elongated nanostructures, the differences between sample sets are marginal suggesting weak influence of the gas atmosphere.

	argon	oxygen
3 h (RH)		
30 min (RH)		
30 min (2K/min)		

**Table 6.1:** SEM images of Au layers with a nominal thickness of  $6.6 \text{ nm} \pm 0.7 \text{ nm}$  that were annealed at  $400^\circ\text{C}$  under different conditions. The conditions were varied with respect to the treatment time (30 min or 3 h), the application of a temperature ramp (2 K/min or rapid heating, RH) and the ambient gas flow (pure oxygen or argon, respectively).

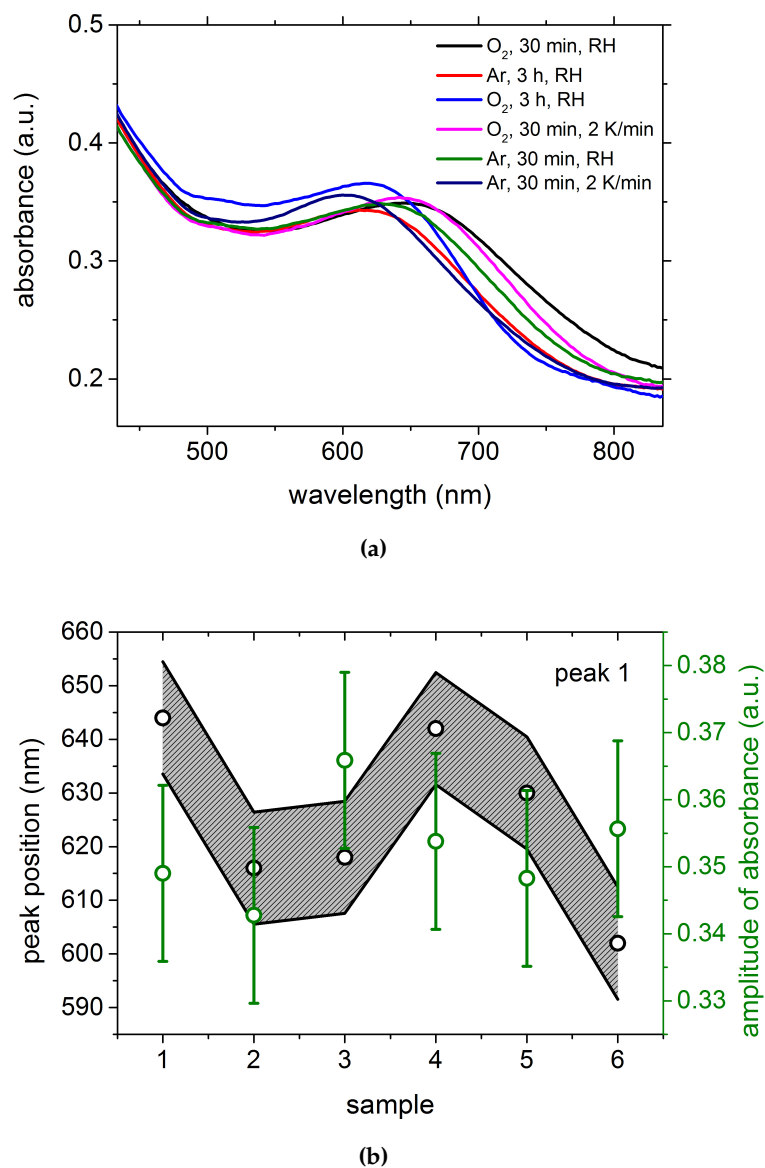


**Figure 6.10:** (a) Thermal annealing while varying the gas atmosphere, time and temperature ramping resulted in deviating LSPR peak maxima. (b) The LSPR peaks are plotted with the estimated standard deviation of peak maxima as error bars. The legend is as followed: (1) oxygen, 30 min, RH, (2) argon, 3 h, RH, (3) oxygen, 3 h, RH, (4) oxygen, 30 min, 2 K/min, (5) argon, 30 min, RH, (6) argon, 30 min, 2 K/min.

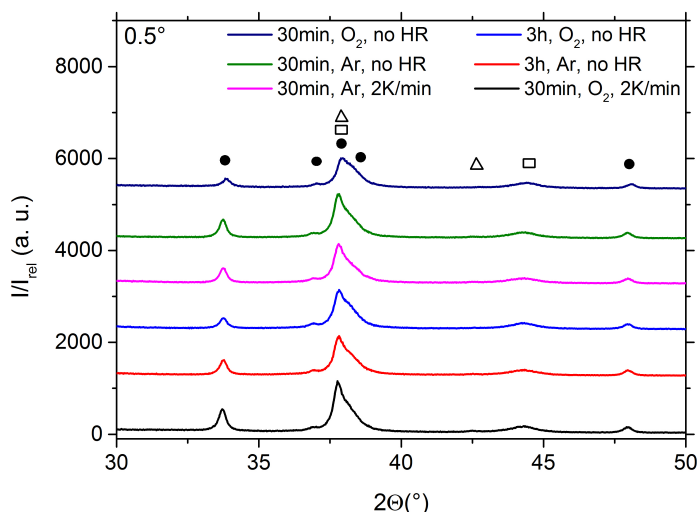


**Figure 6.11:** XRD spectra for thin Au layers annealed under different conditions. Symbols: open square: Au, closed circle: TiO<sub>2</sub>, open triangle: FTO.

## 6.2.2 UV-vis spectroscopy

UV-vis spectra showed LSPR maxima between 602-644 nm (figure 6.10a). These maxima were calculated by determining the spectra's extrema (figure 6.10b) with the standard deviation (figure 9.0.9 in the appendix) as error bars. The standard deviation was needed to distinguish between fluctuations in LSPR position due to the stochastic nature [193] of solid state dewetting and significant effects from the variation of the parameters.

The absorbance spectra showed an extremum at approximately 540 nm possibly related to transverse excitation. Its LSPR positions did not show significant shifts within the experimental insecurities (figure 9.4 in the appendix).

For the longitudinal mode, argon resulted in LSPR with the lowest wavelengths (3 h, RH and 30 min, 2 K/min) whereas the strongest shift to high wavelengths was found for oxygen treated samples (30 min, RH and 30 min, 2 K/min). Rapid annealing under oxygen for 30 min formed elongated nanoparticles that could explain the red-shift.

## 6.2.3 X-ray diffraction

X-ray diffraction of these samples (figure 6.11) showed the crystalline phases of TiO<sub>2</sub> anatase (space group I4<sub>1</sub>/amd), Au (space group Fm $\bar{3}$ m) and SnO<sub>2</sub>(space group P4<sub>2</sub>/mmn). A modulation in the background between 30-36° 2 $\Theta_{diff}$  was observed for the sample annealed under oxygen for 30 min with a 2 K/min heating ramp (appendix figure 9.6).

The average size of the Au crystals were calculated (table 6.2) using Debye-Scherrer formalism from the peak area of the (200) Au reflection and varied between 9 and 11 nm. There is no conclusive trend, regarding the time or the gas atmosphere on the crystal size.

Sample Description	Crystallite Size D after Debye-Scherrer / nm
3h, Ar, RH	10
3h, O <sub>2</sub> , RH	11
30 min, O <sub>2</sub> , 2K/min	11
30 min, Ar, RH	10
30 min, Ar, 2K/min	9
30 min, O <sub>2</sub> , RH	9

**Table 6.2:** Crystallite size were calculated from the peak area of the (200) Au reflection at  $44.41^\circ \pm 2^\circ \Theta_{diff}$ .

#### 6.2.4 Transmission electron microscopy

Mono- and polycrystallinity of single Au particles were evaluated by transmission electron microscopy. To enable TEM, a 30 nm thick TiO<sub>2</sub> layer was deposited by reactive DC magnetron sputtering onto SiN grids and used as nanoparticles support. Au nanoparticles were synthesized as described above.

All samples showed single crystallinity for small particles and polycrystallinity in large, irregular structures (table 6.4 and 6.3). Besides this general observation, they had tendencies for single crystal formation (3 h argon without ramp; 3 h oxygen without ramp, 30 min argon without ramp, 30 min argon with 2 K/min) or polycrystallinity (30 min oxygen 2 K/min, 30 min oxygen without ramp).

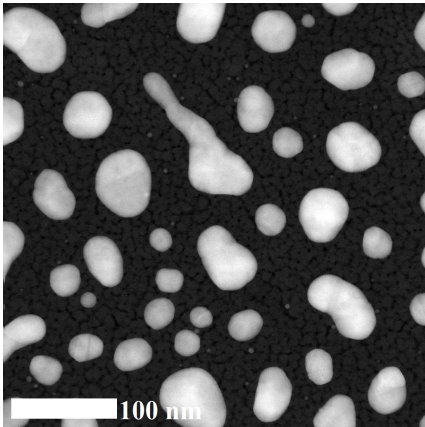
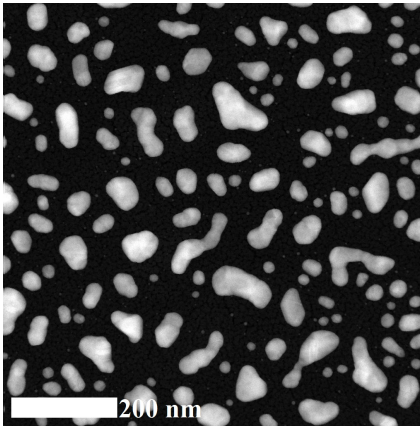
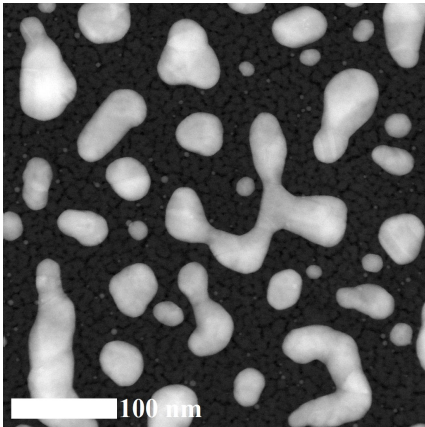
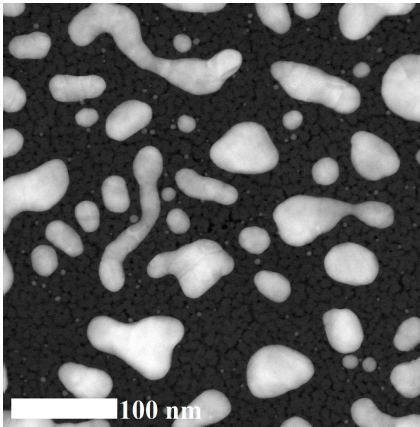
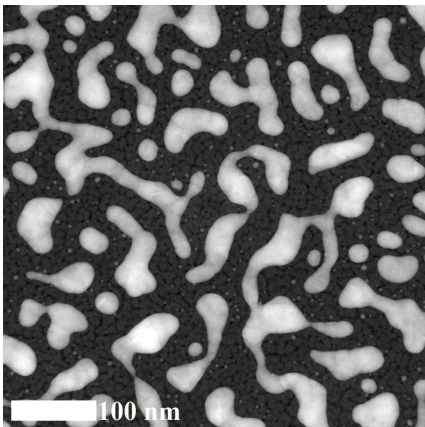
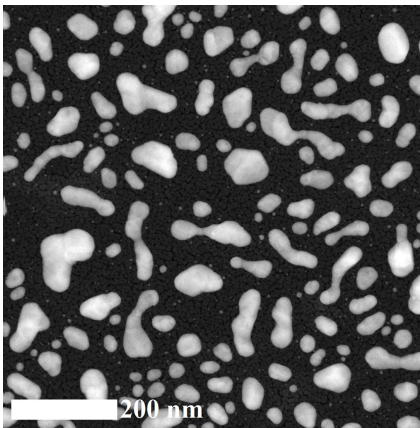
There is a tendency for circular-like particles for 3 h argon treatment whereas more irregular particles were observed for 30 min under oxygen with 2 K/min ramp, 30 min argon without ramp, 3 h under oxygen and 30 min oxygen without a ramp. For data interpretation consider that 30 min annealing plus slow heating and cooling ramps summed up to an extended period of temperature exposure for the sample. A high amount of elongated and irregular particles were found for the parameters 30 min in argon and a 2 K/min ramp. Moreover, grain boundaries, particle agglomeration and five-fold twinning were found (figure 6.12).

No conclusive trends were observed for the variation in annealing treatment and the samples showed only small deviation. Studys conducted by Karakouz et al. showed no difference in particle embedding with the glass substrate of oxygen presence or absence in the thermal annealing of just-percolated Au films [194]. Bechelany et al. found that annealing in nitrogen does not show differences in the orientation of Au nanodots compared to oxygen-containing ambient air [195]. The small differences in the morphology and structure of the nanoparticles indicated a robust and therefore reproducible annealing process.

#### 6.2.5 Summary: variation of thermal treatment

Variation of time, gas atmosphere and temperature ramp in the annealing step was investigated by comparing shape, optical absorbance and crystallinity of the Au nanoparticles. The sample prepared using oxygen atmosphere for 30 min rapid heating contained elongated nanoparticles, possibly due to a reduced mobility of the Au atoms, that exhibited a red-shift of the longitudinal LSPR. However, the influence of the parameters on the particles properties were weak compared to stochastic effects intrinsic to the self-assembling solid state dewetting process. This shows that



	argon	oxygen
3 h (RH)		
30 min (RH)		
30 min (2K/min)		

**Table 6.3:** Tabular overview of TEM micrographs for Au nanoparticles on 30 nm TiO<sub>2</sub> deposited on SiN grids. The annealing parameters were varied according to previous preparation protocols (Figure 6.1). The heating ramp was chosen as an increase/decrease of the furnace temperature by 2K/min or as "rapid heating" (RH) where the sample was introduced/received from the furnace immediately. Please consider the different scale bars.



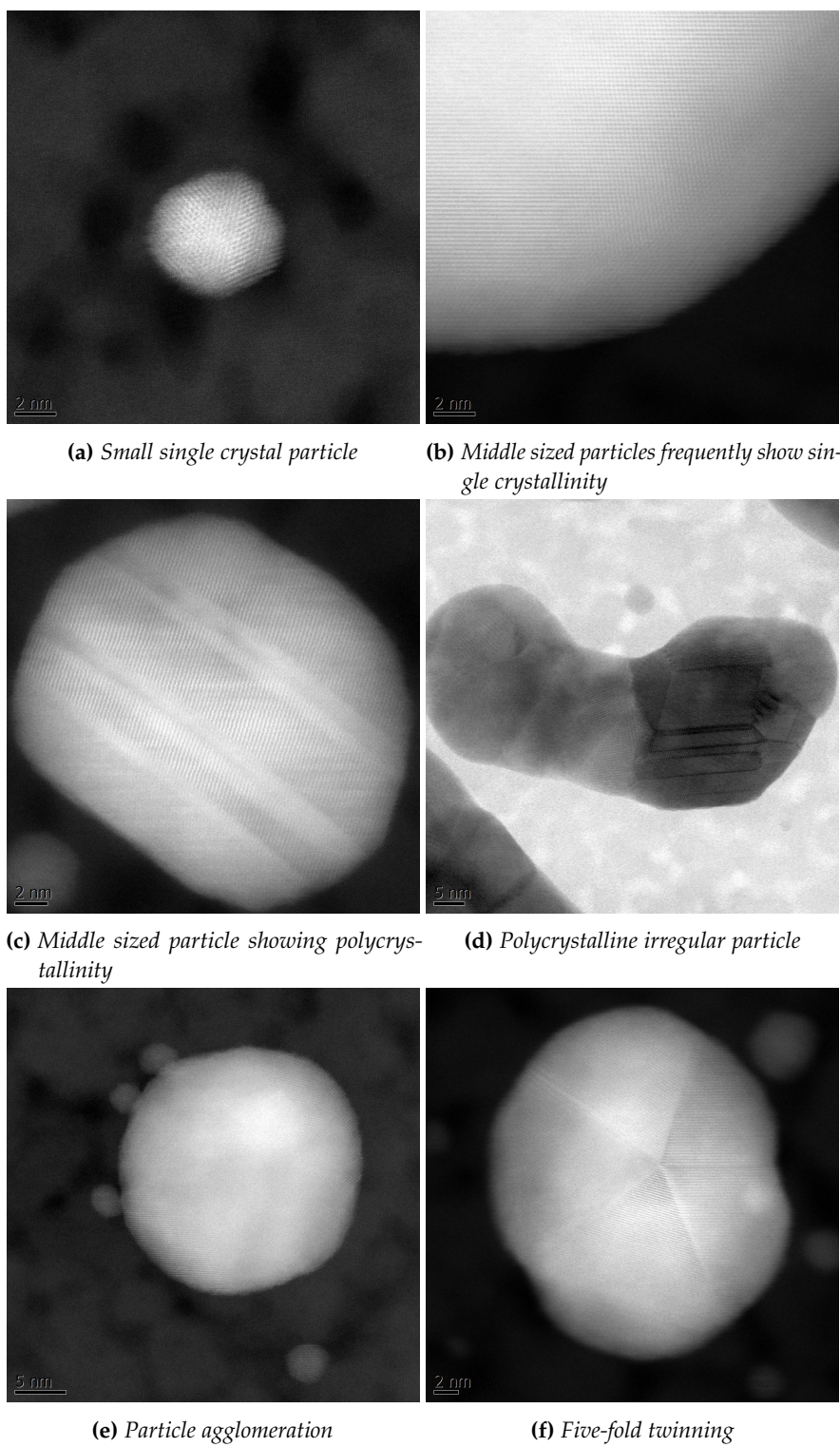


**Figure 6.12:** TEM images of single crystals and polycrystalline particle, particle agglomeration and five-fold twinning.

Parameter	NP<6 nm	20-40 nm NP	NP>70 nm
3 h Ar (no HR)	-	single	poly
3 h O <sub>2</sub> (no HR)	single	single	poly
30 min Ar (no HR)	-	single	poly
30 min O <sub>2</sub> (no HR)	-	poly	poly
30 min Ar (2 K/min)	single	single	poly
30 min O <sub>2</sub> (2 K/min)	single	poly	poly

**Table 6.4:** The crystallinity of the particles were rated by means of TEM images.

the preparation method of thermally annealing magnetron sputtered thin films is a robust process. Such robustness is an advantage for nanoparticle preparation in large-scale applications.

### 6.3 Bimetallic Au-Ag nanoparticles

Bimetallic nanoparticles have raised strong interest due to the tunability of their visible light absorption [196], their refractive index sensitivity [197] and their catalytic activity [198]. They have a large application range as substrates for surface-enhanced Raman spectroscopy (SERS) [34][54][130][131], biosensors [199], catalysts (e.g. reduction of nitrophenols [128][116]) or as potential tags for security applications [200]. They can appear as alloys, in a raspberry structure or core-shell structure [201][54]. Au-Ag core-shell structures are prepared chemically by reduction of the shell element on a colloidal seed solution of the core metal [202][135][127][34][137], by electro-deposition of the shell material [126] or UV-photoactivation techniques [203]. This thesis demonstrates the preparation of reproducible Au-Ag core shell structures by a combination of magnetron sputtering and annealing.

#### 6.3.1 Preparation of Au-Ag bimetallic nanoparticles

The introduction of a second metal for the preparation of bimetallic nanoparticles allowed additional control over the elemental ratio and the deposition order.

In a first experiment, an ultra-thin Ag film was sputtered on TiO<sub>2</sub> followed by a Au deposition. The elemental ratio was chosen to be AgAu (1:5), (3:5) and (9:5) with total nominal thicknesses of 7.8 nm, 6.7 nm and 6.2 nm, respectively. Both metals could not be distinguished by SEM technique. The layer with the lowest Ag amount (AgAu(1:5)) was percolated, i.e. it showed connected clusters in the order of 10-20 nm (figure 6.13a). Conversely, the AgAu (3:5) layer covered the TiO<sub>2</sub> completely and appeared highly faceted (figure 6.13c) with large grains having a size of 20 nm and smaller particles with diameters of about 5 nm. The final sample with the highest AgAu ratio (9:5) was pre-percolated.

A similar sample set was prepared by keeping the AgAu ratio but reversing the deposition sequence. All as-sputtered layers were percolated. With increasing Ag amount the surface coverage increased, cluster size reduced and the particles became more homogenous. The voids in the thin films similarly decreased from long elongated cracks in AuAg (5:1) to shorter voids in AuAg (5:3) and finally to small circular ones in AuAg(5:9).

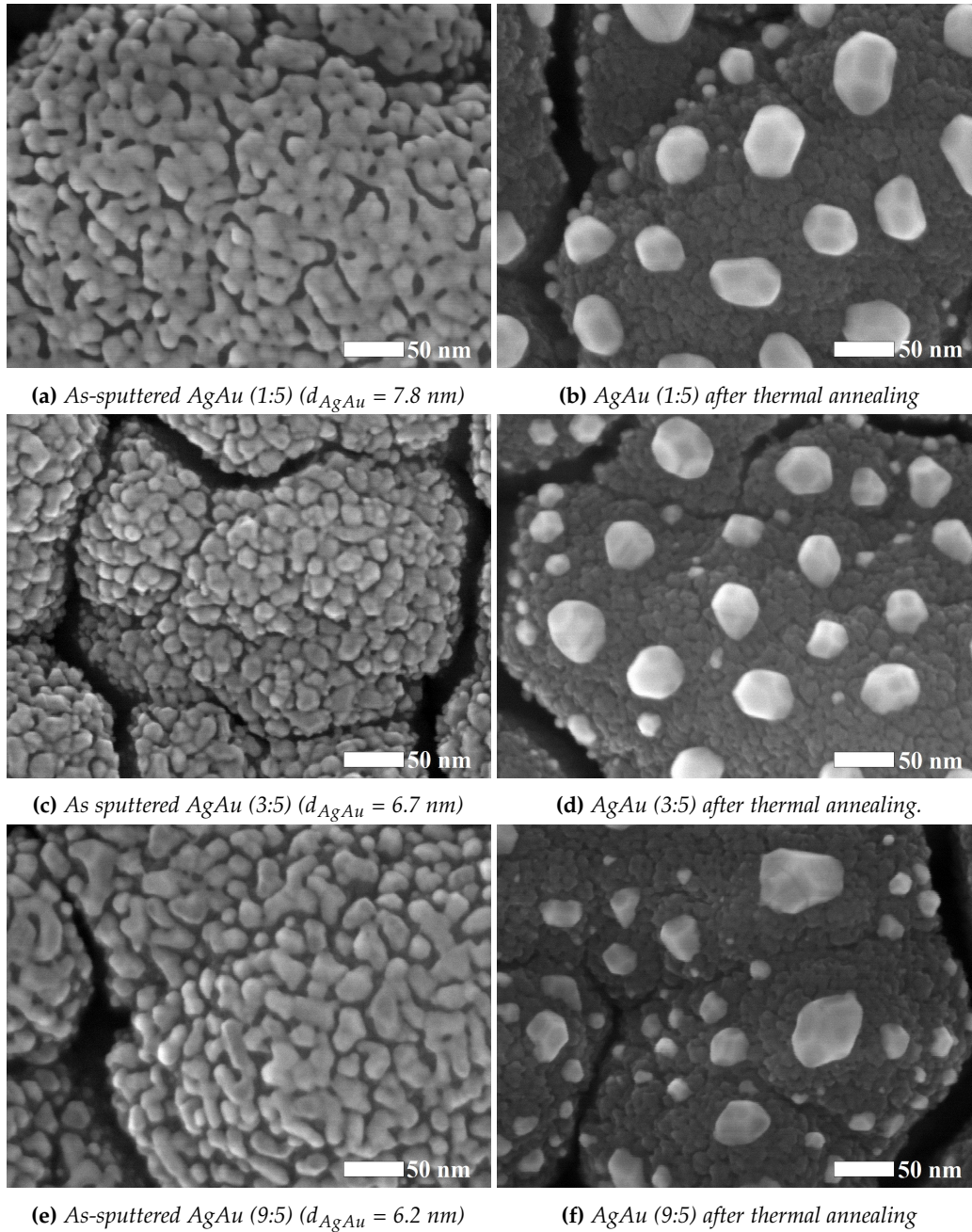


**Figure 6.13:** SEM images of three AgAu nanoparticles with the ratios (1:5), (3:5) and (9:5), respectively, are shown as-sputtered as well as after thermal annealing. The nominal sample thicknesses were chosen to be (a) 1.3 nm Ag (sputter time: 19 s) followed by 6.4 nm Au (sputter time: 293s); (c) 2.5nm Ag (sputter time: 36s) followed by 4 nm (sputter time: 188s) Au deposition and (e) 4 nm Ag layer (sputter time: 57s) prior to a 2.2 nm Au layer (sputter time: 98s).

Film formation depended on the deposition order. As a secondary layer, Ag did not seem to prefer coalescence on either  $\text{TiO}_2$  or the preexisting Au nanolayers that led to the uniform coverage. Au, on the other hand, seemed to stick preferably to the first-deposited Ag nanoislands than to the titania. This could originate in the similarities between the metals [147] and explain the island-dominated film morphology. Therefore, the obtained results hint to a stronger wetting of titania by Ag compared to Au. Regarding the surface energy balance, the sum of the surface energy density of the Ag/ $\text{TiO}_2$  interface and the Ag film surface is expected to be smaller than the Au equivalents.

Isolated nanoparticles were formed after thermal annealing of the bimetallic films that are highly faceted and possessed a broad size distribution. A comparison indicated that nanoparticles formed from the highest Ag amount appeared to wet the titania surface more efficiently than the other samples leading to more irregular nanoparticles. These particles could be described by the Winterbottom construction that accounts for the affinity of the material with the substrate and models particles with cut-off bottom parts [204]. A TEM cross section confirmed the dome-shaped particle morphology (figure 6.15). Ag nanoparticles appeared more faceted compared to the cross section of Au particles.

### 6.3.2 Core-shell structure

The bimetallic Au-Ag nanoparticles showed a Au-core Ag-shell structure. TEM imaging of a AuAg sample showed large nanoparticles of approximately 40 nm. These are accompanied by small particles that grow up to 10 nm with increasing Ag content. High-resolution images of the large 40 nm nanoparticles revealed a core-shell structure visible due to contrast differences indicating the formation of a 1-2 nm thick shell (grey) around a core (white). Even multiple cores surrounded by a single shell are observed. This is not a trivial finding because both metals exhibit face-centered-cubic (fcc) crystal structures and similar lattice constants (0.408 nm for Au and 0.409 nm for Ag being a smaller difference than the amplitude of thermal atomic vibration) [145][146]. Moreover, they exhibit the same atomic radius of 134 pm and similar valence and electronegativity [205] which makes alloy formation possible according to Hume-Rothery rules. Similar preparation techniques described in the literature commonly result in Au-Ag alloys [20]. Core-shell structures are mainly prepared by chemical reduction e.g. the preparation of Au seed by reduction of  $\text{HAuCl}_4$  with ascorbic acid followed by a reduction of  $\text{AgNO}_3$  as was done by Lu et al. [134]. However, Ag shows lower surface energy densities for the 111, 100 and 101 orientation than Au [205]. The Ag atoms exhibit a higher mobility than Au atoms and will preferentially occupy the surface [206], leading to the observed core-shell structure.

EDX analysis revealed that the small particles consist almost entirely of Ag and that the larger particles possess a Au-core and a Ag shell. Surprisingly, EDX on the reverse deposition order (Au deposition followed by Ag thin film) again shows a Au-Ag core-shell structure. This underlines the robust preparation process for Ag-coated Au particles.

### 6.3.3 Plasmon excitation in core-shell particles

Unexpectedly, the core-shell nanostructures showed only one absorbance peak that was sensitive to the Au amount. The as-sputtered layers with the highest Au amount (AuAg (5:1) and AgAu (1:5), respectively) showed a nearly uniform absorption where the AuAg deposition order exhibited the highest absorbance (figure 6.20). After thermal annealing, a LSPR peak was detected between 550 and 750 nm. This LSPR peak decreased with decreasing Au amount and was not observed for the sample with the highest Ag ratio. The AuAg deposition order peak was red-shifted and slightly



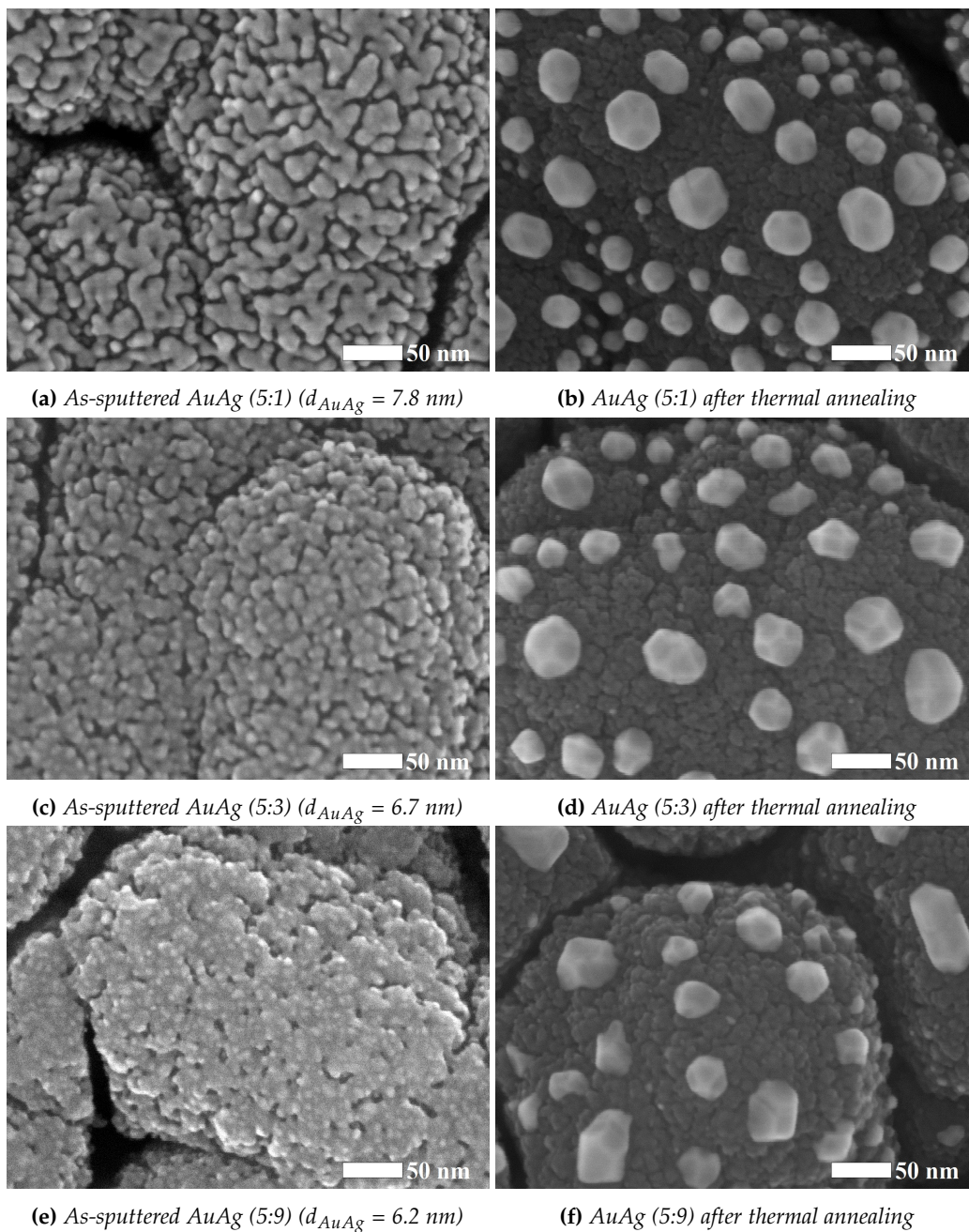
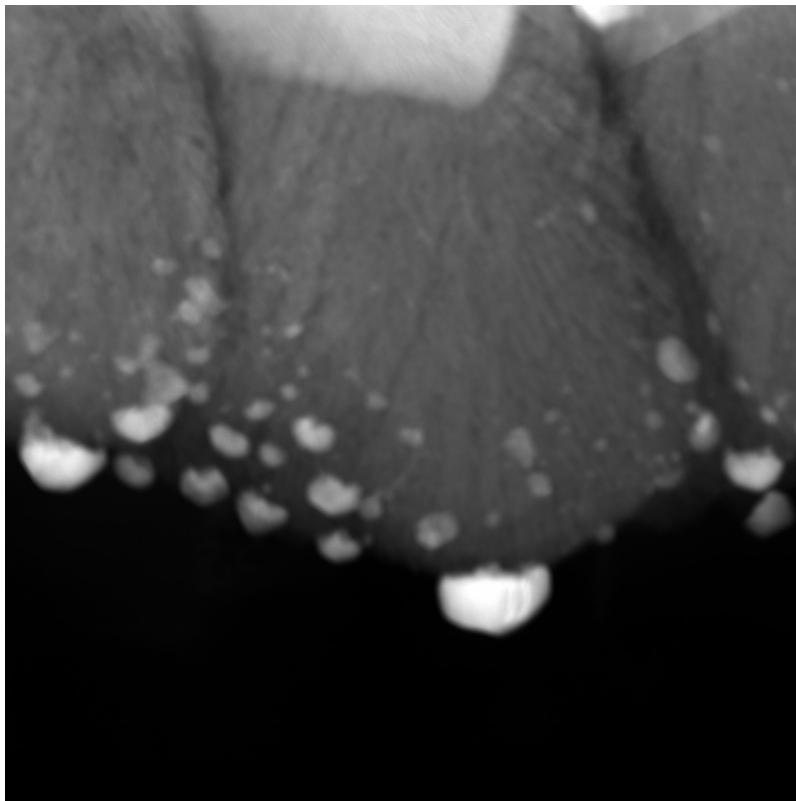


**Figure 6.14:** This figure presents SEM top view images of three AuAg/TiO<sub>2</sub> samples with the element ratios (5:1), (5:3) and (5:9). The synthesis parameters are analog to figure 6.13 except that Au was deposited first followed by a Ag layer.



(a)

**Figure 6.15:** *TEM image for AuAg (5:3) nanoparticle.*



**Figure 6.16:** *AgAu (1:5) Detail*

**Figure 6.17:** *HRTEM images for AgAu nanoparticles with element ratios of (1:5). The nanoparticles are loaded on a SiN grid that was deposited with 30 nm thick TiO<sub>2</sub>.*

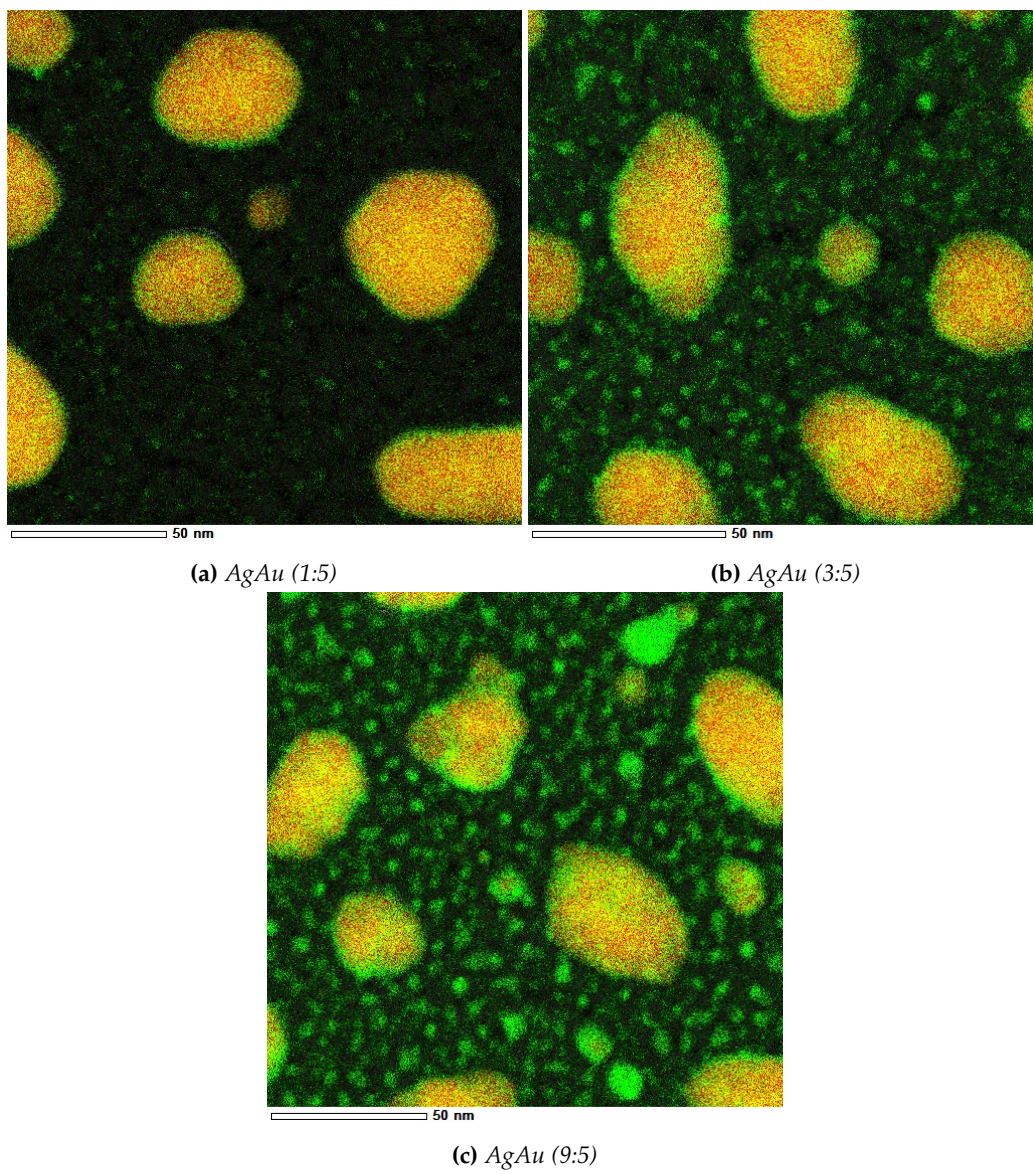


**Figure 6.18:** EDX mapping for *AgAu* (1:5) (a), *AgAu* (3:5) (b) and *AgAu* (9:5) (c).



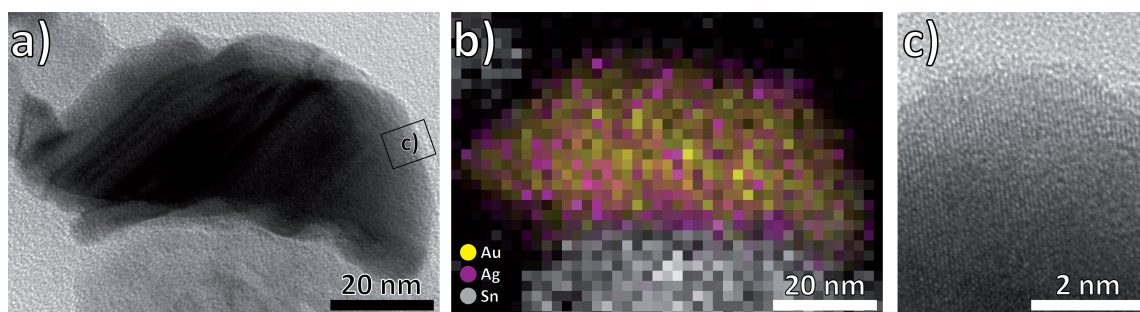


**Figure 6.19:** HRTEM and EDX images from AuAg (5:3) nanoparticles.

increased in intensity.

The observation of a single peak is unexpected for core-shell nanoparticles. Spherical core-shell structures generally show two peaks related to the outer shell material and the interface between core and shell. According to Lu et al. [134], Ag LSPR emergence is expected with a Ag shell thickness between 2.0 and 3.2 nm and the Au LSPR is repressed above a shell thickness of approximately 4 nm. Large core-shell nanoparticles should partly exceed the critical shell thickness and hence exhibit absorbance at the LSPR of Ag. However, no such peak was found which could indicate that only a small amount of particle possess Ag layers with the required thickness.

Other structures such as a physical mixture of two pure metals or alloy formation do not fit the results. A mixture of Ag and Au nanoparticle was found together with core-shell nanoparticles in EDX maps. However, they should exhibit two absorbance peaks: at 400 nm and 520 nm due to the excitation of localized surface plasmon resonance in Ag and Au, respectively [146][125]. Alloy formation, however, is characterized by one LSPR peak located between the one for the pure metals and depends on the elemental ratios [20][146][125][147]. Alloy formation was not found in TEM/EDX analysis (section 6.3.2).

The Ag-related LSPR could be covered by the TiO<sub>2</sub> absorbance beginning at 386 nm. This hypothesis is supported by optical spectroscopy done on pure Ag nanoparticles (appendix). A moderate increase in absorbance was observed at short wavelengths for pure Ag nanoparticles (figure 9.8 appendix), hence the cut-off wavelength of the underlying TiO<sub>2</sub> substrate may overlap with the LSPR of Ag and prevent its observation as an independent absorbance. The influence of elemental composition could only be observed on the Au LSPR that is located at longer wavelengths between 550 nm and 750 nm and became stronger with increasing Au content.

Another possibility for the missing LSPR of Ag could be its oxidation. Kracker et al. [20] observed no LSPR for pure Ag nanoparticle prepared by thermal annealing of a thin Ag film in their study. They argued that thermal annealing of Ag in the presence of oxygen led to the formation of Ag<sub>2</sub>O or AgO which was also partially observed under oxygen exclusion by Barreca [147]. The transformation from a metal to a metal oxide reduces the number of free electrons in the nanoparticles that could be excited for plasmon surface resonance. However, as stated above, a weak LSPR peak was observed for pure Ag and additionally EDX did not give an indication for Ag<sub>2</sub>O formation. Although such phenomenon has to be considered, it might not be the main reason for the absence of Ag peak.

### 6.3.4 Summary: bimetallic nanoparticles

Subsequent deposition of Au and Ag layers followed by thermal annealing resulted in Au-core Ag-shell nanoparticles, regardless of the deposition order. Increasing the Ag amount led to an increase in Ag shell thickness and the increased appearance of smaller pure Ag nanoparticles. The UV-vis spectra showed a single Au related peak that increased in intensity with increasing Au amount. No Ag related peak was observed because it was probably located at the  $\text{TiO}_2$  cut-off frequency and was overlapped.

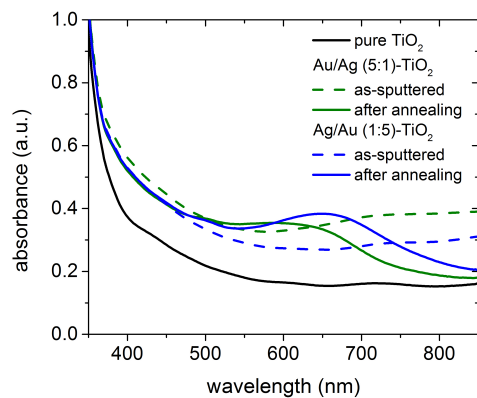
This physical plasma-based synthesis approach uniquely demonstrated a reproducible and robust non-chemical preparation method for the synthesis of Au-core Ag-shell nanoparticles. Because of its low costs, resource-saving and large area advantages; it has high potential for future large-scale applications in SERS enhanced spectroscopy or photocatalysis.

## 6.4 Photocurrent generation

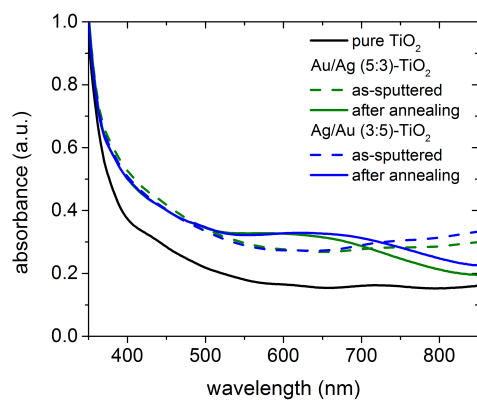
The systems Au/ $\text{TiO}_2$  and Au-Ag/ $\text{TiO}_2$  are very interesting for solar applications like water splitting [207][208][114][209][210] or photovoltaic [211][212]. Exposure to band gap irradiation can lead to photocharge generation in the semiconductor [213] that drives chemical reactions (solar water splitting) or results in photocurrent (photovoltaic). An enhancement in photocurrent density would result in high performing materials for photoelectrodes that can be used e.g. in solar cells. Metal nanoparticles such as Au and Ag are of special interest because they exhibit localized surface plasmon resonance [214][215]. Plasmonic excitation can significantly enhance the photocharge generation in a Au/ $\text{TiO}_2$  and Au-Ag/ $\text{TiO}_2$  system due to energy transfer mechanisms from the nanoparticles to the semiconductor.

This thesis systematically investigates variation in mono- and bimetallic nanoparticles including variation in Au amount and annealing parameters to find optimal materials and procedures for enhanced photocurrent generation. For the first time, magnetron sputtering-dewetted bimetallic Au-Ag core-shell structures are investigated for their photocurrent generation. This section focuses on comparing different deposition order and elemental ratios to find the most active system. Au nanoparticles were deposited on diverse anatase substrates such as DC sputtered, spincoated and AP-CVD prepared  $\text{TiO}_2$  because photoelectrochemical characterization of these Au/ $\text{TiO}_2$  systems give insights in the possible metal-metal oxide interface that is crucial for charge transport. To summarize, the overall aim of this section is to identify the preparation protocol that results in the highest photocurrent density; i.e. the largest amount of usable photocharge carriers.

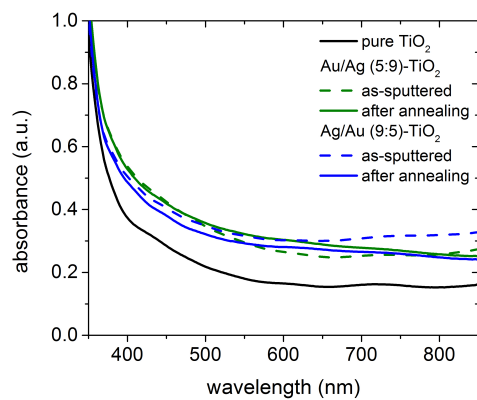
The amount of free charge carriers generated by, ideally, solar irradiation is fundamental in photoelectrochemistry and photocatalysis [216]. The influence of nanoparticle decoration on charge carrier generation was determined by measuring the anodic photocurrent in a photoelectrochemical half-cell configuration. Although the measurements changed the particle morphology by driving particle agglomeration during the experiment (which is discussed in section 9.0.18 in the appendix), relative photocurrent densities are still comparable and trends are relevant because the same procedures and experimental conditions were applied in an experimental series to provide maximal possible comparability. Photocurrent densities were measured by applying 800 mV to the samples and chopping the illumination in six consecutive on/off cycles. Two light sources were obtained that represented regions of the solar spectrum, i.e. illumination at 529 nm that overlapped with the transverse mode of Au nanoparticles and ultraviolet light with 378 nm wavelength.



(a)



(b)



(c)

**Figure 6.20:** Absorption spectra of  $\text{TiO}_2$  films with Au-Ag loadings. Only one LSPR peak is observed that decreased with decreasing Au content. The absence of a Ag-related plasmon peak could be due to Ag shells below the critical thickness or an overlap with the  $\text{TiO}_2$  absorbance band that obscure its visibility.

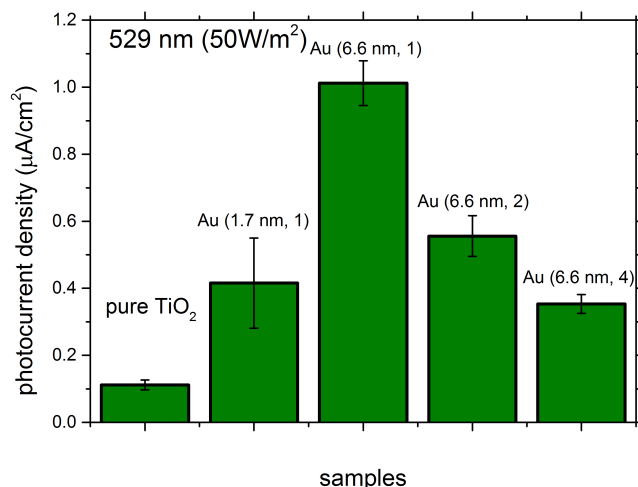


**Figure 6.21:** The optimal Au loading for photocurrent enhancement in visible light at 529 nm were exhibited by Au (6.6 nm, 1) nanoparticles with diameters of up to 65 nm.

#### 6.4.1 Variation of Au loading on DC sputtered $\text{TiO}_2$

Au nanoparticle decoration resulted in a photocurrent density enhancement compared to pure DC sputtered  $\text{TiO}_2$  when the photoelectrochemical half-cell was illuminated with 529 nm visible light as shown in figure 6.21. The photocurrent density increased from  $0.1 \mu\text{A}/\text{cm}^2$  for pure DC sputtered titania to  $0.42 \pm 0.13 \mu\text{A}/\text{cm}^2$  for Au (1.7 nm, 1) and reached an optimum enhancement of  $1 \mu\text{A}/\text{cm}^2$  for Au (6.6 nm, 1) with a maximal particle diameter of 65 nm. The photocurrent density decreased for the higher Au loadings of Au (6.6 nm, 2) and Au (6.6 nm, 4). The following paragraphs will discuss the origin of the enhanced photocurrent density by Au nanoparticle decoration compared to pure DC sputtered  $\text{TiO}_2$  before it will give explanations for the observation of an optimum in metal loading.

Au nanoparticles can enhance visible light photocurrent generation by three plasmon-induced energy transfer mechanisms: hot electron injection, electric-field enhancement and resonant scattering [217][62][218][61].

The injection of hot electrons from the Au nanoparticle to the semiconductor conduction band requires a sharp interface between both materials [219][149][110][66]. Such a large shared interface was suggested by HRTEM images for the oblate-shaped particles on top of the titania columns (figure 6.6). The formation of a direct contact between the metal and the semiconductor is an advantage of solid state dewetting processes and enables efficient charge transfer and separation [220]. Hence, hot electron injection is a possible mechanism for plasmonic enhancement in this Au/ $\text{TiO}_2$  system.

Plasmon excitation can further induce electric-field enhancement and scattering of incident photons on the nanoparticle that induce charge generation in the semiconductor [60]. This requires an overlap of the LSPR wavelength and the absorption of the semiconductor [221][66]. Visible light absorption of the titania can be achieved by defect states located within the semiconductors band gap [221]. Cyclic voltammetric measurements on DC sputtered  $\text{TiO}_2$  hint to the existence of such defect states (figure 9.10, appendix). Additionally, UV-vis spectra of pure DC sputtered  $\text{TiO}_2$  showed low light absorption in the entire visible region (figure 6.7) which could further indicate

the presents of such states [222][110]. Plasmon enhancement via electric-near field is possible, if these defect states exist.

Plasmon-induced scattering from the Au nanoparticles to increase the possibility for subsequent semiconductor light absorption, however, is only relevant for large nanoparticles and high particle densities [221]. Au (1.7 nm, 1) and Au (6.6 nm, 2) nanoparticles even reduce the reflectivity compared with the pure TiO<sub>2</sub> sample (figure 9.11 appendix). Although it occurs for larger particle, scattering should not have a dominant effect in photocurrent density enhancement.

Beside plasmon-induced energy transfer, metal nanoparticles also exhibit catalytic activity from faster injection of holes to the electrolyte. Haro et al. observed the excitation of LSPR in their Au/TiO<sub>2</sub> system, yet they showed that the photocurrent enhancement is due to a faster charge transfer [114]. The Au nanoparticles in this work showed, as a result of plasmon-induced energy transfer or faster charge transfer to the electrolyte, a photocurrent enhancement using a light source with wavelengths centered at 529 nm.

A correlation between plasmon resonance excitation and activity of the sample is commonly argued by emphasizing an overlap of an wavelength-dependent action spectra with the absorption spectra [148][149][152][223]. The incident photon-to-current efficiencies (IPCE) in this work showed no unambiguous correlation between resonance wavelength and wavelength-dependent photocurrent density enhancement for the Au samples (appendix figure 9.15). The tunable light source consisted of 23 discrete LEDs with light intensities of 1 W/m<sup>2</sup> that could be insufficient to induce a charge transfer so that further investigations with high-intensity light source are needed to clarify, if the observed charge carrier enhancement is plasmon induced.

Au nanoparticles showed an optimum in photocurrent density when their Au amount was varied. Increasing, an increase in the Au loading initially increased the photocurrent density to  $1.01 \pm 0.07 \mu\text{A}/\text{cm}^2$  for Au (6.6 nm, 1) before the photocurrent density decreased to  $0.35 \pm 0.03 \mu\text{A}/\text{cm}^2$  for Au (6.6 nm, 4). The initial enhancement probably originated from hot electron injection and/or near-field enhancement [110] as discussed above. Particles tend to increase in size with increasing Au amount, although the maximum particle diameter was similar for Au (6.6 nm, 1) and Au (6.6 nm, 2) and the size distributions are comparable. Hot electrons with a high energy distribution that are able to overcome the Schottky barrier and inject to the TiO<sub>2</sub> conduction band[224] are predominantly generated by small nanoparticles with diameters below 20 nm. Although Au (6.6 nm, 1) and Au (6.6 nm, 2) have similar maximal particle diameter of 65 nm and 68 nm, 48,5 % of the particles in Au (6.6 nm, 1) are up to 20 nm whereas with 41 % for Au (6.6 nm, 2) it is less. The increase in particle size with increasing Au loading could have reduced the number of electrons that contributed to electron injection. This means that hot electron injection had a significant contribution to the visible light enhancement of the Au nanoparticles.

Interestingly, the formation of an optimum in Au loading for photocurrent enhancement was reported with light sources that extended into the UV region and excited electron-hole pairs in the TiO<sub>2</sub>. The further increase in Au amount shielded the TiO<sub>2</sub> from incident light and decreased the titania surface area in contact with the electrolyte. The later prevented charge exchange with the ions in the electrolyte, namely the injection of photogenerated holes to the electrolyte species[221]. The 529 nm light source did not provided wavelengths in the UV region. It could be speculated, if the aforementioned defect states in the TiO<sub>2</sub> could have introduced a visible light response that was reduced by subsequent surface coverage with Au. However, further investigations are needed to validate the existence of these states and therefore hot electron injection from the Au nanoparticles are the preferred explanation.

### 6.4.2 Optimal annealing parameter for enhanced photocurrent generation

In the section concerning the optimal Au amount, Au (6.6 nm, 1) particles on TiO<sub>2</sub> showed a photocurrent density enhancement at 529 nm compared to pure DC sputtered TiO<sub>2</sub>; therefore this Au loading was selected as the invariant layer thickness for the variation of the annealing parameter. The variation in oxygen and argon as the gas atmosphere only showed differences for 30 min annealing at rapid heating (RH) (figure 6.22). Here, oxygen resulted in a stronger photocurrent density enhancement compared to argon. If the annealing treatment times were compared (figure 6.22b), no parameter set was superior.

There is no significant general difference between argon and oxygen gas (figure 6.22a), which is in accordance to the lack of differences in crystallite size, particle size and morphology and the LSPR position. Despite otherwise similar photocurrent densities of the prepared samples, 30 min RH showed a greater enhancement in oxygen than argon (figure 6.22b). The LSPR was shifted to greater wavelengths than the position of the argon annealing. However, the parameter set oxygen 30 min 2 K/min showed a similar shift and the related photocurrent density was more comparable to the argon sample. The crystallite sizes of the oxygen 30 min RH was with 9 nm lower than the 10 nm for argon. However, the parameter set for 30 min argon 2 K/min exhibited the same size as the oxygen sample. The superior enhancement of the oxygen 30min RH could not be explained either by the LSPR position or the morphology and might be a statistic artifact. However, as the 30 min oxygen RH treatment resulted in the highest photocurrent density, this parameter set was applied as the standard annealing method throughout the thesis.

This investigations, together with the previously conducted experiments that focused on the morphology and optical properties, showed that the thermal annealing parameters varied in this study did not significantly influence the properties of the nanoparticles concerning morphology, optical absorption, crystallinity or photocurrent enhancement.

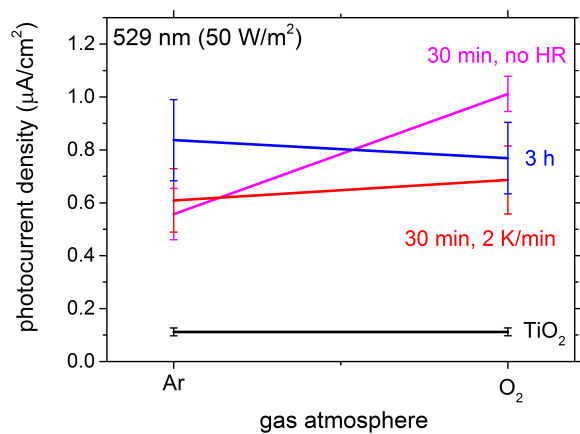
### 6.4.3 Variation of the TiO<sub>2</sub> substrate to investigate the influence of Au/TiO<sub>2</sub> interfaces

The interface between Au and the TiO<sub>2</sub> influences their photoelectrochemical activity because it determines charge transfer and separation. The following section introduces two TiO<sub>2</sub> substrates, namely porous TiO<sub>2</sub> prepared with a chemical-vapor-deposition (CVD) method at atmospheric pressure and spincoated TiO<sub>2</sub>. This gives the opportunity to investigate visible light charge carrier generation on a Au decorated substrate with different conductivity, recombination behavior and surface area as the DC sputtered titania.

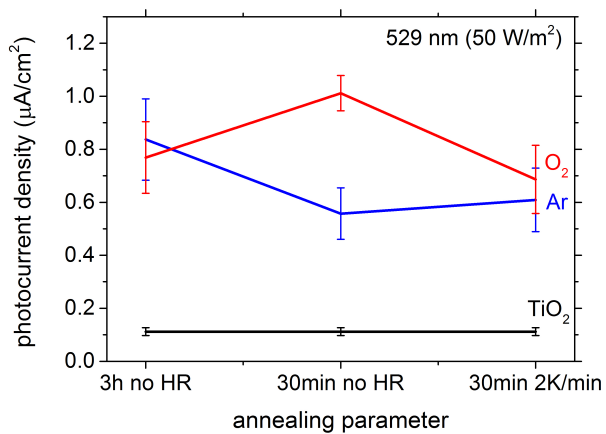
#### Atmospheric pressure chemical vapor deposition (AP-CVD)

Pure AP-CVD TiO<sub>2</sub> with thicknesses of 400 nm, 600 nm, 800 nm and 1000 nm varied in photocurrent density (figure 6.23). The most active titania sample had a thickness of 400 nm showing a photocurrent density of 0.11  $\mu\text{A}/\text{cm}^2$  and was followed by 800 nm thick titania exhibiting 0.06  $\mu\text{A}/\text{cm}^2$ . Layer thicknesses of 600 nm and 1000 nm generated comparable photocurrents of 0.04 and 0.03  $\mu\text{A}/\text{cm}^2$ , respectively. The higher photocurrent density generated by the 400 nm thick layer could be related to its low film thickness. Thinner semiconducting layers usually exhibit lower charge recombination than extended ones because of the shorter diffusion path for the photocharges to the ohmic contact [225].

Deposition of Au (6.6 nm, 2) nanoparticles resulted in a significant photocurrent density enhancement at 529 nm wavelength. The strongest enhancement was reached by Au deposited on a 800 nm thick layer ( $0.70 \pm 0.09 \mu\text{A}/\text{cm}^2$ ) followed by the Au covered 1000 nm ( $0.65 \pm 0.09 \mu\text{A}/\text{cm}^2$ )



(a)



(b)

**Figure 6.22:** Annealing atmosphere of Au (6.6 nm, 1) nanoparticles differ at 30 min annealing with RH where oxygen gave rise to 1  $\mu\text{A}/\text{cm}^2$  at 800 mV and 529 nm illumination. In comparison, no annealing time was superior.

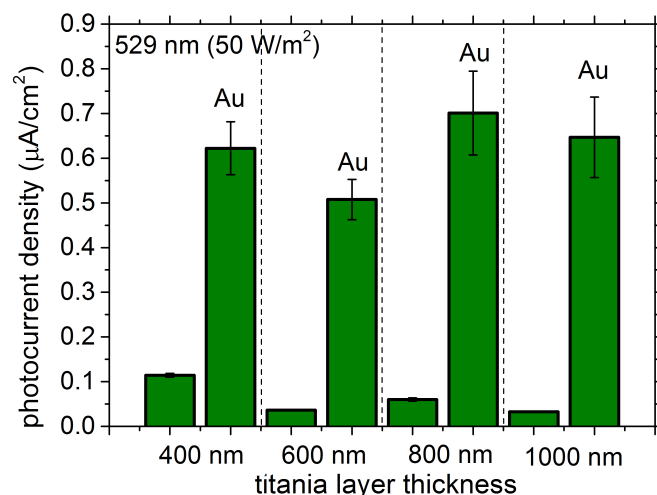


**Figure 6.23:** *Au nanoparticles increased the photocurrent of AP-CVD TiO<sub>2</sub> at 529 nm regardless of titania layer thickness.*

and 400 nm titania ( $0.62 \pm 0.06 \mu\text{A}/\text{cm}^2$ ) that are comparable. All samples except for the Au/TiO<sub>2</sub> sample with 600 nm titania thickness showed a higher photocurrent density than the  $0.56 \pm 0.06 \mu\text{A}/\text{cm}^2$  reached by the same Au loading on DC sputtered TiO<sub>2</sub> (figure 6.21).

The improved enhancement of the Au/AP-CVD TiO<sub>2</sub> for layer thicknesses of 400 nm, 800 nm and 1000 nm compared to Au/DC sputtered TiO<sub>2</sub> could result either from more preferable properties of the nanoparticles (e.g. morphology, size and size distribution) or a Au/TiO<sub>2</sub> interface that allows faster charge transfer and better charge separation. Although no significant differences in morphology of the Au nanoparticles compared to Au/DC sputtered TiO<sub>2</sub> is observed in top view SEM images (figure 6.25), UV-Vis spectra suggested more spherical nanoparticles than formed on the DC sputtered TiO<sub>2</sub> that could explain differences in the photocurrent generation. The photocurrent density generation did not correlate with the absorbance of the sample. Pure AP-CVD TiO<sub>2</sub> showed the highest absorbance in the visible region at 800 nm thickness as seen in figure 9.9 in the appendix (highest photocurrent density was 400 nm thickness, figure 6.23) whereas 1000 nm thickness exhibited the highest absorbance for Au/AP-CVD TiO<sub>2</sub> sample as seen in figure 9.12 in the appendix (strongest photocurrent at 800 nm thickness). Therefore, the photocurrent density could not be related to strong absorbance or LSPR but rather to the Au particle morphology, size or size distribution and their interface with the titania.

### Spincoated TiO<sub>2</sub>

Spincoating of a titania solution allowed to embed sputtered Au nanoparticles into the titania matrix additionally to deposition on the surface (Top view SEM image is shown in figure 9.16 in the appendix). Interestingly, the introduction of Au nanoparticle combined with spincoated TiO<sub>2</sub> generally showed a negative effect on the photocurrent density. The sandwich structure, i.e. Au (1.7 nm, 1) on top and as well as embedded additionally in the matrix, showed highest photocurrent density of  $0.056 \pm 0.003 \mu\text{A}/\text{cm}^2$ , yet it was below the photocurrent density of  $0.09 \pm 0.01 \mu\text{A}/\text{cm}^2$  for pure spincoated TiO<sub>2</sub> (figure 6.24). Au (6.6 nm, 1) nanoparticle that exhibited the highest



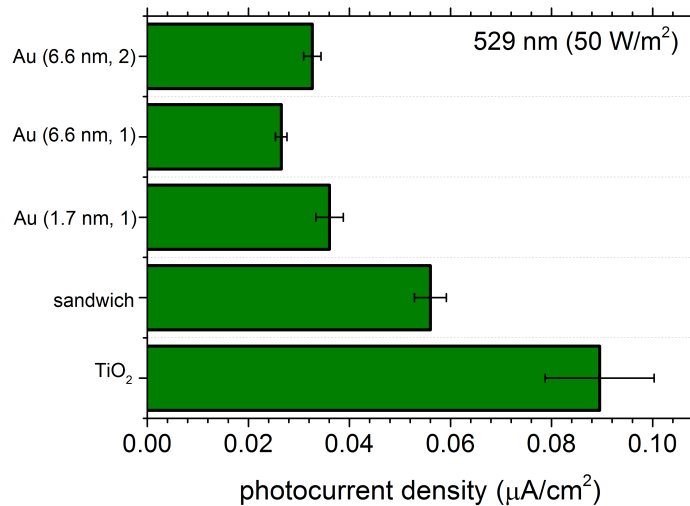


**Figure 6.24:** Au nanoparticle loading reduces the photocurrent at 529nm for spincoated TiO<sub>2</sub> samples.

photocurrent density on DC sputtered TiO<sub>2</sub> resulted in the lowest photocurrent density on spincoated titania.

Such a decrease in activity was not expected because generally the embedment of Au nanoparticles in titania is known to improve the film conductivity, the absorption and the charge transfer [113]. Negative effect of Au introduction on TiO<sub>2</sub> systems at visible light are scarcely reported. Naseri et al. [113] attributed it to a coverage of the semiconductor surface from illumination by large Au particles. He used a filter to cut-off wavelengths below 390 nm and ensured exclusive visible light excitation. In visible light, however, TiO<sub>2</sub> should be inactive and "shadowing" of the semiconductors surface should not influence the charge generation. Furthermore, the SEM image of Au (6.6 nm, 1)/TiO<sub>2</sub> showed large isolated particles with dimensions up to 50 nm between accessible bare TiO<sub>2</sub> surfaces as well as Au/TiO<sub>2</sub>/electrolyte sites. Rather than shielding the titania surface, the introduction of defect states that act as recombination centers [113] is more plausible. The increase in recombination by the Au nanoparticle could explain the decrease in photocurrent density generation compared to pure titania.

Another critical issue is the metal/semiconductor interface. The spincoated TiO<sub>2</sub> substrate consisted of elongated semiconducting nanoparticles with dimensions of 30 nm (figure 6.26) providing a rough surface. After dewetting, the rough structure may just provided few interface area with the large 50 nm metal nanoparticles that aimed for a minimized surface energy. In this case, the charge transfer would have been hindered and recombination promoted. This hypothesis was supported by the embedded Au nanoparticles in the sandwich sample that were expected to have a large interface with the TiO<sub>2</sub> and that showed the highest photocurrent density among the Au/spincoated TiO<sub>2</sub> samples.

These two examples of TiO<sub>2</sub> with different porosity and surface roughness suggested a major significance of the Au/TiO<sub>2</sub> interface to photocurrent density generation. Dewetted Au nanoparticles generally exhibited a close contact with the substrate, however, their tendency to form spherical shapes in order to lower their surface energy per area could have resulted in low contact areas with the rough TiO<sub>2</sub> surface that showed features in the dimensions of tens-of-nanometers. This effect should be considered for nanoparticle sizes comparable to the

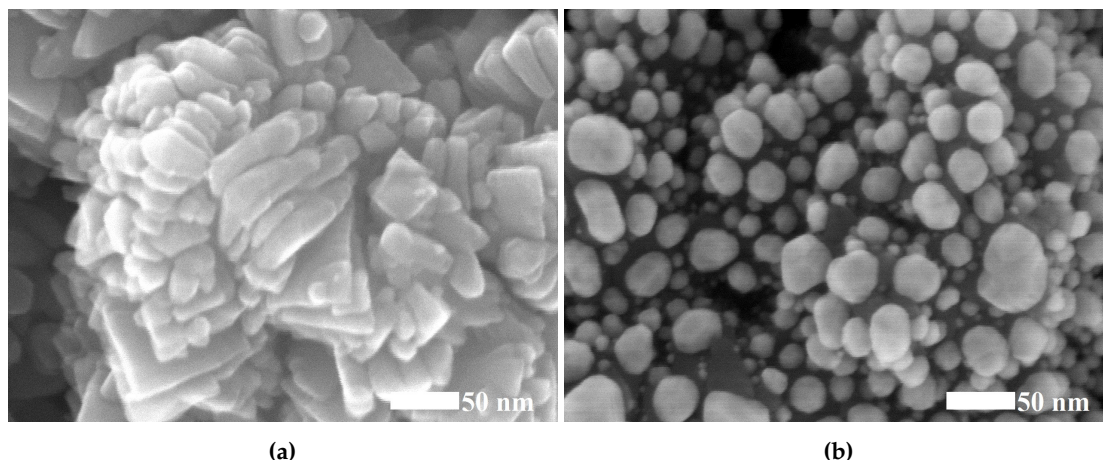


**Figure 6.25:** Top view SEM micrographs of (a) as received AP-CVD TiO<sub>2</sub> and (b) after deposition of Au (6.6 nm, 2) nanoparticles.

substrate domain sizes whereas it should be irrelevant for smaller particles.

#### 6.4.4 Photocurrent density increase by bimetallic AuAg and AgAu nanoparticles

All bimetallic Au-Ag nanoparticles resulted in a photocurrent enhancement at 529 nm illumination (figure 6.27). Ag as a first layer resulted throughout in a higher photocurrent than the reverse deposition order. Ag/Au with the highest amount of Au reached the strongest enhancement with a photocurrent density of  $1.18 \mu\text{A}/\text{cm}^2$ . The ratios AgAu (1:5) and AgAu (9:5) exhibited a stronger photocurrent density than Au (6.6 nm, 1) with  $1 \mu\text{A}/\text{cm}^2$ . AgAu (3:5) while all ratios for the AuAg series showed lower photocurrent densities. No trend of the elemental ratio with the activity was found that was valid for both deposition orders. The AgAu nanoparticles showed the highest photocurrent density of all investigated samples in this work.

Bimetallic Au-core Ag-shell nanoparticles showed a high photocurrent density generation because of the strong plasmon resonance of the Ag. It is known that Ag nanoparticles exhibit a strong LSPR because its resonance wavelength is separated from the Ag interband transitions starting at 3.87 eV (320 nm) [5][226]. However, no Ag-related LSPR peak was found in the UV-vis and it was speculated if it overlapped with the TiO<sub>2</sub> absorption. Even though this overlap would be beneficial as it offers the possibility for near-field enhancement and scattering, this spectral region is not excited by the 529 nm illumination source. A plasmonic enhancement is therefore reduced to the influence of the Au-related LSPR.

Lim et al. [227] found an optimal Au:Ag ratio for 75:25 wt% in dye-sensitized solar cells and Wang et al. [228] found an optimum for a Ag:Au ratio of (0.19:0.81) for the oxidation of p-aminothiophenol. The high conductivity and catalytic activity of the Au nanoparticle could be responsible for the high activity of the composite as well as the improved charge transfer. Although the advantage of a high Au amount in the Au-Ag nanoparticles is in accordance with the superior enhancement of AgAu (1:5), there is no trend in this study between the elemental ratio and the photocurrent density. The AgAu (1:5) sample, however, showed the highest LSPR intensity of all samples.

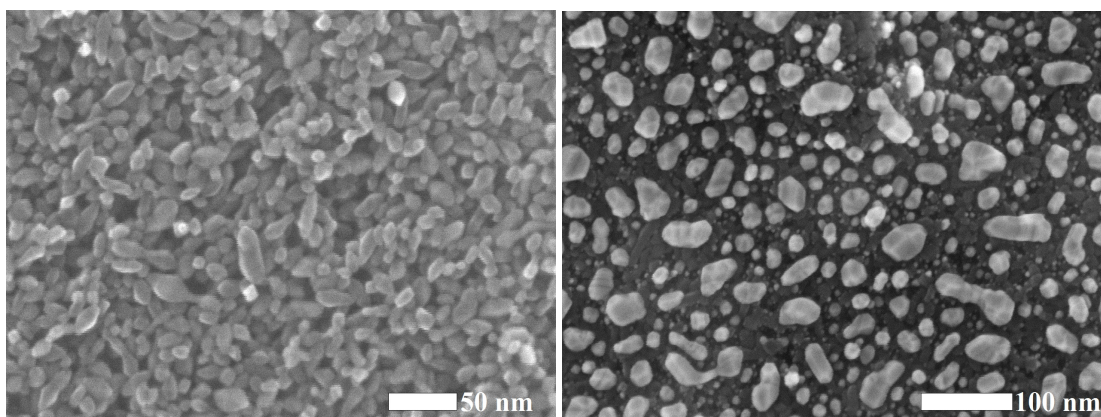


**Figure 6.26:** (left): SEM images of  $\text{TiO}_2$  solution spincoated on FTO glass (right): SEM images of Au (6.6 nm, 1)/ $\text{TiO}_2$  spincoated on FTO glass.

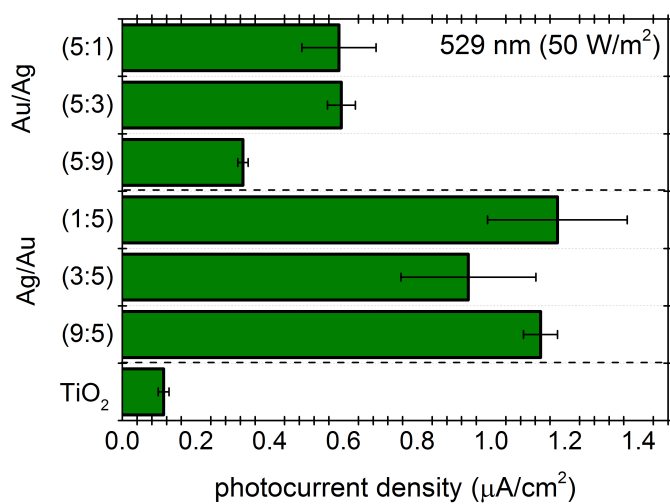


**Figure 6.27:** Ag-Au nanoparticles with Ag deposited first showed higher photocurrents at 529 nm than the preparation with reversed order.

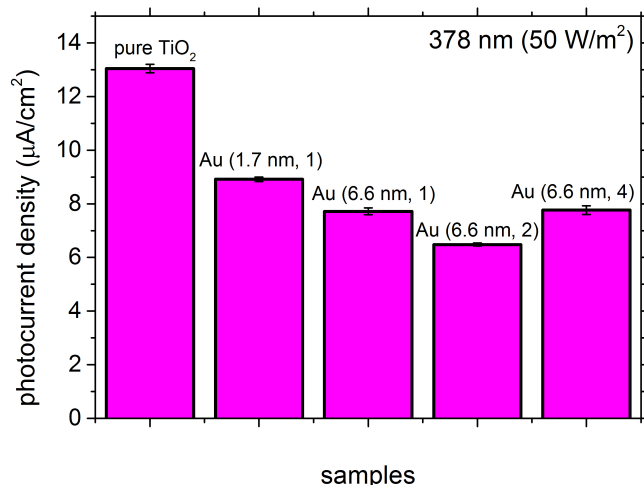


**Figure 6.28:** Au loading leads to a significant decrease in photocurrent at 378 nm.

The deposition order influenced the photocurrent density and AgAu samples showed a higher photocurrent density than the reverse order. UV-vis measurements in section 6.3.3 revealed that the LSPR peak for the AgAu samples was shifted to longer wavelengths for the two highest Au amounts. This suggested that either the morphology or the composition of the particles differed. SEM images did not show a significant difference in the morphology, however, the shell thicknesses could have differed. If the photocurrent enhancement was mainly related to the Au-related LSPR than the introduction of the passive Ag could reduce the photocurrent enhancement compared to monometallic Au.

#### 6.4.5 Decrease in photocurrent by Au decoration

All metal/TiO<sub>2</sub> samples investigated in this work showed, contrary to visible light illumination, a decrease in photocurrent density compared to pure TiO<sub>2</sub> under UV irradiation. Figure 6.28 presents the data of various Au loadings as a representative example. The Au (6.6nm, 2) sample showed the lowest photocurrent density compared to other Au loadings, whereas Au (1.7nm, 1) nanoparticles resulted in the least photocurrent density reduction. Another phenomenon under UV (378 nm) was an overshoot in photocurrent density at the beginning of every light-on-cycle before converting to a steady state value (figure 9.17, appendix).

This is in contrast to UV-induced photocurrent enhancement found by other researcher [229]. In UV light, electron hole pairs are generated in the TiO<sub>2</sub> [110]. The electrons are transferred to the Au nanoparticle [229]. They are electron-sinks and prevent charge recombination [230]. Pu et al. [221] speculate that Au nanoparticle could erase trap states on the surface of the TiO<sub>2</sub> semiconductor that would otherwise prevent photo-generated holes to reach the electrolyte. This effect is termed surface passivation. Furthermore surface plasmon induced electric-field amplification in the vicinity of the semiconductor is also considered in the UV light [221].

A reduction in photocurrent of TiO<sub>2</sub> after Au nanoparticle decoration was observed previously in the literature [110][231][60]. The Au nanoparticles reduce the the surface area of the TiO<sub>2</sub> that is illuminated and in contact with the electrolyte [110][60]. The ability of Au nanoparticles to act

as electron sinks due to their Schottky barrier [232] and trap the photoelectrons generated by the  $\text{TiO}_2$  [233] was argued to be responsible for the low photocurrent.

#### 6.4.6 Summary: photocurrent generation

Photocurrent density measurements were performed using a PEC half-cell set-up to compare different preparation parameters and find optimal configurations for high charge carrier generation. The introduction of Au nanoparticles on DC sputtered  $\text{TiO}_2$  resulted in a photocurrent density enhancement at an illumination wavelength of 529 nm. Further IPCE measurements with a high-intensity light source are needed to correlate the photocurrent density enhancement with the LSPR absorption. The particles exhibited a close interface with the titania that suggested plasmon-induced electron injection to be the most promising mechanism for the observed enhancement. High Au amount resulted in larger groups of particles with diameters up to 20 nm that generate low energetic hot electrons that cannot pass the Schottky barrier and decrease the photocurrent density. The optimal enhancement showed the Au (6.6 nm, 1)/ $\text{TiO}_2$  sample.

The Au (6.6 nm, 1)/ $\text{TiO}_2$  sample was annealed by varying the gas atmosphere (oxygen, argon), the time (30 min, 3 h) and the applied temperature ramp (none or 2 K/min). The samples showed no significant differences in photocurrent density generation, which is in accordance with the insignificant variation in morphology, size, crystallinity and LSPR position observed in section 6.2.

The deposition of Au nanoparticles on AP-CVD and spincoated  $\text{TiO}_2$  substrates revealed the importance of a sufficiently good interface between the metal and the semiconductor. Au/spincoated  $\text{TiO}_2$  showed a decrease in photocurrent compared to pure spincoated  $\text{TiO}_2$ . This suggests the introduction of defect states and the role of Au nanoparticles as recombination centers. The tendency of Au to form spherical shapes upon annealing in order to minimize its surface energy density could result in small contact areas with the nanostructured semiconductors that exhibited domains in the order of tens-of-nanometers.

Bimetallic Au-Ag nanoparticles showed a photocurrent enhancement under illumination with 529 nm. The wavelength of the light source, however, was only able to excite a Au-related LSPR absorption peak. The AgAu deposition showed a higher photocharge response than the reverse deposition order. A comparison of the peak positions from the same elemental ratio with the complementary deposition order indicated a variation in the particle properties such as the shell thickness. Hence, the preferred charge generation for AgAu/ $\text{TiO}_2$  is probably related with the initial core-shell formation during the synthesis.

The Au nanoparticles decreased the photocurrent density of the photoactive  $\text{TiO}_2$  under illumination with 378 nm UV light due to a reduction of the illumination area and the area of the  $\text{TiO}_2$  that is in contact with the electrolyte.

The high photocurrent density enhancement of AgAu (1:5)/ $\text{TiO}_2$  at 529 nm proved its potential as a material for photoelectrodes.

## Conclusion

This thesis presented a plasma-based method for the preparation of Au and Au-Ag nanoparticles, characterized the morphology of the nanostructures and their optical properties and evaluated optimal parameters for photocurrent density enhancement. This enhancement in photocurrent density showed the ability of the systems to generate charge carriers under visible light illumination, which is an important result as photo-induced charges can drive chemical reaction and can be used in photovoltaic devices.

Au and Au-Ag nanoparticles were prepared by a combination of magnetron sputtering and subsequent thermal annealing. TiO<sub>2</sub> substrates were prepared by direct current (DC) sputtering, atmospheric pressure chemical vapor deposition and spincoating. Their surface morphology determined the particle growth while the interface between the Au and the DC sputtered TiO<sub>2</sub> was crucial for efficient charge transfer. In contrast, Au nanoparticles seemed to share low surface areas with the spincoated TiO<sub>2</sub> that exhibited a rough surface with elongated TiO<sub>2</sub> particle having sizes of approximately 30 nm. Upon thermal annealing, Au atoms diffused in order to form a shape with low surface energy per area; ideally a sphere. The comparable size of the Au nanoparticles ( $\approx$  50 nm diameter) with the TiO<sub>2</sub> domains could have resulted in small contact areas that impeded charge transfer and introduced centers for recombination. This would explain the observed reduction in photocurrent density for Au decoration compared with pure spincoated TiO<sub>2</sub> upon illumination with 529 nm wavelength.

The properties of the Au nanoparticles deposited on DC sputtered TiO<sub>2</sub> such as the morphology, plasmon resonance position and photocurrent density generation were independent from the varied annealing parameter, i.e. annealing time (30 min, 3 h) the temperature ramp (2 K/min or none) and the composition of the gas atmosphere (oxygen and argon). The most important parameter to tune the aforementioned Au nanoparticles properties were the initial Au layer thickness, the number of deposition-annealing cycles and the morphology of the TiO<sub>2</sub> substrate. DC sputtered TiO<sub>2</sub> exhibited a cauliflower-like structure with columns having diameter of approximately 200 nm and a nanometer-roughness. The influence of the substrate on the particle growth was dominant for high Au amounts and was first observed after dewetting of Au layer with a nominal layer thickness of 6.6 nm. Small spherical nanoparticles were found close to the columns edge while large, oblate particles formed on top of the titania columns. This was probably caused by the lower initial layer thickness near the column edges due to the orientation of the substrate to the magnetron, to shadowing effects and to surface diffusion barriers. The non-spherical shape of the largest particles enable electron oscillation with orientation depending restoring forces that resulted in longitudinal and transverse localized surface plasmon resonance

absorptions.

The Au nanoparticles shared a large surface area with the DC sputtered TiO<sub>2</sub> that resulted, under illumination with 529 nm wavelength, in efficient photocharge transfer due to hot electron injection from the Au to the TiO<sub>2</sub>. The photocurrent density increased for increasing Au amount, reached an optimum for Au (6.6 nm, 1) and then decreased. High Au loadings contained fewer nanoparticles with diameter under 20 nm that could generate hot electrons with enough energy to overcome the Schottky barrier. Their decrease in number could explain the reduced photocurrent density due to more insufficient electron transfer.

Bimetallic Au-Ag nanoparticles were prepared by depositing a Ag on a Au layer as well as by a reversed deposition order (i.e. Ag-Au-annealing). Thermal annealing caused the formation of large Au-core Ag-shell particles with diameters of approximately 40 nm as well as smaller Ag particles with sizes up to 10 nm. A Ag shell with a thickness of ca.1-2 nm formed regardless of the deposition order because, which was explained by the lower surface energy per area of Ag compared to Au. The bimetallic nanoparticles showed a Au-related plasmon peak for Au:Ag ratios of (5:1) and (5:3) while the expected Ag-related plasmon resonance peak was not observed and probably overlapped with the TiO<sub>2</sub> absorbance. The Au-related plasmon resonance was possibly responsible for the enhanced photocurrent density for the AuAg/DC sputtered TiO<sub>2</sub> and the AgAu/DC sputtered TiO<sub>2</sub> compared to pure DC sputtered TiO<sub>2</sub>. The AgAu (1:5) sample showed, with a photocurrent density of 1.18  $\mu$ A, the highest enhancement for all investigated samples.

Nanoparticle decoration, however, led to a general decrease in photocurrent density compared to the corresponding pure TiO<sub>2</sub> when UV light with a wavelength of 378 nm was used. TiO<sub>2</sub> is photoactive at wavelengths below 386 nm and can generate electron-hole pairs. The nanoparticles shielded the TiO<sub>2</sub> surface from the incident light and reduced its interfacial area with the electrolyte.

This thesis demonstrated the potential of magnetron sputtering in combination with thermal annealing as a low-waste, solvent-free preparation method with potential for large-scale applications. This physical plasma-based synthesis approach even facilitates a uniquely, reproducible and robust non-chemical preparation method for the synthesis of Au-core Ag-shell nanoparticles. The photocharge generation of the nanoparticles are too low to compete with existing systems e.g. in photovoltaic. However, the low-cost, resource-saving nanoparticle preparation method could be interesting for purely plasmonic application such as surface-enhanced Raman spectroscopy.

## Acknowledgement

This thesis would not been possible without the expertise, support and ideas from Prof. Dr. Lochbrunner, Dr. Volker Brüser and Dr. Angela Kruth. During my PhD time, numerous members from the INP have supported me and I wholeheartedly thank Daniel Köpp, Karl-Heinz Schmidt, Dr. Jan Schäfer, Uwe Lindemann, Dr. Harm Wulff, Kirsten Anklam, Anja Albrecht, Dr. Antje Quade, Dagmar Jasinski, Gustav Sievers, Frank May, Steffen Müller and Christian Walter. Very important contributions were made from Dr. Marga-Martina Pohl from the LIKAT, Alexander Müller from the MPIE and Ing. Thomas Abendroth and Dr. Holger Althues from Fraunhofer Institut für Werkstoff- und Strahltechnik. This thesis is a result of a priority project funded by the German Research Society. The positive influence of Dr. Michael Karnahl, Dr. Henrik Junge, Prof. Dr. Christina Scheu, Dr. Stefanie Tschierlei, Jaqueline Priebe and Dr. Alastair Lennox was highly appreciated. Furthermore, I had the great honor to visit Hokkaido University in Sapporo thanks to Dr. Kosei Ueno, Prof. Misawa and Dr. Xu Shi. Beside academic supervision, there is always a moral support from family and friends. Naturally, my biggest thank you is directed to my wonderful mother! I have the great fortune to be surrounded by amazing and caring friends: Jan Wallis, Ann-Pierra Herrendorf, Jana Kredl, Birgit Schabinger, Steffen Drache, Vladimir Shuskov, Marian Putscher, Robert Morzek, Thomas Koch, Prof. Rainer Hippler, Marco Rosenbusch, Mathias Pamperin, Susanne Gerhardt, Stefan Knauer, Tim Teichmann, Thomas Wegner, Carsten Killer, Andreas Pieper, Christian Wurl (née Schultz) Georg Teiser, Martin Langowski and Fabian Szymik. The dearest reader rest assured that every name in these lists corresponds to an amazing and wonderful person.



## Bibliography

- [1] Eleonora Petryayeva and Ulrich J. Krull. Localized surface plasmon resonance: Nanostructures, bioassays and biosensing-a review. *Analytica Chimica Acta*, 706(1):8 – 24, 2011.
- [2] K. Lance Kelly, Eduardo Coronado, Lin Lin Zhao, and George Schatz. The optical properties of metal nanoparticles: the influence of size, shape, and dielectric environment. *The Journal of Physical Chemistry B*, 107(3):668–677, 2003.
- [3] Xuming Zhang, Yu Lim Chen, Ru-Shi Liu, and Din Ping Tsai. Plasmonic photocatalysis. *Reports on Progress in Physics*, 76(4):046401, 2013.
- [4] Colleen L. Nehl and Jason H. Hafner. Shape-dependent plasmon resonances of gold nanoparticles. *J. Mater. Chem.*, 18:2415–2419, 2008.
- [5] Prashant K. Jain and Mostafa A. El-Sayed. Plasmonic coupling in noble metal nanostructures. *Chemical Physics Letters*, 487(4):153 – 164, 2010.
- [6] Pierre Colson, Catherine Henrist, and Rudi Cloots. Nanosphere lithography: A powerful method for the controlled manufacturing of nanomaterials. *Journal of Nanomaterials*, 2013:19, 2013.
- [7] Traci R. Jensen, Michelle Duval Malinsky, Christy L. Haynes, and Richard P. Van Duyne. Nanosphere lithography: tunable localized surface plasmon resonance spectra of silver nanoparticles. *The Journal of Physical Chemistry B*, 104(45):10549–10556, 2000.
- [8] Claudia Manuela Müller, Flavio Carlo Filippo Mornaghini, and Ralph Spolenak. Ordered arrays of faceted gold nanoparticles obtained by dewetting and nanosphere lithography. *Nanotechnology*, 19(48):485306, 2008.
- [9] D. Gaspar, A. C. Pimentel, T. Mateus, J. P. Leitão, J. Soares, B. P. Falcão, A. Araújo, A. Vicente, S. A. Filonovich, H. Águas, R. Martins, and I. Ferreira. Influence of the layer thickness in plasmonic gold nanoparticles produced by thermal evaporation. *Scientific Reports*, 3:1469, 2013.
- [10] Jakub Siegel, Ondřej Kvítek, Petr Slepíčka, Joseph Náhlík, J. Heitz, and V. Švorčík. Structural, electrical and optical studies of gold nanostructures formed by Ar plasma-assisted sputtering.

*Nuclear Instruments and Methods in Physics Research Section B: Beam Interactions with Materials and Atoms*, 272:193 – 197, 2012. Proceedings of the 17th International Conference on Ion Beam Modification of Materials (IBMM 2010).

- [11] Jakub Siegel, Robert Krajcar, Zdeňka Kolská, Vladimír Hnatowicz, and Václav Švorčák. Annealing of gold nanostructures sputtered on polytetrafluoroethylene. *Nanoscale Research Letters*, 6(1):588–588, 2011.
- [12] Piyapong Asanithi, Surasing Chaiyakun, and Pichet Limsuwan. Growth of silver nanoparticles by DC magnetron sputtering. *Journal of Nanomaterials*, 2012:8, 2012.
- [13] R. Herizchi, E. Abbasi, M. Milani, and A. Akbarzadeh. Current methods for synthesis of gold nanoparticles. *Artificial Cells, Nanomedicine, and Biotechnology*, 2014.
- [14] Kholoud M.M. Abou El-Nour, Ala’a Eftaiha, Abdulrhman Al-Warthan, and Reda A.A. Ammar. Synthesis and applications of silver nanoparticles. *Arabian Journal of Chemistry*, 3(3):135 – 140, 2010.
- [15] Jongpil Ye. Investigation of the mechanism of solid-state dewetting of silver thin films using spatial correlation analysis of hole patterns. *Applied Physics Express*, 7(8):085601, 2014.
- [16] Raphael Clearfield, Justin G. Railsback, Ryan C. Pearce, Dale K. Hensley, Jason D. Fowlkes, Miguel Fuentes-Cabrera, Michael L. Simpson, Philip D. Rack, and Anatoli V. Melechko. Reactive solid-state dewetting of Cu-Ni films on silicon. *Applied Physics Letters*, 97(25):253101, 2010.
- [17] M. Can Günendi, İrem Tanyeli, Gürsoy B. Akgüç, Alpan Bek, Raşit Turan, and Oğuz Gülseren. Understanding the plasmonic properties of dewetting formed Ag nanoparticles for large area solar cell applications. *Opt. Express*, 21(15):18344–18353, Jul 2013.
- [18] H Krishna, Ritesh Sachan, J Strader, Christopher Favazza, Mikhail Khenner, and Ramki Kalyanaraman. Thickness-dependent spontaneous dewetting morphology of ultrathin Ag films. 21, 04 2010.
- [19] Anna Kosinova, Dong Wang, Peter Schaaf, Oleg Kovalenko, Leonid Klinger, and Eugen Rabkin. Fabrication of hollow gold nanoparticles by dewetting, dealloying and coarsening. *Acta Materialia*, 102(Supplement C):108 – 115, 2016.
- [20] Michael Kracker, Christian Worsch, Christian Bocker, and Christian Rüssel. Optical properties of dewetted thin silver/gold multilayer films on glass substrates. *Thin Solid Films*, 539:47 – 54, 2013.
- [21] G Seguíni, J Llamoya Curi, S Spiga, G Tallarida, C Wiemer, and M Perego. Solid-state dewetting of ultra-thin Au films on SiO<sub>2</sub> and HfO<sub>2</sub>. *Nanotechnology*, 25(49):495603, 2014.
- [22] Minhee Kang, Sang-Gil Park, and Ki-Hun Jeong. Repeated solid-state dewetting of thin gold films for nanogap-rich plasmonic nanoislands. *Scientific Reports*, 5:14790, 2015.
- [23] A. Serrano, O. Rodríguez de la Fuente, and M. A. García. Extended and localized surface plasmons in annealed Au films on glass substrates. *Journal of Applied Physics*, 108, 2010.
- [24] Anna Kosinova, Oleg Kovalenko, Leonid Klinger, and Eugen Rabkin. Mechanisms of solid-state dewetting of thin Au films in different annealing atmospheres. *Acta Materialia*, 83(Supplement C):91 – 101, 2015.

- [25] P Farzinpour, A Sundar, K D Gilroy, Z E Eskin, R A Hughes, and S Neretina. Altering the dewetting characteristics of ultrathin gold and silver films using a sacrificial antimony layer. *Nanotechnology*, 23(49):495604, 2012.
- [26] Jongpil Ye and Carl V. Thompson. Regular pattern formation through the retraction and pinch-off of edges during solid-state dewetting of patterned single crystal films. *Phys. Rev. B*, 82:193408, Nov 2010.
- [27] S. A. Jang, H. J. Lee, C. V. Thompson, C. A. Ross, and Y. J. Oh. Crystallographic analysis of the solid-state dewetting of polycrystalline gold film using automated indexing in a transmission electron microscope. *APL Materials*, 3(12):126103, 2015.
- [28] Anya Muzikansky, Pilkhaz Nanikashvili, Judith Grinblat, and David Zitoun. Ag dewetting in Cu@Ag monodisperse core-shell nanoparticles. *The Journal of Physical Chemistry C*, 117(6):3093–3100, 2013.
- [29] S. Grammatikopoulos, S. D. Pappas, V. Dracopoulos, P. Pouloupoulos, P. Fumagalli, M. J. Velgakis, and C. Politis. Self-assembled Au nanoparticles on heated corning glass by dc magnetron sputtering: size-dependent surface plasmon resonance tuning. *Journal of Nanoparticle Research*, 15(2):1446, Jan 2013.
- [30] J. Okumu, C. Dahmen, A. N. Sprafke, M. Luysberg, G. von Plessen, and M. Wuttig. Photochromic silver nanoparticles fabricated by sputter deposition. *Journal of Applied Physics*, 97(9):094305, 2005.
- [31] F. Hajakbari and M. Ensandoust. Study of thermal annealing effect on the properties of silver thin films prepared by DC magnetron sputtering. *ACTA PHYSICA POLONICA A*, 129(4), 2016.
- [32] A Belahmar and A Chouiyakh. Sputtering synthesis and thermal annealing effect on gold nanoparticles in Al<sub>2</sub>O<sub>3</sub> matrix. 2:100–103, 01 2016.
- [33] Alexander B. Tesler, Ben M. Maoz, Yishay Feldman, Alexander Vaskevich, and Israel Rubinstein. Solid-state thermal dewetting of just-percolated gold films evaporated on glass: Development of the morphology and optical properties. *The Journal of Physical Chemistry C*, 117(21):11337–11346, 2013.
- [34] Akshaya K. Samal, Lakshminarayana Polavarapu, Sergio Rodal-Cedeira, Luis M. Liz-Marzán, Jorge Pérez-Juste, and Isabel Pastoriza-Santos. Size tunable Au@Ag core-shell nanoparticles: synthesis and surface-enhanced Raman scattering properties. *Langmuir*, 29(48):15076–15082, 2013. PMID: 24261458.
- [35] Ian Freestone, Nigel Meeks, Margaret Sax, and Catherine Higgitt. The lycurgus cup-a roman nanotechnology. 40:270–277, 12 2007.
- [36] M. Faraday. The Bakerian Lecture: Experimental Relations of Gold (and Other Metals) to Light. *Philosophical Transactions of the Royal Society of London Series I*, 147:145–181, 1857.
- [37] Neil Savage. Trick of the light- invisibly small particles of gold can be used to manipulate the properties of light. *Nature*, 495(7440):S8–S9, 2013.
- [38] Dror Sarid and William Challener. *Modern Introduction to surface plasmons: theory, mathematical modeling, and applications*. Cambridge University press, The Edinburgh Building, Cambridge, 2010.

- [39] S. A. Maier. *Plasmonics: fundamentals and applications*. Springer Science+Business Media LLC, 2007.
- [40] Gregory V. Hartland. Optical studies of dynamics in noble metal nanostructures. *Chemical Reviews*, 111(6):3858–3887, 2011. PMID: 21434614.
- [41] E. Hutter and J.H. Fendler. Exploitation of localized surface plasmon resonance. *Advanced Materials*, 16(19):1685–1706, 2004.
- [42] Mark I. Stockman. Nanoplasmonics: The physics behind the applications. *Physics Today*, 64(2), 2011.
- [43] Suljo Linic, Phillip Christopher, and David B. Ingram. Plasmonic-metal nanostructures for efficient conversion of solar to chemical energy. *Nat Mater*, 10(12):911–921, 2011.
- [44] Viktor Myroshnychenko, Jessica Rodriguez-Fernandez, Isabel Pastoriza-Santos, Alison M. Funston, Carolina Novo, Paul Mulvaney, Luis M. Liz-Marzan, and F. Javier Garcia de Abajo. Modelling the optical response of gold nanoparticles. *Chem. Soc. Rev.*, 37:1792–1805, 2008.
- [45] Shinji Hayashi and Takayuki Okamoto. Plasmonics: visit the past to know the future. *Journal of Physics D: Applied Physics*, 45(43), 2012.
- [46] Sarah Unser, Ian Bruzas, Jie He, and Laura Sagle. Localized surface plasmon resonance biosensing: Current challenges and approaches. 15 (7):15684–15716, Jul 2015.
- [47] Younan Xia and Naomi J. Halas. Shape-controlled synthesis and surface plasmonic properties of metallic nanostructures. *MRS Bulletin*, 30(5):338â348, 2005.
- [48] John David Jackson. *Klassische Elektrodynamik (Classical Electrodynamics)*. Walter de Gruyter GmbH Co. KG, Berlin, 2006. Fourth Edition (German), translated by Prof. Kurt Müller, edited by Christopher Witte.
- [49] Xiaohua Huang and Mostafa A. El-Sayed. Gold nanoparticles: Optical properties and implementations in cancer diagnosis and photothermal therapy. *Journal of Advanced Research*, 1(1):13 – 28, 2010.
- [50] Gustav Mie. Beiträge zur Optik trüber Medien, speziell kolloidaler Metallösungen. *Annalen der Physik*, 330(3):377–445, 1908.
- [51] Jon A. Schuller, Edward S. Barnard, Wenshan Cai, Young Chul Jun, Justin S. White, and Mark L. Brongersma. Plasmonics for extreme light concentration and manipulation. *Nat Mater*, 9(3):193–204, 2010.
- [52] A. Trügler. *Optical properties of metallic nanoparticles*. PhD thesis, Institut für Physik, Fachbereich Theoretische Physik, Karl-Franzens-Universität Graz, 2011.
- [53] Jian Zhu. Surface plasmon resonance from bimetallic interface in Au–Ag core–shell structure nanowires. *Nanoscale Research Letters*, 4(9):977, 2009.
- [54] Yong Yang, Jianlin Shi, Go Kawamura, and Masayuki Nogami. Preparation of Au-Ag, Ag-Au core-shell bimetallic nanoparticles for surface-enhanced Raman scattering. *Scripta Materialia*, 58(10):862 – 865, 2008.
- [55] Furong Tian, Franck Bonnier, Alan Casey, Anne Shanahan, and Hugh Byrne. Surface enhanced Raman scattering with gold nanoparticles: Effect of particle shape. 6, 10 2014.

- [56] Adam B. Taylor and Peter Zijlstra. Single-molecule plasmon sensing: Current status and future prospects. *ACS Sensors*, 2(8):1103–1122, 2017. PMID: 28762723.
- [57] Toshihiro Nakamura and Shinji Hayashi. Enhancement of dye fluorescence by gold nanoparticles: Analysis of particle size dependence. *Japanese Journal of Applied Physics*, 44(9R):6833, 2005.
- [58] Ronghua Lu, Ling Xu, Zhaoyun Ge, Rui Li, Jun Xu, Linwei Yu, and Kunji Chen. Improved efficiency of silicon nanoholes/gold nanoparticles/organic hybrid solar cells via localized surface plasmon resonance. *Nanoscale Research Letters*, 11(1):160, Mar 2016.
- [59] Srivalleesha Mallidi, Timothy Larson, Justina Tam, Pratixa P. Joshi, Andrei Karpiouk, Konstantin Sokolov, and Stanislav Emelianov. Multiwavelength photoacoustic imaging and plasmon resonance coupling of gold nanoparticles for selective detection of cancer. *Nano Letters*, 9(8):2825–2831, 2009. PMID: 19572747.
- [60] Zuwei Liu, Wenbo Hou, Prathamesh Pavaskar, Mehmet Aykol, and Stephen B. Cronin. Plasmon resonant enhancement of photocatalytic water splitting under visible illumination. *Nano Letters*, 11(3):1111–1116, 2011. PMID: 21319840.
- [61] Xiang-Chao Ma, Ying Dai, Lin Yu, and Bai-Biao Huang. Energy transfer in plasmonic photocatalytic composites. *Light Sci Appl*, 5:e16017, 2016.
- [62] Cesar Clavero. Plasmon-induced hot-electron generation at nanoparticle/metal-oxide interfaces for photovoltaic and photocatalytic devices. *Nat Photon*, 8(2):95–103, 2014.
- [63] Akihiro Furube, Luchao Du, Kohjiro Hara, Ryuzi Katoh, and Masanori Tachiya. Ultrafast plasmon-induced electron transfer from gold nanodots into TiO<sub>2</sub> nanoparticles. *Journal of the American Chemical Society*, 129(48):14852–14853, 2007. PMID: 17994750.
- [64] Syed Mubeen, Gerardo Hernandez-Sosa, Daniel Moses, Joun Lee, and Martin Moskovits. Plasmonic photosensitization of a wide band gap semiconductor: Converting plasmons to charge carriers. *Nano Letters*, 11(12):5548–5552, 2011. PMID: 22040462.
- [65] Wenbo Hou and Stephen B. Cronin. A review of surface plasmon resonance-enhanced photocatalysis. *Advanced Functional Materials*, 23(13):1612–1619, 2013.
- [66] Ying-Chih Pu and Jin Z Zhang. Mechanisms behind plasmonic enhancement of photocurrent in metal oxides. *Austin J Nanomed Nanotechnol.*, 2(5), 2014.
- [67] Yucheng Lan, Yalin Lu, and Zhifeng Ren. Mini review on photocatalysis of titanium dioxide nanoparticles and their solar applications. *Nano Energy*, 2(5):1031 – 1045, 2013.
- [68] Dorian A. H. Hanaor and Charles C. Sorrell. Review of the anatase to rutile phase transformation. *Journal of Materials Science*, 46(4):855–874, 2011.
- [69] Roel van de Krol. *Photoelectrochemical Hydrogen Production*, volume 102 of *Electronic Materials: Science Technology*, chapter 2: Principles of Photoelectrochemical Cells. Springer US, 2012.
- [70] Ming X. Tan, Paul E Laibinis, Sonbinh T. Nguyen, Janet M. Kesselman, Colby E. Stanton, and Nathan S. Lewis. *Principles and Applications of Semiconductor Photoelectrochemistry*, pages 21–144. John Wiley Sons, Inc., 2007.

- [71] David O. Scanlon, Charles W. Dunnill, John Buckeridge, Stephen A. Shevlin, Andrew J. Logsdail, Scott M. Woodley, C. Richard A. Catlow, Michael J. Powell, Robert G. Palgrave, Ivan P. Parkin, Graeme W. Watson, Thomas W. Keal, Paul Sherwood, Aron Walsh, and Alexey A. Sokol. Band alignment of rutile and anatase  $\text{TiO}_2$ . *Nat Mater*, 12(9):798–801, 2013.
- [72] Kazuhito Hashimoto, Hiroshi Irie, and Akira Fujishima.  $\text{TiO}_2$  photocatalysis: A historical overview and future prospects. *Japanese Journal of Applied Physics*, 44(12R):8269, 2005.
- [73] Joop Schoonman and Roel van de Krol. Nanostructured materials for solar hydrogen production. *U. P. B. Sci. Bull*, 73, 2011.
- [74] N.W. Ashcroft and N.D. Mermin. *Festkörperphysik*. Oldenbourg, 2001.
- [75] A. V. Andrade-Neto. Dielectric function for free electron gas: comparison between Drude and Lindhard models. *Revista Brasileira de Ensino de Física*, 39, 00 2017.
- [76] Anastasiya Derkachova, Krystyna Kolwas, and Iraida Demchenko. Dielectric function for gold in plasmonics applications: Size dependence of plasmon resonance frequencies and damping rates for nanospheres. *Plasmonics*, 11(3):941–951, Jun 2016.
- [77] L. Catherine and P. Olivier. *Gold Nanoparticles For Physics, Chemistry And Biology (Second Edition)*. World Scientific Publishing Company, 2017.
- [78] M. Concepción Gimeno. *The Chemistry of Gold*, pages 1–63. Wiley-VCH Verlag GmbH Co. KGaA, 2009.
- [79] C. Caro, P. M. Castillo, R. Klippstein, D. Pozo, and A. P. Zaderenko. *Silver nanoparticles: sensing and imaging applications*. InTech, 2010.
- [80] Donald A. Gurnett and Amitava Bhattacharjee. *Introduction to Plasma Physics-with Space and Laboratory Applications*. Cambridge University Press, United Kingdom, 2005.
- [81] Lewi Tonks and Irving Langmuir. Oscillations in ionized gases. *Phys. Rev.*, 33:195–210, Feb 1929.
- [82] Alfred Grill. *Cold Plasma in Materials Fabrication-From Fundamentals to Applications*. IEEE Pres, New York, 1994.
- [83] M.-B. Kallenrode. *Space Physics: An Introduction to Plasmas and Particles in the Heliosphere and Magnetospheres*. Springer Verlag, 2004.
- [84] W. H. Kegel. *Plasmaphysik- eine Einführung*. Springer-Verlag Berlin Heidelberg, 1998.
- [85] Raymond Constantin and Baham Miremad. Performance of hard coatings, made by balanced and unbalanced magnetron sputtering, for decorative applications. *Surface and Coatings Technology*, 120&121:728 – 733, 1999.
- [86] E Budke, J Krempel-Hesse, H Maidhof, and H Schüssler. Decorative hard coatings with improved corrosion resistance. *Surface and Coatings Technology*, 112(1&3):108 – 113, 1999.
- [87] Sam Zhang, Xuan Lam Bui, and Yongqing Fu. Magnetron sputtered hard a-C coatings of very high toughness. *Surface and Coatings Technology*, 167(2-3):137 – 142, 2003. Proceedings of the Symposium on Technological Advances and Performance of Engineering Thin Films and Surface Coatings at the 1st International Conference on Materials Processing for Properties and Performance (MP3).

- [88] D. Dinesh Kumar, N. Kumar, S. Kalaiselvam, R. Radhika, S. Dash, A. K. Tyagi, and R. Jayavel. Reactive magnetron sputtered wear resistant multilayer transition metal carbide coatings: microstructure and tribo-mechanical properties. *RSC Adv.*, 5:81790–81801, 2015.
- [89] J. Morales-Hernández, A. Mandujano-Ruíz, J. Torres-González, F. J. Espinoza-Beltrán, and H Herrera-Hernández. Low friction coefficient coatings Ni-Cr by magnetron sputtering, DC. *Revista de Metalurgia*, 51, 2015.
- [90] Yongjian Zhang, Zhengtang Liu, Duyang Zang, Liping Feng, Xingsen Che, and Yanyan Li. Optical and electrical properties of magnetron sputtering deposited Cu-Al-O thin films. *International Journal of Antennas and Propagation*, 2012:7, 2012.
- [91] Edgar Alfonso, Jairo Olaya, and G Cubillos. Thin film growth through sputtering technique and its applications. 09 2012.
- [92] S Swann. Magnetron sputtering. *Physics in Technology*, 19(2):67, 1988.
- [93] Roman Surmenev, Alina Vladescu, Maria Surmeneva, Anna Ivanova, Mariana Braic, Irina Grubova, and Cosmin Mihai Cotrut. Radio frequency magnetron sputter deposition as a tool for surface modification of medical implants. In Nikolay N. Nikitenkov, editor, *Modern Technologies for Creating the Thin-film Systems and Coatings*, chapter 12. InTech, Rijeka, 2017.
- [94] P.J Kelly and R.D Arnell. Magnetron sputtering: a review of recent developments and applications. *Vacuum*, 56(3):159 – 172, 2000.
- [95] T E. Sheridan, Matthew Goeckner, and John Goree. Electron velocity distribution functions in a sputtering magnetron discharge for the EXB direction. 16:2173 – 2176, 08 1998.
- [96] Donald L. Smith. *Thin-film deposition: principles and practice*. McGraw-Hill, 1995.
- [97] Y. B. Gaididei, V. M. Loktev, A. G. Naumovets, and A. G. Zagorodny. Adatom interaction effects in surface diffusion. *CondensedMatterPhysics*, 16(1), 2013.
- [98] F F Leal, Silvio C. Ferreira, and Sukarno O. Ferreira. Modelling of epitaxial film growth with an Ehrlich-Schwoebel barrier dependent on the step height. *Journal of Physics: Condensed Matter*, 23(29):292201, 2011.
- [99] K Reichelt. Nucleation and growth of thin films. *Vacuum*, 38(12):1083 – 1099, 1988.
- [100] I. Petrov, P. B. Barna, L. Hultman, and J. E. Greene. Microstructural evolution during film growth. *Journal of Vacuum Science & Technology A: Vacuum, Surfaces, and Films*, 21(5):S117–S128, 2003.
- [101] C. V. Thompson. Structure evolution during processing of polycrystalline films. *Annual Review of Materials Science*, 30(1):159–190, 2000.
- [102] J A Venables, G D T Spiller, and M Hanbucken. Nucleation and growth of thin films. *Reports on Progress in Physics*, 47(4):399, 1984.
- [103] Marcia H. Grabow and George H. Gilmer. Thin film growth modes, wetting and cluster nucleation. *Surface Science*, 194(3):333 – 346, 1988.
- [104] D. Magnfält. *Fundamental processes in thin film growth-The origin of compressive stress and the dynamics of the early growth stages*. PhD thesis, Linkoping Universit, Institute of Technology, 2014.

- [105] R Esterina. *Solid-state dewetting of magnetic binary alloy thin films and application as nanowire and nanotube growth catalysts*. PhD thesis, national university of Singapore, 2014.
- [106] R. V. Zucker. *Capillary-Driven Shape Evolution in Solid-State Micro- and Nano-Scale Systems*. PhD thesis, Massachusetts Institute of Technology, 2015.
- [107] J. Ye. *Solid-state Dewetting of Continuous and Patterned Single Crystal Ni Thin Films*. PhD thesis, Massachusetts Institute of Technology, 2011.
- [108] Anna Schaub, Petr Slepíčka, Irena Kašpárková, Petr Malinský, Anna Macková, and Václav Švorčík. Gold nanolayer and nanocluster coatings induced by heat treatment and evaporation technique. *Nanoscale Research Letters*, 8(1):249, 2013.
- [109] B. Ballarin, M. C. Cassani, C. Maccato, and A. Gasparotto. Rf-sputtering preparation of gold-nanoparticle-modified ITO electrodes for electrocatalytic applications. *Nanotechnology*, 22(27), 2011.
- [110] Wenjuan Chen, Yuhua Lu, Wen Dong, Zhuo Chen, and Mingrong Shen. Plasmon mediated visible light photocurrent and photoelectrochemical hydrogen generation using Au nanoparticles/TiO<sub>2</sub> electrode. *Materials Research Bulletin*, 50:31 – 35, 2014.
- [111] Lei Zhang, Frederic Cosandey, Rajendra Persaud, and Theodore E. Madey. Initial growth and morphology of thin Au films on TiO<sub>2</sub>(110). *Surface Science*, 439(1-3):73–85, 1999.
- [112] Y. Q. Wang, W. S. Liang, and C. Y. Geng. Shape evolution of gold nanoparticles. *Journal of Nanoparticle Research*, 12(2):655–661, 2010.
- [113] N Naseri, M Amiri, and A Z Moshfegh. Visible photoenhanced current-voltage characteristics of Au:TiO<sub>2</sub> nanocomposite thin films as photoanodes. *Journal of Physics D: Applied Physics*, 43(10):105405, 2010.
- [114] Marta Haro, Rafael Abargues, Isaac Herraiz-Cardona, Juan Martínez-Pastor, and Sixto Giménez. Plasmonic versus catalytic effect of gold nanoparticles on mesoporous TiO<sub>2</sub> electrodes for water splitting. *Electrochimica Acta*, 144:64 – 70, 2014.
- [115] K. Lance Kelly, Eduardo Coronado, Lin Lin Zhao, and George C. Schatz. The optical properties of metal nanoparticles: the influence of size, shape, and dielectric environment. *The Journal of Physical Chemistry B*, 107(3):668–677, 2003.
- [116] Jianfeng Huang, Sascha Vongehr, Shaochun Tang, Haiming Lu, Jiancang Shen, and Xiangkang Meng. Ag dendrite-based Au/Ag bimetallic nanostructures with strongly enhanced catalytic activity. *Langmuir*, 25(19):11890–11896, 2009. PMID: 19788231.
- [117] Wolfgang Haiss, Nguyen T. K. Thanh, Jenny Aveyard, and David G. Fernig. Determination of size and concentration of gold nanoparticles from uv-vis spectra. *Analytical Chemistry*, 79(11):4215–4221, 2007. PMID: 17458937.
- [118] Somaye Baset, Hossein Akbari, Hossein Zeynali, and Morteza Shafie. Size measurement of metal and semiconductor nanoparticles via UV-vis absorption spectra. *Digest Journal of Nanomaterials and Biostructures*, 6(2):709–716, 2011.
- [119] Sheng Peng, Jeffrey M. McMahon, George C. Schatz, Stephen K. Gray, and Yugang Sun. Reversing the size-dependence of surface plasmon resonances. *Proceedings of the National Academy of Sciences of the United States of America*, 107(33):14530–14534, 2010.



- [120] Shigehito Deki, Yoshifumi Aoi, Hiroshi Yanagimoto, Katsuyuki Ishii, Kensuke Akamatsu, Minoru Mizuhata, and Akihiko Kajinami. Preparation and characterization of Au-dispersed TiO<sub>2</sub> thin films by a liquid-phase deposition method. *J. Mater. Chem.*, 6:1879–1882, 1996.
- [121] D. Buso, J. Pacifico, A. Martucci, and P. Mulvaney. Gold-nanoparticle-doped TiO<sub>2</sub> semiconductor thin films: optical characterization. *Advanced Functional Materials*, 17(3):347–354, 2007.
- [122] Enrico Della Gaspera, Alessandro Antonello, Massimo Guglielmi, Michael L. Post, Valentina Bello, Giovanni Mattei, Filippo Romanato, and Alessandro Martucci. Colloidal approach to Au-loaded TiO<sub>2</sub> thin films with optimized optical sensing properties. *J. Mater. Chem.*, 21:4293–4300, 2011.
- [123] Inga Bannat, Katrin Wessels, Torsten Oekermann, Jiri Rathousky, Detlef Bahnemann, and Michael Wark. Improving the photocatalytic performance of mesoporous titania films by modification with gold nanostructures. *Chemistry of Materials*, 21(8):1645–1653, 2009.
- [124] Matthew S. Shore, Junwei Wang, Aaron C. Johnston-Peck, Amy L. Oldenburg, and Joseph B. Tracy. Synthesis of Au(core)/Ag(shell) nanoparticles and their conversion to AuAg alloy nanoparticles. *Small*, 7(2):230–234, 2011.
- [125] Edit Csapó, Albert Oszkó, Erika Varga, Ádám Juhász, Norbert Buzás, and László Kőr. Synthesis and characterization of Ag/Au alloy and core(Ag)-shell(Au) nanoparticles. *Colloids and Surfaces A: Physicochemical and Engineering Aspects*, 415:281 – 287, 2012.
- [126] Jiajia Deng, Jian Du, Ye Wang, Yifeng Tu, and Junwei Di. Synthesis of ultrathin silver shell on gold core for reducing substrate effect of LSPR sensor. *Electrochemistry Communications*, 13(12):1517 – 1520, 2011.
- [127] Masaharu Tsuji, Ryoichi Matsuo, Peng Jiang, Nobuhiro Miyamae, Daisuke Ueyama, Michiko Nishio, Sachie Hikino, Hisayo Kumagae, Khairul Sozana Nor Kamarudin, and Xin-Ling Tang. Shape-dependent evolution of Au@Ag core-shell nanocrystals by PVP-assisted N,N-dimethylformamide reduction. *Crystal Growth & Design*, 8(7):2528–2536, 2008.
- [128] Krishna Kanta Halder, Simanta Kundu, and Amitava Patra. Core-size-dependent catalytic properties of bimetallic Au/Ag core-shell nanoparticles. *ACS Applied Materials & Interfaces*, 6(24):21946–21953, 2014. PMID: 25456348.
- [129] Yanyun Ma, Weiyang Li, Eun Chul Cho, Zhiyuan Li, Taekyung Yu, Jie Zeng, Zhaoxiong Xie, and Younan Xia. Au@Ag core-shell nanocubes with finely tuned and well-controlled sizes, shell thicknesses, and optical properties. *ACS Nano*, 4(11):6725–6734, 2010. PMID: 20964400.
- [130] F. Pincella, K. Isozaki, and K. Miki. A visible light-driven plasmonic photocatalyst. *Light: Science Applications*, 3, 2014.
- [131] Tingting Bai, Jianfei Sun, Renchao Che, Lina Xu, Chenyue Yin, Zhirui Guo, and Ning Gu. Controllable preparation of core-shell Au-Ag nanoshuttles with improved refractive index sensitivity and SERS activity. *ACS Applied Materials & Interfaces*, 6(5):3331–3340, 2014. PMID: 24533919.
- [132] A V Abakshonok, A Yu Panarin, V E Agabekov, A N Eryomin, and S N Terekhov. Synthesis of (Au)Ag core-shell nanocomposite in the water- ethanol mixture and its optical properties. *IOP Conference Series: Materials Science and Engineering*, 64(1):012038, 2014.

- [133] I. A. Tiunov, M. V. Gorbachevskyy, D. S. Kopitsyn, M. S. Kotelev, E. V. Ivanov, V. A. Vinokurov, and A. A. Novikov. Synthesis of large uniform gold and core-shell gold-silver nanoparticles: Effect of temperature control. *Russian Journal of Physical Chemistry A*, 90(1):152–157, Jan 2016.
- [134] Lu Lu, Gwendolyn Burkey, Ionel Halaciuga, and Dan V. Goia. Core-shell gold/silver nanoparticles: Synthesis and optical properties. *Journal of Colloid and Interface Science*, 392:90 – 95, 2013.
- [135] Lehui Lu, Haishui Wang, Yonghui Zhou, Shiquan Xi, Hongjie Zhang, Jiawen Hu, and Bing Zhao. Seed-mediated growth of large, monodisperse core-shell gold-silver nanoparticles with Ag-like optical properties. *Chem. Commun.*, pages 144–145, 2002.
- [136] Yan Wu, Peng Jiang, Ming Jiang, Tie-Wei Wang, Chuanfei Guo, Si-Shen Xie, and Zhong Wang. The shape evolution of gold seeds and gold@silver core-shell nanostructures. 20:305602, 08 2009.
- [137] A Calagua, Hugo Alarcón, F Paraguay, and Juan Rodríguez. Synthesis and characterization of bimetallic gold-silver core-shell nanoparticles: a green approach. 04:116–121, 01 2015.
- [138] Masaharu Tsuji, Nobuhiro Miyamae, Seongyop Lim, Kousuke Kimura, Xu Zhang, Sachie Hikino, and Michiko Nishio. Crystal structures and growth mechanisms of Au@Ag core-shell nanoparticles prepared by the microwave-polyol method. *Crystal Growth & Design*, 6(8):1801–1807, 2006.
- [139] Cheshta Shankar, Anh T N Dao, Prerna Singh, Koichi Higashimine, Derrick M Mott, and Shinya Maenosono. Chemical stabilization of gold coated by silver core-shell nanoparticles via electron transfer. *Nanotechnology*, 23(24):245704, 2012.
- [140] Chao Wang, Sheng Peng, Ryan Chan, and Shouheng Sun. Synthesis of AuAg alloy nanoparticles from core/shell-structured Ag/Au. *Small*, 5(5):567–570, 2009.
- [141] Ronei Miotto, Luiz De melo dos santos, Ferenc Kiss, and Armando Ferraz. Structural and energetic properties of Au@Ag and Ag@Au core-shell nanoparticles. 10 2014.
- [142] R.C. Adochite, D. Munteanu, M. Torrell, L. Cunha, E. Alves, N.P. Barradas, A. Cavaleiro, J.P. Riviere, E. Le Bourhis, D. Eyidi, and F. Vaz. The influence of annealing treatments on the properties of Ag:TiO<sub>2</sub> nanocomposite films prepared by magnetron sputtering. *Applied Surface Science*, 258(8):4028 – 4034, 2012.
- [143] V. M. Renteria-Tapia, G. Valverde-Aguilar, and J. A. Garcia-Macedo. *Plasmonics: Metallic Nanostructures and Their Optical Properties*, chapter Synthesis, optical properties and modelling of silver core-silver oxide shell nanostructures in silica films. Proc. Of SPIE, 2007.
- [144] M. Banerjee, S. Sharma, A. Chattopadhyay, and S. S. Ghosh. Enhanced antibacterial activity of bimetallic gold-silver core-shell nanoparticles at low silver concentration. *Nanoscale*, 2011.
- [145] Jian Zhu, Fan Zhang, Jian-Jun Li, and Jun-Wu Zhao. The effect of nonhomogeneous silver coating on the plasmonic absorption of Au-Ag core-shell nanorod. *Gold Bulletin*, 47(1):47–55, 2014.
- [146] S. Link, Z. L. Wang, and M. A. El-Sayed. Alloy formation of gold-silver nanoparticles and the dependence of the plasmon absorption on their composition. *The Journal of Physical Chemistry B*, 103(18):3529–3533, 1999.

- [147] Davide Barreca, Alberto Gasparotto, Cinzia Maragno, Eugenio Tondello, and Stefano Gialanella. Structure and optical properties of silica-supported AgAu nanoparticles. *Journal of Nanoscience and Nanotechnology*, 7(7):2480–2486, 2007.
- [148] Yang Tian and Tetsu Tatsuma. Plasmon-induced photoelectrochemistry at metal nanoparticles supported on nanoporous TiO<sub>2</sub>. *Chem. Commun.*, pages 1810–1811, 2004.
- [149] Yang Tian and Tetsu Tatsuma. Mechanisms and applications of plasmon-induced charge separation at TiO<sub>2</sub> films loaded with gold nanoparticles. *Journal of the American Chemical Society*, 127(20):7632–7637, 2005. PMID: 15898815.
- [150] Gaoling Zhao, Hiromitsu Kozuka, and Toshinobu Yoko. Sol-gel preparation and photoelectrochemical properties of TiO<sub>2</sub> films containing Au and Ag metal particles. *Thin Solid Films*, 277(1):147 – 154, 1996.
- [151] S.K. Jana, T. Majumder, and S. Banerjee. Enhanced photoelectrochemical property of gold nanoparticle sensitized TiO<sub>2</sub> nanotube: A crucial investigation at electrode-electrolyte interface. *Journal of Electroanalytical Chemistry*, 727:99 – 103, 2014.
- [152] Kefeng Yu, Yang Tian, and Tetsu Tatsuma. Size effects of gold nanoparticles on plasmon-induced photocurrents of gold-TiO<sub>2</sub> nanocomposites. *Phys. Chem. Chem. Phys.*, 8:5417–5420, 2006.
- [153] Xu Wu, Anthony Centeno, Xuemei Zhang, Daniel Darvill, Mary P. Ryan, D. Jason Riley, Neil M. Alford, and Fang Xie. Broadband plasmon photocurrent generation from Au nanoparticles/ mesoporous TiO<sub>2</sub> nanotube electrodes. *Solar Energy Materials and Solar Cells*, 138:80 – 85, 2015.
- [154] Martin Moskovits. Hot electrons cross boundaries. *Science*, 332(6030):676–677, 2011.
- [155] Furui Tan, Tenghao Li, Ning Wang, Sin Ki Lai, Chi Chung Tsoi, Weixing Yu, and Xuming Zhang. Rough gold films as broadband absorbers for plasmonic enhancement of TiO<sub>2</sub> photocurrent over 400-800nm. *Scientific Reports*, 6:33049, 2016.
- [156] Yongkun Li, Hongmei Yu, Changkun Zhang, Li Fu, Guangfu Li, Zhigang Shao, and Baolian Yi. Enhancement of photoelectrochemical response by Au modified in TiO<sub>2</sub> nanorods. *International Journal of Hydrogen Energy*, 38(29):13023 – 13030, 2013.
- [157] Mohammad Mansoob Khan, Sajid Ali Ansari, Jintae Lee, and Moo Hwan Cho. Enhanced optical, visible light catalytic and electrochemical properties of Au@TiO<sub>2</sub> nanocomposites. *Journal of Industrial and Engineering Chemistry*, 19(6):1845 – 1850, 2013.
- [158] Deepa Jose, Christopher M. Sorensen, Sadhana S. Rayalu, Khadga M. Shrestha, and Kenneth J. Klabunde. Au-TiO<sub>2</sub> nanocomposites and efficient photocatalytic hydrogen production under UV-visible and visible light illuminations: A comparison of different crystalline forms of TiO<sub>2</sub>. *International Journal of Photoenergy*, 2013:10, 2013.
- [159] G. Kenanakis, D. Vernardou, A. Dalamagkas, and N. Katsarakis. Photocatalytic and electrooxidation properties of TiO<sub>2</sub> thin films deposited by sol-gel. *Catalysis Today*, 240, Part A:146 – 152, 2015. Environmental Applications of Advanced Oxidation Processes â {EAAOP3}.
- [160] Paramaconi Rodriguez, Daniela Plana, David J. Fermin, and Marc T.M. Koper. New insights into the catalytic activity of gold nanoparticles for CO oxidation in electrochemical media. *Journal of Catalysis*, 311:182 – 189, 2014.

- [161] Muhammad Hussain, Mashkoo Ahmad, Amjad Nisar, Hongyu Sun, Shafqat Karim, Maaz Khan, Sabih D. Khan, Munawar Iqbal, and Syed Zahid Hussain. Enhanced photocatalytic and electrochemical properties of Au nanoparticles supported TiO<sub>2</sub> microspheres. *New J. Chem.*, 38:1424–1432, 2014.
- [162] Angela Kruth, Sandra Peglow, Antje Quade, Marga-Martina Pohl, Rüdiger Foest, Volker Brüser, and Klaus-Dieter Weltmann. Structural and photoelectrochemical properties of DC magnetron-sputtered TiO<sub>2</sub> layers on FTO. *The Journal of Physical Chemistry C*, 118(43):25234–25244, 2014.
- [163] M. Vergöhl, H. Althues, P. Frach, D. Göß, T. Graumann, C. Hübner, F. Neumann, T. Neubert, G. Schottner, and D. K. Song. Measurement of the photocatalytic activity of TiO<sub>2</sub> films deposited by different methods. *8th International Conference on Coatings on Glass and Plastics, ICCG 2010. Advanced Coatings for Large Area or High-Volume Products. Proceedings*, 2010. conference paper, International Conference on Coatings on Glass and Plastics (ICCG) 8, 2010, Braunschweig.
- [164] Thomas Abendroth, Holger Althues, Stefan Kaskel, and Ines Dani. Verfahren zur Herstellung photokatalytisch aktiver Titandioxidschichten. (DE102008052098 B4), 2013.
- [165] Heinz-Helmut Perkampus. *UV-VIS Spectroscopy and its Applications*. Springer-Verlag, 1992.
- [166] W. Gottwald and Heinrich K. H. *UV/VIS-Spektroskopie für Anwender*. Wiley-VCH, 1998.
- [167] T. Burns. *UV spectroscopy : techniques, instrumentation, data handling*, chapter Principles of spectrophotometric measurements with particular reference to the UV-visible region. London ; New York : Chapman Hall, 1993.
- [168] PerkinElmer. Tutorial Highendmessung mit Kugel. *V1.0.doc*, 20.08.2012.
- [169] Jeol Advanced Technology. *SEM Scanning Electron Microscope A To Z-Basic Knowledge for using the SEM*.
- [170] P. J. Goodhew and J. Humphreys, F. *Elektronenmikroskopie: Grundlagen und Anwendung*. McGraw-Hill Book Company (UK) Limited, Maidenhead, 1991.
- [171] D. B. Williams and C. B. Carter. *Transmission Electron Microscopy: a textbook for materials science*. Plenum Press, New York, 1996.
- [172] K.D. Vernon-Parry. Scanning electron microscopy: an introduction. *III-Vs Review*, 13(4):40 – 44, 2000.
- [173] Christina Scheu and Wayne D. Kaplan. *Introduction to Scanning Electron Microscopy*, pages 1–37. Wiley-VCH Verlag GmbH Co. KGaA, 2012.
- [174] S. L. Flegler, J. W. Heckman, and K. L. Klomparens. *Elektronenmikroskopie: Grundlagen-Methoden-Anwendungen*. Spektrum Akademischer Verlag, 1995.
- [175] Peter Hawkes and John C. Spence. Science of microscopy. -1, 01 2007.
- [176] B. Fultz and J. M. Howe. *Transmission Electron Microscopy and Diffractometry of Materials*. Springer, 2013.
- [177] D. Vollath. *Nanowerkstoffe für Einsteiger*. Wiley-VCH, Weinheim, 2014.

- [178] J Brentano. Focussing method of crystal powder analysis by x-rays. *Proceedings of the Physical Society of London*, 37(1):184, 1924.
- [179] R. W. Cahn, P. Haasen, and E. J. Kramer, editors. *Materials Science and Technology: A comprehensive treatment*, Weinheim, 1992. VCH.
- [180] Roel van de Krol. *Photoelectrochemical Hydrogen Production*, volume 102 of *Electronic Materials: Science Technology*, chapter 3: Photoelectrochemical Measurements. Springer US, 2012.
- [181] Wenhua Luo, Kalin Su, Kemin Li, Gaohua Liao, Nengwen Hu, and Ming Jia. Substrate effect on the melting temperature of gold nanoparticles. *The Journal of Chemical Physics*, 136(23):234704, 2012.
- [182] Marek Grzelczak, Jorge Perez-Juste, Paul Mulvaney, and Luis M. Liz-Marzan. Shape control in gold nanoparticle synthesis. *Chem. Soc. Rev.*, 37:1783–1791, 2008.
- [183] Hong Wei and Hongxing Xu. Hot spots in different metal nanostructures for plasmon-enhanced raman spectroscopy. *Nanoscale*, 5:10794–10805, 2013.
- [184] Kandasamy Palanivelu, Ji-Sun Im, and Young-Seak Lee. Carbon doping of TiO<sub>2</sub> for visible light photo catalysis - a review. *Carbon Science*, 8(3), 2007.
- [185] Yi Ma, Xiuli Wang, Yushuai Jia, Xiaobo Chen, Hongxian Han, and Can Li. Titanium dioxide-based nanomaterials for photocatalytic fuel generations. *Chemical Reviews*, 114(19):9987–10043, 2014. PMID: 25098384.
- [186] Jie Cao, Tong Sun, and Kenneth T.V. Grattan. Gold nanorod-based localized surface plasmon resonance biosensors: A review. *Sensors and Actuators B: Chemical*, 195(Supplement C):332 – 351, 2014.
- [187] Agnieszka Zuber, Malcolm Purdey, Erik Schartner, Caroline Forbes, Benjamin van der Hoek, David Giles, Andrew Abell, Tanya Monro, and Heike Ebendorff-Heidepriem. Detection of gold nanoparticles with different sizes using absorption and fluorescence based method. *Sensors and Actuators B: Chemical*, 227:117 – 127, 2016.
- [188] M A Garcia. Surface plasmons in metallic nanoparticles: fundamentals and applications. *Journal of Physics D: Applied Physics*, 44(28):283001, 2011.
- [189] Shakil Khan, Muhammad Shahid, A. Mahmood, A. Shah, Ishaq Ahmed, Mazhar Mehmood, U. Aziz, Q. Raza, and M. Alam. Texture of the nano-crystalline AlN thin films and the growth conditions in DC magnetron sputtering. *Progress in Natural Science: Materials International*, 25(4):282 – 290, 2015.
- [190] Pravin S. Shinde, Alagappan Annamalai, Ju Hun Kim, Sun Hee Choi, Jae Sung Lee, and Jum Suk Jang. Photoelectrochemical, impedance and optical data for self Sn-diffusion doped Fe<sub>2</sub>O<sub>3</sub> photoanodes fabricated at high temperature by one and two-step annealing methods. *Data in Brief*, 5(Supplement C):796 – 804, 2015.
- [191] Marco Altomare, Nhat Truong Nguyen, and Patrik Schmuki. Templated dewetting: designing entirely self-organized platforms for photocatalysis. *Chem. Sci.*, 7:6865, 2016.
- [192] G.G. Paulson and A.L. Friedberg. Coalescence and agglomeration of gold films. *Thin Solid Films*, 5(1):47 – 52, 1970.

- [193] Jongpil Ye. Fabrication of ordered arrays of micro- and nanoscale features with control over their shape and size via templated solid-state dewetting. *Scientific Reports*, 5:9823, 2015.
- [194] Tanya Karakouz, Alexander B. Tesler, Takumi Sannomiya, Yishay Feldman, Alexander Vaskevich, and Israel Rubinstein. Mechanism of morphology transformation during annealing of nanostructured gold films on glass. *Phys. Chem. Chem. Phys.*, 15:4656–4665, 2013.
- [195] Mikhael Bechelany, Xavier Maeder, Jessica Riesterer, Jihane Hankache, Damiana Lerose, Silke Christiansen, Johann Michler, and Laetitia Philippe. Synthesis mechanisms of organized gold nanoparticles: Influence of annealing temperature and atmosphere. *Crystal Growth & Design*, 10(2):587–596, 2010.
- [196] Amit Bansal, Jagmeet Singh Sekhon, and S. S. Verma. Scattering efficiency and lspr tunability of bimetallic Ag, Au, and Cu nanoparticles. *Plasmonics*, 9(1):143–150, Feb 2014.
- [197] M. P. Navas and R. K. Soni. Laser-generated bimetallic Ag-Au and Ag-Cu core-shell nanoparticles for refractive index sensing. *Plasmonics*, 10(3):681–690, Jun 2015.
- [198] Lili Feng, Guo Gao, Peng Huang, Kan Wang, Xiansong Wang, Teng Luo, and Chunlei Zhang. Optical properties and catalytic activity of bimetallic gold-silver nanoparticles. 2, 12 2010.
- [199] Xuejuan Yang, Yinhu Wang, Yuwei Liu, and Xiue Jiang. A sensitive hydrogen peroxide and glucose biosensor based on gold/silver core-shell nanorods. *Electrochimica Acta*, 108(Supplement C):39 – 44, 2013.
- [200] Carlos Campos-Cuerva, Maciej Zieba, Victor Sebastian, Gema Mart  nez, Javier Sese, Silvia Irusta, Vicente Contamina, Manuel Arruebo, and Jesus Santamaria. Screen-printed nanoparticles as anti-counterfeiting tags. *Nanotechnology*, 27(9):095702, 2016.
- [201] Emma Westsson and Ger J.M. Koper. How to determine the core-shell nature in bimetallic catalyst particles? *Catalysts*, 4:375–396, 2014.
- [202] L Rivas, S Sanchez-Cortes, Jos   Garc  a-Ramos, and Gloria Morcillo. Mixed silver/gold colloids: a study of their formation, morphology, and surface-enhanced raman activity. 16, 11 2000.
- [203] Kaushik Mallick, Madhuri Mandal, Narayan Pradhan, and Tarasankar Pal. Seed mediated formation of bimetallic nanoparticles by UV irradiation: A photochemical approach for the preparation of "core-shell" type structures. 1:319–322, 06 2001.
- [204] Lingxuan Peng, Emilie Ringe, Richard P. Van Duyne, and Laurence D. Marks. Segregation in bimetallic nanoparticles. *Phys. Chem. Chem. Phys.*, 17:27940–27951, 2015.
- [205] Gr  gory Guisbiers, Rub  n Mendoza-Cruz, Lourdes Baz  n-D  az, J. Jes  s Vel  zquez-Salazar, Rafael Mendoza-Perez, Jos   Antonio Robledo-Torres, Jos  -Luis Rodr  guez-Lopez, Juan Mart  n Montejano-Carrizales, Robert L. Whetten, and Miguel Jos  -Yacam  n. Epectrum, the gold  silver alloy, from the bulk scale to the nanoscale: Synthesis, properties, and segregation rules. *ACS Nano*, 10(1):188–198, 2016. PMID: 26605557.
- [206] Eirini Goudeli and Sotiris E. Pratsinis. Surface composition and crystallinity of coalescing silver-gold nanoparticles. *ACS Nano*, 0(0):null, 0. PMID: 29112816.

- [207] Paul A. DeSario, Jeremy J. Pietron, Devyn E. DeVantier, Todd H. Brintlinger, Rhonda M. Stroud, and Debra R. Rolison. Plasmonic enhancement of visible-light water splitting with Au-TiO<sub>2</sub> composite aerogels. *Nanoscale*, 5:8073–8083, 2013.
- [208] Kwanghyun Kim, Pradheep Thiyagarajan, Hyo-Jin Ahn, Sun-I Kim, and Ji-Hyun Jang. Optimization for visible light photocatalytic water splitting: gold-coated and surface-textured TiO<sub>2</sub> inverse opal nano-networks. *Nanoscale*, 5:6254–6260, 2013.
- [209] Timur Sh. Atabaev. The effects of gold nanoparticles deposition on the surface of TiO<sub>2</sub> nanorods for solar water splitting applications. *Nano LIFE*, 06(01):1650004, 2016.
- [210] Kshirodra K. Patra and Chinnakonda S. Gopinath. Bimetallic and plasmonic Ag-Au on TiO<sub>2</sub> for solar water splitting: An active nanocomposite for entire visible-light-region absorption. *ChemCatChem*, 8(20):3294–3311, 2016.
- [211] Yiqun Yang, Judy Wu, and Jun Li. Correlation of the plasmon-enhanced photoconductance and photovoltaic properties of core-shell Au@TiO<sub>2</sub> network. *Appl. Phys. Lett.*, 109, 2016.
- [212] Yang Wang, Jin Zhai, and Yanlin Song. Plasmonic cooperation effect of metal nanomaterials at Au-TiO<sub>2</sub>-Ag interface to enhance photovoltaic performance for dye-sensitized solar cells. *RSC Adv.*, 5:210–214, 2015.
- [213] Run Long and Oleg V Prezhdo. Instantaneous generation of charge-separated state on TiO<sub>2</sub> surface sensitized with plasmonic nanoparticles. *Journal of the American Chemical Society*, 136(11):4343–4354, 2014. PMID: 24568726.
- [214] Vincenzo Amendola, Roberto Pilot, Marco Frascioni, Onofrio M Maragò, and Maria Antonia Iati. Surface plasmon resonance in gold nanoparticles: a review. *Journal of Physics: Condensed Matter*, 29(20):203002, 2017.
- [215] Lufsyi Mahmudin, Edi Suharyadi, Agung Bambang Setio Utomo, and Kamsul Abraha. Optical properties of silver nanoparticles for surface plasmon resonance (spr)-based biosensor applications. *Journal of Modern Physics*, 6(8):1071–1076, 2015.
- [216] Saji Thomas Kochuveedu. Photocatalytic and photoelectrochemical water splitting on tio2 via photosensitization. *Journal of Nanomaterials*, 2016:12, 2016.
- [217] Mark Brongersma, Naomi Halas, and Peter Nordlander. Plasmon-induced hot carrier science and technology. 10:25–34, 01 2015.
- [218] Alejandro Manjavacas, Jun G. Liu, Vikram Kulkarni, and Peter Nordlander. Plasmon-induced hot carriers in metallic nanoparticles. *ACS Nano*, 8(8):7630–7638, 2014. PMID: 24960573.
- [219] Scott K. Cushing, Jiangtian Li, Joeseeph Bright, Brandon T. Yost, Peng Zheng, Alan D. Bristow, and Nianqiang Wu. Controlling plasmon-induced resonance energy transfer and hot electron injection processes in metal@TiO<sub>2</sub> core-shell nanoparticles. *The Journal of Physical Chemistry C*, 119(28):16239–16244, 2015.
- [220] Kazutaka Akiyoshi, Koichiro Saito, and Tetsu Tatsuma. Enhancement of plasmon-induced charge separation efficiency by coupling silver nanocubes with a thin gold film. *Journal of Photonics for Energy*, 6(4):042505, 2016.

- [221] Ying-Chih Pu, Gongming Wang, Kao-Der Chang, Yichuan Ling, Yin-Kai Lin, Bob C. Fitzmorris, Chia-Ming Liu, Xihong Lu, Yexiang Tong, Jin Z. Zhang, Yung-Jung Hsu, and Yat Li. Au nanostructure-decorated TiO<sub>2</sub> nanowires exhibiting photoactivity across entire UV-visible region for photoelectrochemical water splitting. *Nano Letters*, 13(8):3817–3823, 2013. PMID: 23899318.
- [222] Liangbin Xiong, Jia-Lin Li, Bo Yang, and Ying Yu. Ti<sup>3+</sup> in the surface of titanium dioxide: Generation, properties and photocatalytic application. 2012, 01 2012.
- [223] Yoshiaki Nishijima, Kosei Ueno, Yuki Kotake, Kei Murakoshi, Haruo Inoue, and Hiroaki Misawa. Near-infrared plasmon-assisted water oxidation. *The Journal of Physical Chemistry Letters*, 3(10):1248–1252, 2012. PMID: 26286766.
- [224] Alexander O. Govorov, Hui Zhang, and Yurii K. Gun'ko. Theory of photoinjection of hot plasmonic carriers from metal nanostructures into semiconductors and surface molecules. *The Journal of Physical Chemistry C*, 117(32):16616–16631, 2013.
- [225] Nobuhiro Fuke, Atsushi Fukui, Ashraful Islam, Ryoichi Komiya, Ryohsuke Yamanaka, Hiroshi Harima, and Liyuan Han. Influence of TiO<sub>2</sub>/electrode interface on electron transport properties in back contact dye-sensitized solar cells. *Solar Energy Materials and Solar Cells*, 93(6):720 – 724, 2009. 17th International Photovoltaic Science and Engineering Conference.
- [226] Ovidio Pena-Rodriguez and Umapada Pal. Au@Ag core-shell nanoparticles: efficient all-plasmonic fano-resonance generators. *Nanoscale*, 3:3609–3612, 2011.
- [227] Su Pei Lim, Yee Seng Lim, Alagarsamy Pandikumar, Hong Ngee Lim, Yun Hau Ng, Ramasamy Ramaraj, Daniel Chia Sheng Bien, Osama K. Abou-Zied, and Nay Ming Huang. Gold-silver@TiO<sub>2</sub> nanocomposite-modified plasmonic photoanodes for higher efficiency dye-sensitized solar cells. *Phys. Chem. Chem. Phys.*, 19:1395–1407, 2017.
- [228] J. L. Wang, Romulo A. Ando, and Pedro H. C. Camargo. Investigating the plasmon-mediated catalytic activity of AgAu nanoparticles as a function of composition: Are two metals better than one? *ACS Catalysis*, 4(11):3815–3819, 2014.
- [229] Marco Serra, Josep Albero, and Hermenegildo García. Photocatalytic activity of Au/TiO<sub>2</sub> photocatalysts for H<sub>2</sub> evolution: Role of the Au nanoparticles as a function of the irradiation wavelength. *ChemPhysChem*, 16(9):1842–1845, 2015.
- [230] Jeffrey Chi-Sheng Wu, Jiun-Jen Chen, Pin Chieh Wu, and Tsai; Din Ping. Plasmon-enhanced photolysis of water for hydrogen production. *SPIE*, page 1, 2012.
- [231] Lorcan J . Brennan, Finn Purcell-Milton, Aurélien S Salmeron, Hui Zhang, Alexander O Govorov, Anatoly V. Fedorov, and Yurii K. Gun'ko. Hot plasmonic electrons for generation of enhanced photocurrent in gold-TiO<sub>2</sub> nanocomposites. In *Nanoscale research letters*, 2015.
- [232] Yang Yu, Wei Wen, Xin-Yue Qian, Jia-Bin Liu, and Jin-Ming Wu. Uv and visible light photocatalytic activity of Au/TiO<sub>2</sub> nanoforests with anatase/rutile phase junctions and controlled au locations. *Scientific Reports*, 7:41253, 2017.
- [233] Liping Liu, Gongming Wang, Yat Li, Yadong Li, and Jin Z. Zhang. CdSe quantum dot-sensitized Au/TiO<sub>2</sub> hybrid mesoporous films and their enhanced photoelectrochemical performance. *Nano Research*, 4(3):249–258, Mar 2011.



- [234] Milena Jankulovska, Thomas Berger, Stanislaus S. Wong, Roberto Gómez, and Teresa Lana-Villarreal. Trap states in  $\text{TiO}_2$  films made of nanowires, nanotubes or nanoparticles: An electrochemical study. *ChemPhysChem*, 13(12):3008–3017, 2012.
- [235] Jun heng XING, Zheng bin XIA, Hui LI, Ying ying WANG, and Li ZHONG. Growth and crystallization behaviors of anodic oxide films on sputter-deposited titanium at very low potentials. *Transactions of Nonferrous Metals Society of China*, 23(11):3286 – 3292, 2013.
- [236] Thomas Berger, Teresa Lana-Villarreal, Damián Monllor-Satoca, and Roberto Gómez. An electrochemical study on the nature of trap states in nanocrystalline rutile thin films. *The Journal of Physical Chemistry C*, 111(27):9936–9942, 2007.
- [237] Christian Worsch, Michael Kracker, Wolfgang Wisniewski, and Christian Rüssel. Optical properties of self assembled oriented island evolution of ultra-thin gold layers. *Thin Solid Films*, 520(15):4941 – 4946, 2012.
- [238] Alexander B. Tesler, Lev Chuntonov, Tanya Karakouz, Tatyana A. Bendikov, Gilad Haran, Alexander Vaskevich, and Israel Rubinstein. Tunable localized plasmon transducers prepared by thermal dewetting of percolated evaporated gold films. *The Journal of Physical Chemistry C*, 115(50):24642–24652, 2011.

### 9.0.7 Uniformity and reproducibility of metal deposition

The basic requirement for a reliable preparation is a homogenous and reproducible deposition. Au was sputtered on a glass sample and a height profile was measured to evaluate the thickness uniformity of the deposition (figure 9.1). An average thickness of 62 nm with a standard variation of 9 nm (15 %) was measured indicating a homogenous spatial deposition which suggests a good uniformity. Nevertheless, the height profile shows two maxima with a separation distance of 2.5 cm. This peak structure appears because the magnetron acts like a ring source [92] with a nearly homogenous deposition at the center. An increase in magnetron-sample distance would attenuate the peak structure but also prevent efficient utilization and waste target material. The baseline is tilted which could indicate that the substrate holder and the target surface is not exactly parallel. All samples in this work have dimensions equal or smaller than 25 mm so that a uniformly thick layer is expected when they are placed in the identified area.

The layer thickness was controlled by variation of the sputter time through knowledge of the deposition rate (amount of film deposition per sputter time). A sufficiently high sputter time was achieved by placing a 1 mm thick iron disc between the sputter target and the magnetron. The ferromagnetic iron reduced the magnetic field strength from the magnetron near the target surface. Sputter rates calculated from the profilometer data are plotted in figure 9.2. A mean sputtering yield of 22 pm/s with a standard variation of 6 pm/s was obtained for Au deposition and 71 pm/s with a standard variation of 3 pm/s for Ag. This suggested a homogenous and reproducible film deposition provided by magnetron sputtering.

### 9.0.8 Particle sizes of annealed Au (6.6 nm, 1)

After annealing of a 6.6 nm thick Au layer irregular nanostructures transform to isolated particles with diameters between 5-69nm (figure 9.3).

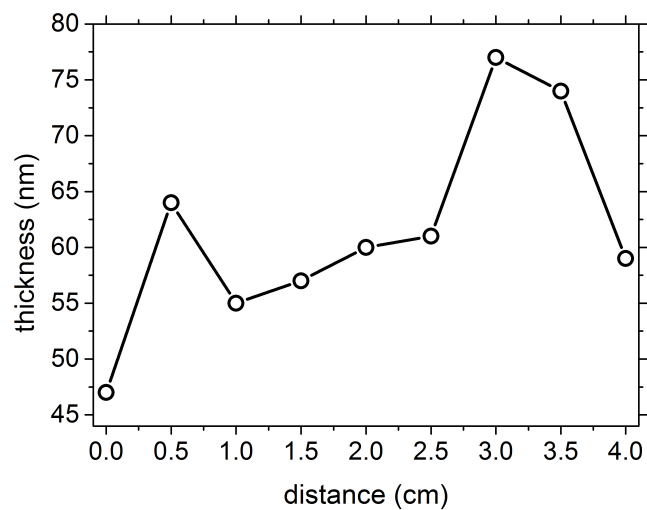


**Figure 9.1:** Profilometer line scan showed that a uniformly thick Au deposition is expected if the sample is placed in the center between position 1.0 cm and 2.5 cm.

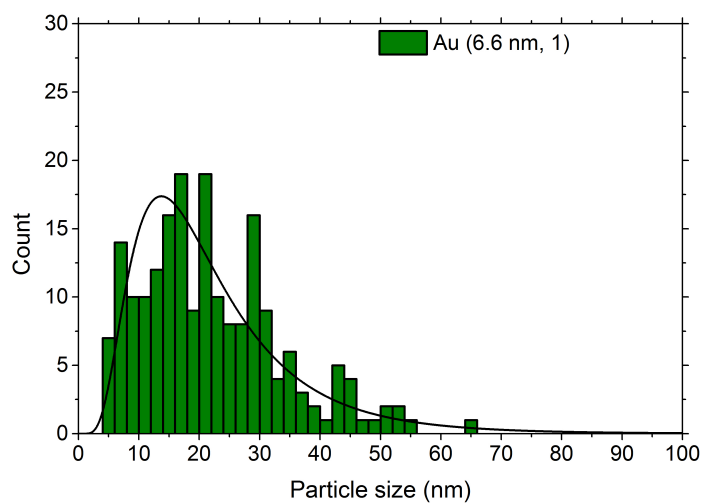
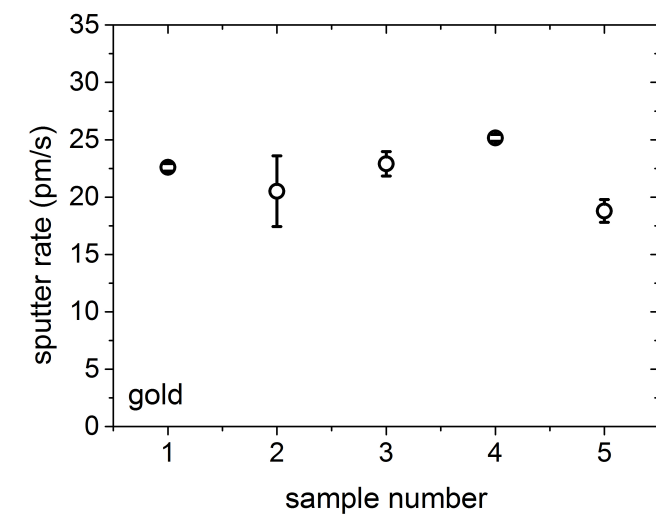
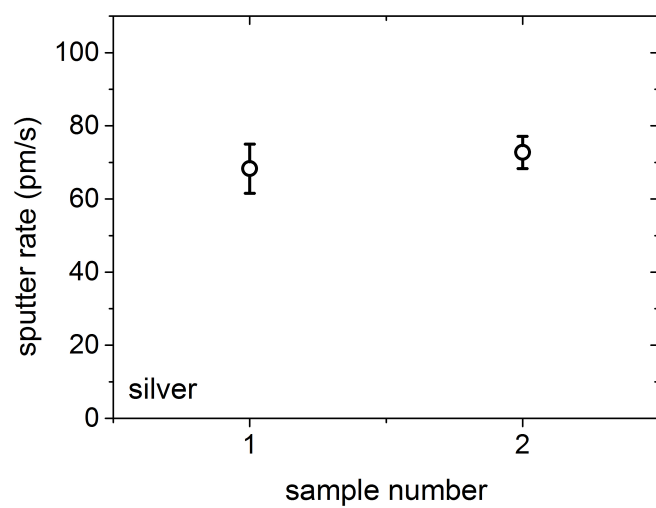


**Figure 9.3:** Particle Size distribution determined from SEM images shown in 6.3a. The number of pixels for 200 nanoparticles were counted and their distribution fitted by a lognormal distribution.



(a)



(b)

**Figure 9.2:** A sputter rate mean value of 22.0 pm/s with a standard deviation of 5.8 pm/s (26%) for Au (a) and of 71 pm/s with a standard deviation of 3.1 pm/s (4 %) for Ag (b) suggested a reproducible film deposition by magnetron sputtering.

### 9.0.9 Reproducibility of LSPR peak position in UV-vis

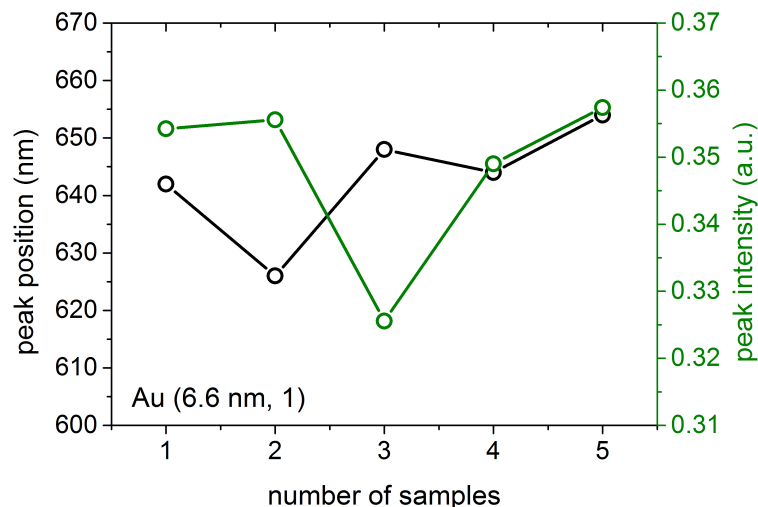


**Figure 9.4:** Reproducibility for Au (6.6 nm, 1) nanoparticles preparation method.

The scattering of absorbance peak maxima data served as an estimation for the reproducibility of the optical properties. For the analysis, the absorbance was calculated from the recorded diffuse transmission according to the equation 5.2, the data was smoothed (moving average) and the null of the first derivative was determined. The average LSPR peak of five identical preparation protocols were found at 642.8 nm with a standard deviation of  $\pm 10$  nm and an intensity of 0.35  $\text{nm} \pm 0.01$  nm, respectively. The standard deviation was consecutively used as an error bar in figure 6.10 in the main text and figure 9.5 in the appendix.

### 9.0.10 Variation in thermal annealing: transverse excitation

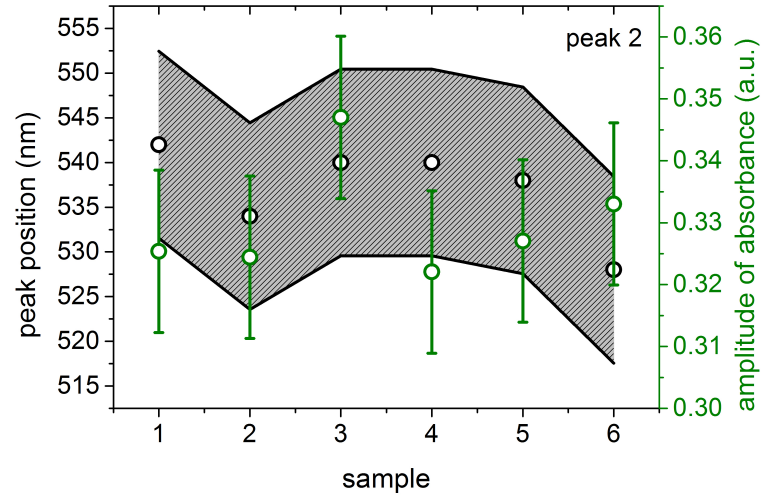


**Figure 9.5:** LSPR peak position of the transvers mode extracted from figure 6.10 in the main text. The added standard error shows that they are comparable in relation to the experimental error.

Beside the red-shifted longitudinal peak shown in the main text, there is also a subtil peak at approximatively 540 nm. The position of this peak maximum for different annealing parameters lies in the region of experimental error.

### 9.0.11 Modulation in XRD

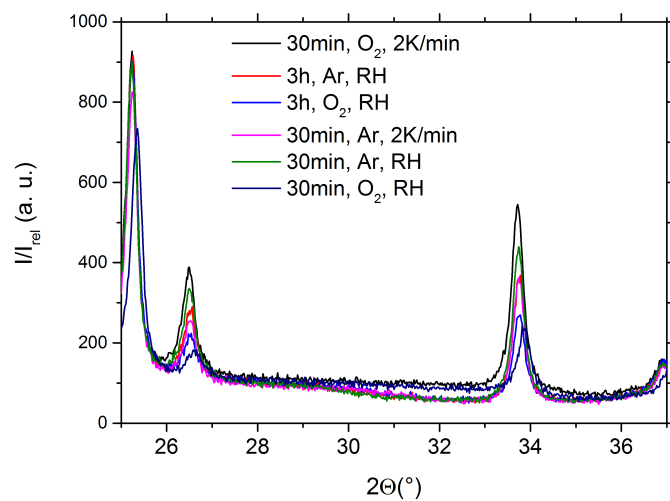


**Figure 9.6:** The XRD diffraction showed a background modulation for 30 min oxygen 2 K/min and 30 min oxygen RH

The XRD diffraction of 30 min oxygen 2 K/min and 30 min oxygen RH showed a background modulation between  $29^\circ 2\theta$  and the reflex at  $33.8^\circ 2\theta_{diff}$ .

### 9.0.12 Ag nanoparticle formation

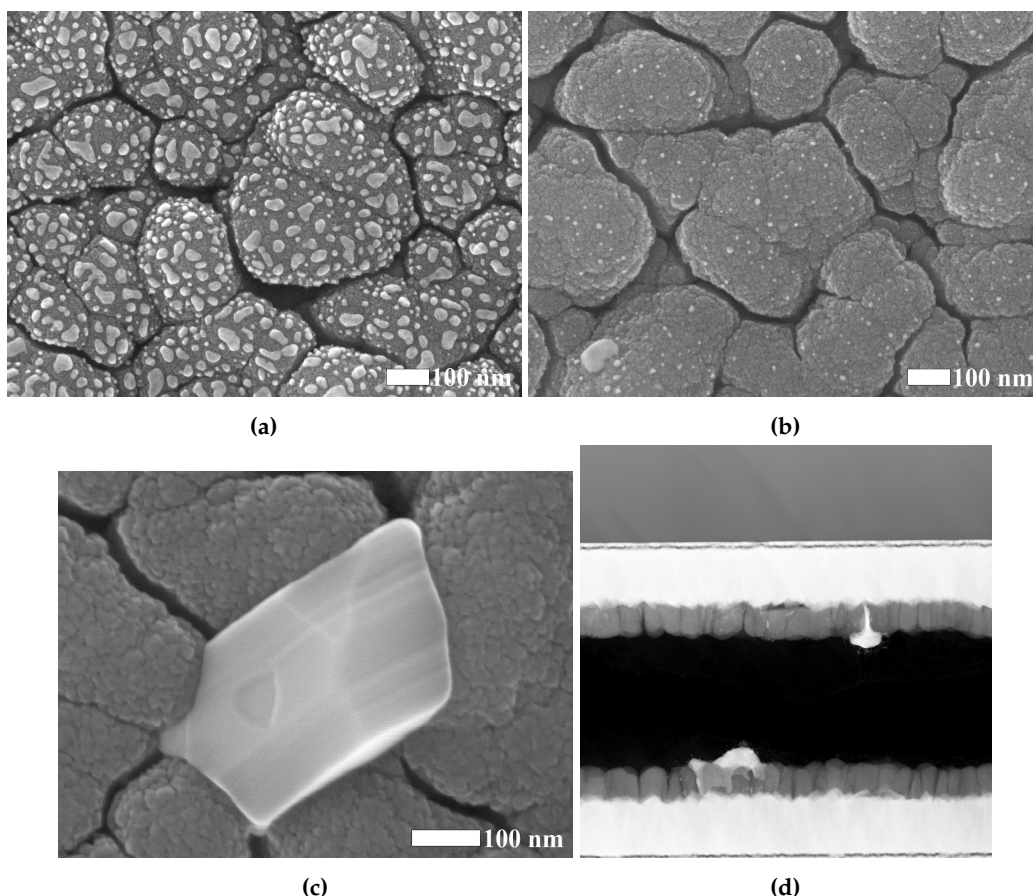


**Figure 9.7:** SEM images showing the effect of thermal annealing on a Ag layer with a nominal thickness of  $4.3 \text{ nm} \pm 0.2 \text{ nm}$ . Figure (a) shows that the as-sputtered Ag layer already forming isolated nanoparticles (140616A Ag 60s). After annealing at  $200^\circ\text{C}$  in for 30 min in oxygen a reduction in particle size and metal loading detected on the TiO<sub>2</sub> surface was observed (140605A Ag 60 s  $200^\circ\text{C}$ , figure (b)). The formation of large Ag crystals that appear to migrate into the inter-columnar space can be seen in Figure (c). The sample was annealed at  $400^\circ\text{C}$  for 30 min in air. Finally, a HRTEM cross section of a preparation similar to (b) revealed large Ag agglomeration partially located deeply between the columns.

The introduction of Ag to the Au nano-particle system posed challenges for its preparation. An as-sputtered Ag deposition with a nominal layer thickness of  $4.3 \text{ nm} \pm 0.2 \text{ nm}$  immediately forms isolated nanoparticles as is indicated by SEM images (figure 9.7a). However, thermal annealing at  $200^\circ\text{C}$  in oxygen resulted in a drastic decrease in particle size, density and number and a significant reduction of metal present at the surface (Figure 9.7b). Another sample prepared at  $400^\circ\text{C}$  in air shows a large faceted Ag agglomeration located between TiO<sub>2</sub> columns (figure 9.7c) and TEM images of a cross section (similar to preparation in figure 9.7d) confirms filling of voids between the TiO<sub>2</sub> columns with Ag protruding til the FTO substrate. This suggest that Ag is highly mobile (as reported for fcc metals [101]) upon annealing and starts to coalescence to large agglomerations. The small nanoparticles seen in figure 9.7b are likely pinned nanoclusters that are immobilized due to surface diffusion barriers of the titania. The filling of the inter-columnar



voids are probably driven by capillary effects. This indicates the difficulty of Ag dewetting while using a highly structured and void containing substrate.

### 9.0.13 UV-vis spectra of Ag nanoparticles

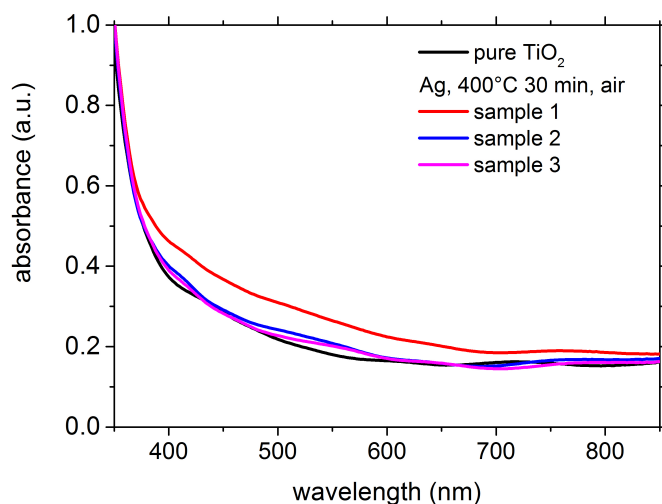


**Figure 9.8:** The UV-vis spectra showed different adsorbance intensities for annealing of thin Ag layers at 400°C for 30 min in air.

The UV-Vis spectra compared Ag/TiO<sub>2</sub> prepared with the same protocol of thermal annealing of a Ag layer with a nominal layer thickness of 4.3 nm ± 0.2 nm at 400°C for 30 min in air. The differences in absorbance intensity is related to deviations in nanoparticle formation. The UV-vis spectra suggested that Ag intruded into the voids between the TiO<sub>2</sub> columns for sample 2 and 3.

### 9.0.14 Optical properties of TiO<sub>2</sub>

The UV-Vis spectra of TiO<sub>2</sub> (anatase) layers deposited on FTO@glass by different methods and used as support for nanoparticles decoration are presented in figure 9.9. They all showed a strong increase in intensity below 400 nm which was expected from the band gap of the anatase and a non-zero absorbance due to scattering or mind-band gap states. The spectra of a 200 nm thick highly porous layer was comparable to the absorbance found for DC sputtered 270 nm substrate. The AP-CVD TiO<sub>2</sub> gained in intensity with increasing layer thickness and seemed to convert towards a limit.

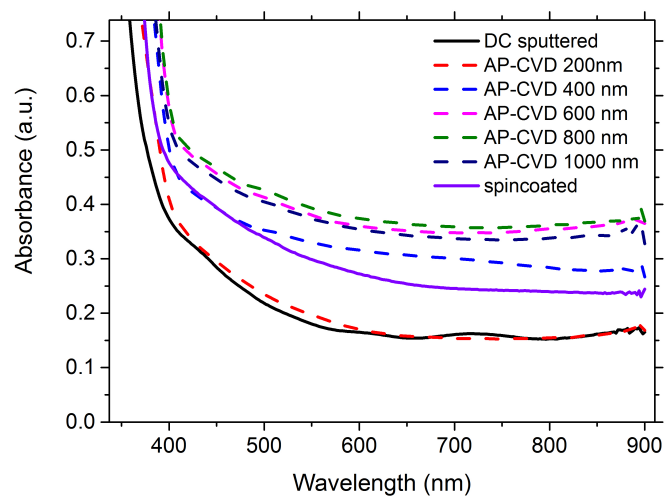


**Figure 9.9:** Overview of the absorbance spectra for the  $\text{TiO}_2$  (anatase)@FTO@glass substrates used in this work (sputtered, spincoated and highly porous). They are calculated from diffuse transmission data. The absorbance for highly porous  $\text{TiO}_2$  with thicknesses from 200 nm to 1000 nm are indicated by broken lines for clarity.

### 9.0.15 Cyclic voltammetry of DC sputtered $\text{TiO}_2$

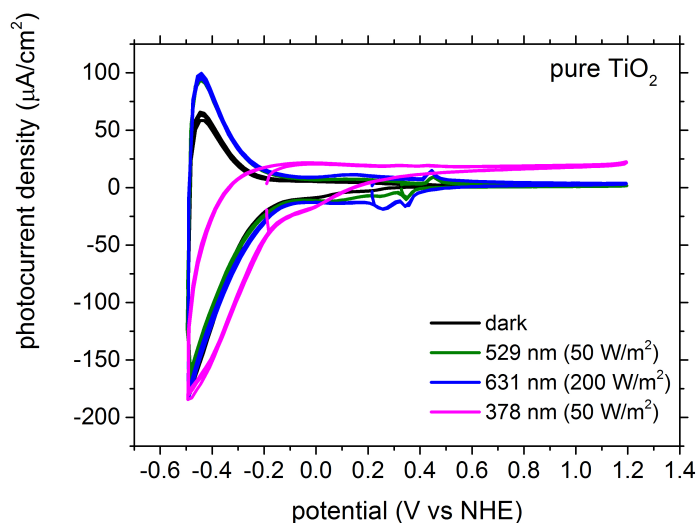


**Figure 9.10:** Pure DC sputtered  $\text{TiO}_2$  showed two peaks in cyclic voltammetry with an onset of 0.38 V vs NHE in the cathodic sweep and 0.4 V vs NHE in the anodic sweep that could be due to defect states in the band gap.

This cyclic voltammetry measurement of DC sputtered  $\text{TiO}_2$  showed the photocurrent density response of the sample during sweeping of the potential. An accumulation region with an onset of -0.1 V vs NHE appeared where the electrode became conductive [234]. The photocurrent double-peak with an onset at 0.38 V vs NHE in the cathodic sweep and 0.4 V vs NHE in the anodic sweep were observed both in pure DC sputtered  $\text{TiO}_2$  and metal loaded titania. They could indicate reduction and oxidation reaction on the semiconductor surface, respectively. The use of a  $\text{Na}_2\text{SO}_4$  electrolyte suggested adsorption of sulphate on the semiconductor surface. However, a study conducted on the characterization of  $\text{TiO}_2$  with  $\text{H}_2\text{SO}_4$  did not show comparable reduction and oxidation peaks in CV measurements [235]. Kenanakis et al. observed sodium intercalation in the  $\text{TiO}_2$  at a cathodic onset of -750 mV vs Ag/AgCl that is also not applicable to our sample [159]. The most plausible explanation for these increased photocurrents is the filling and refilling of electron trap states at the interface between  $\text{TiO}_2$  grain boundaries and the electrolyte. Energetically, these trap states lie in the band gap of the semiconductor. These capacitive peaks are characteristic for nanoparticulate electrodes [236] and therefore indicate the existence of defect states in the band gap of DC sputtered  $\text{TiO}_2$  that are able to trap electrons.

### 9.0.16 Reflectivity of Au nanoparticles

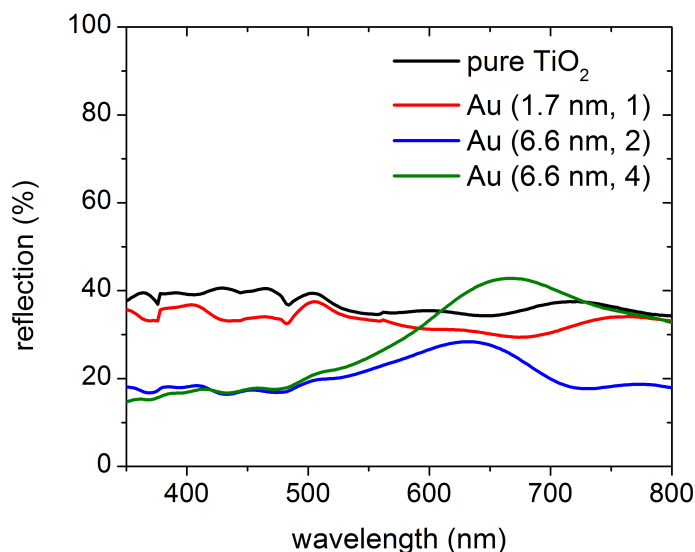


**Figure 9.11:** The reflectivity above 550 nm increased with increasing Au loading.

Figure 9.11 compares the reflectivity of three Au- $\text{TiO}_2$  samples having different nanoparticle sizes. For wavelengths shorter than 550 nm, Au nanoparticles decorated samples reflected less than the pure  $\text{TiO}_2$  with Au (6.6 nm, 2) and Au (6.6 nm, 4) size particles having the lowest and nearly equal reflection. For longer wavelengths, Au (1.7 nm, 1) nanoparticles merely showed a red shift for the reflection maxima seen in the  $\text{TiO}_2$ . With increasing Au deposition, a reflection maximum between 550 nm and 730 nm seemed to have evolved that increases the reflectivity of Au (6.6 nm, 4) particle deposition compared to the pure  $\text{TiO}_2$ .

Both Au (1.7 nm, 1) and Au (6.6 nm, 2) nanoparticles exhibited a lower reflection than pure TiO<sub>2</sub>. This is in accordance with Worsch et al and Tesler et al who observed no significant light scattering for Au nanoparticles below 40nm [237][238]. A dominant scattering is expected for particles above 200 nm that give rise to strong red-shift and peak broadening [238].

### 9.0.17 UV-vis absorbance of Au/AP-CVD TiO<sub>2</sub>

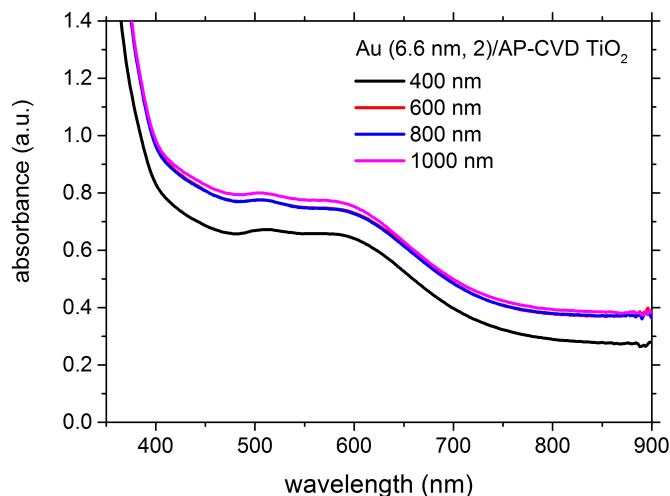


**Figure 9.12:** Absorbance of Au/AP-CVD TiO<sub>2</sub> with titania layer thicknesses of 400 nm, 600 nm, 800 nm and 1000 nm.

The UV-vis spectra of Au (6.6 nm, 2)/AP-CVD TiO<sub>2</sub> for titania layer thicknesses of 400 nm, 600 nm, 800 nm and 1000 nm showed a transverse LSPR 490 nm and 550 nm and the formation of a longitudinal peak between 550 nm and 750 nm. The separation between the transverse and longitudinal resonances is lower than for Au (6.6 nm, 2) on DC sputtered TiO<sub>2</sub>, which indicates that the nanoparticles in this system have a lower aspect ratio than the nanoparticles on the DC sputtered TiO<sub>2</sub>.

### 9.0.18 Stability of sample surface

A PEC cell and a 0.1 M Na<sub>2</sub>SO<sub>4</sub> electrolyt were used for photoelectrochemical characterization of nanoparticle-TiO<sub>2</sub> systems and results of anodic photocurrent measurements are discussed in the following paragraphs. However, comparing the optical appearance of the samples before and after photoelectrochemical measurements suggest changes in the material surface, that is in direct contact with the electrolyt and illuminated (figure 9.13). SEM images from four different areas on a measured Au (6.6 nm, 2)-TiO<sub>2</sub> sample indicate that nanoparticles agglomerate on the TiO<sub>2</sub> surface (figure 9.14) and can form porous nanostructures with diameters of 200 to 300 nm.

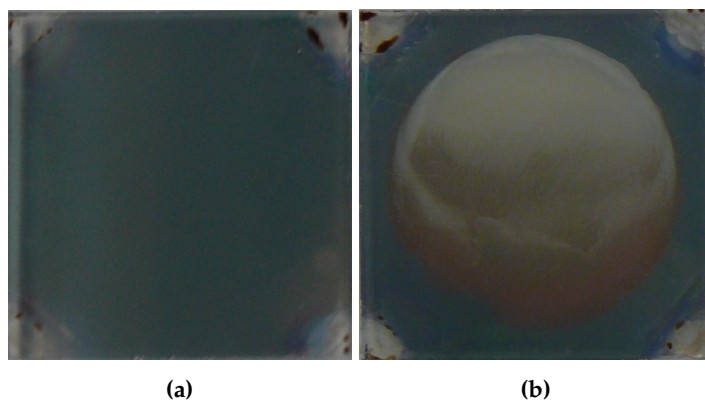


**Figure 9.13:** Foto of Au (6.6 nm, 2)-TiO<sub>2</sub> sample before (left side) and after photoelectrochemical measurements (right side) suggest a change of surface properties during electrochemical measurements. The corners were omitted from TiO<sub>2</sub> deposition to ensure contact with the conductive FTO. The circular spot of differing colour visible after measurements correlates with the area in contact with the electrolyte. The samples have side diameter of 25 mm.

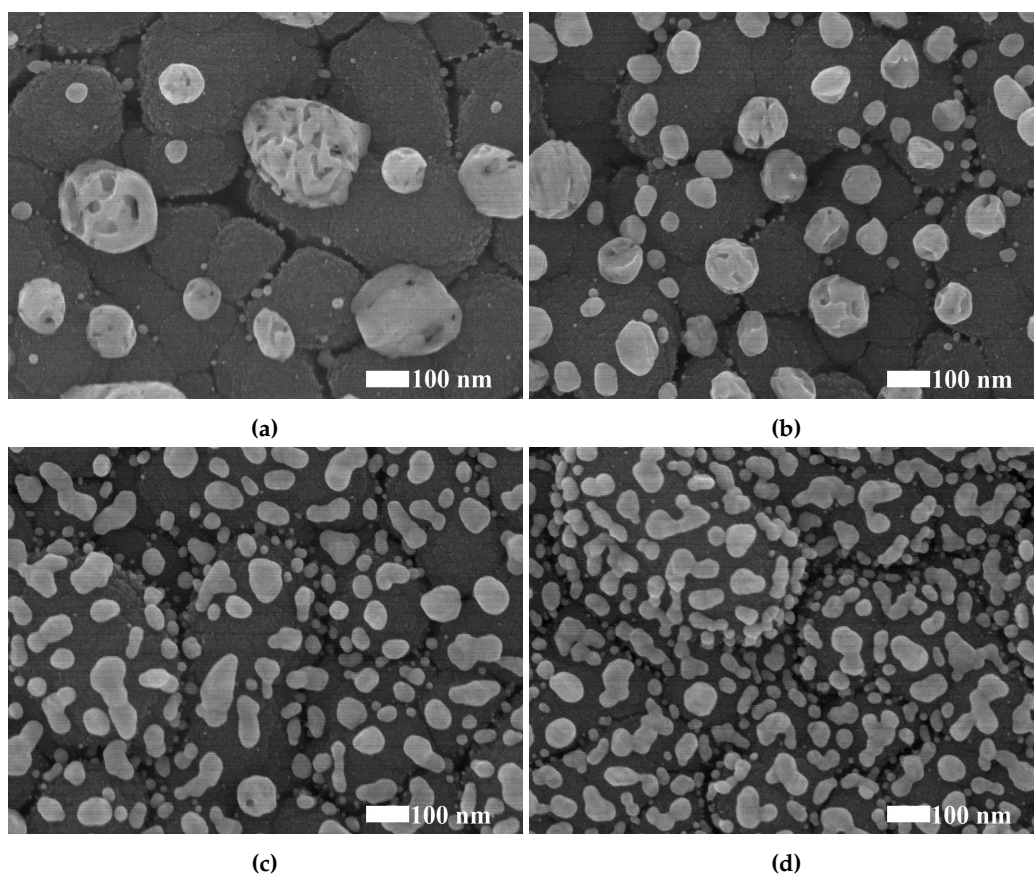


**Figure 9.14:** SEM from a Au (6.6 nm, 2) nanoparticle sample after photoelectrochemical measurements showed agglomeration. The images show four positions on the same sample.

The particle agglomeration time could not be determined in the experiment which allows only for a cautious property-activity correlation in hindsight. However, the experiments were performed under the same protocol which should allow to draw comparative conclusions between the samples. Moreover, the detected photocurrents were stable (appendix fig 9.17).

### 9.0.19 Incident photon-to-current efficiency

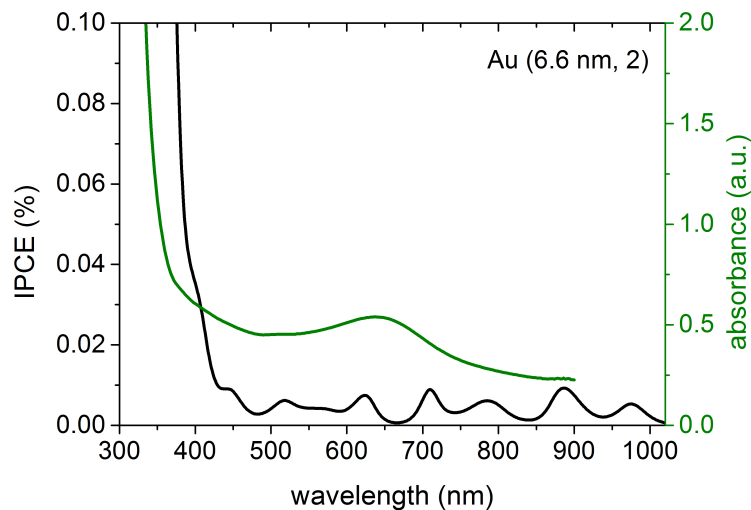


**Figure 9.15:** No photocurrent enhancement at visible wavelengths which could be due to too low light source intensity.

The IPCE in figure 9.15 of Au (6.6 nm, 2) nanoparticles did not show an enhancement between 550-750 nm as would be expected from plasmon-induced charge generation. The tunable TLS03 light source consisted of 23 LEDs and had an intensity of  $1 \text{ W/m}^2$  so that a more suitable high-intensity source is needed for further investigation.

### 9.0.20 SEM of Au decorated spincoated $\text{TiO}_2$

Similar to visible light at 529 nm, Au loading on spincoated  $\text{TiO}_2$  decreased the photocurrent at a broader light illumination. Au (6.6 nm, 1) nanoparticles showed the lowest photocurrent whereas Au (6.6 nm, 2) nanoparticles had the highest.



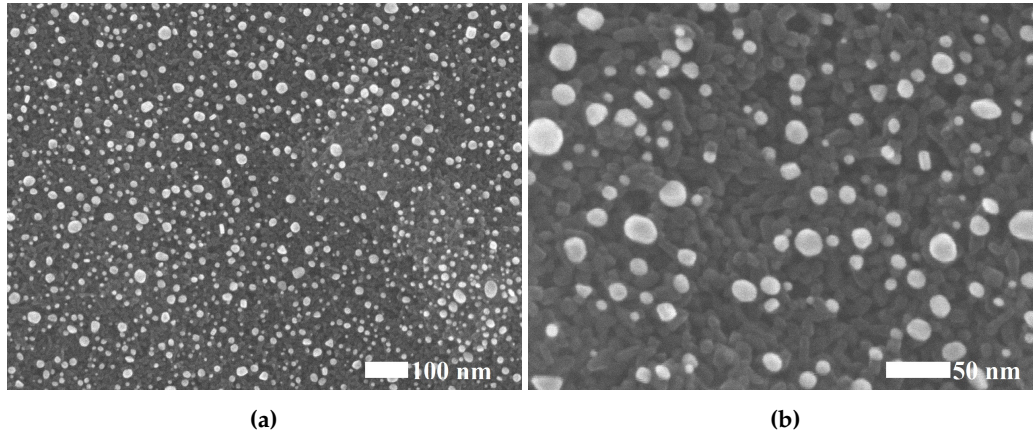


**Figure 9.16:** SEM top view on a Au-TiO<sub>2</sub> composite. Au (1.7 nm, 1) nanoparticles were deposited between subsequent TiO<sub>2</sub> layers forming a Au-TiO<sub>2</sub>-Au-TiO<sub>2</sub>-Au-TiO<sub>2</sub>-FTO-Glas sample.

### 9.0.21 Stability of photocurrent density

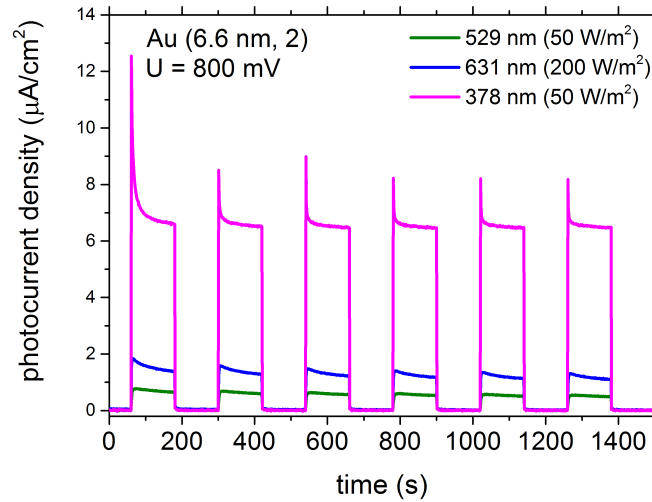


**Figure 9.17:** The Photocurrent density measured for Au (6.6 nm, 2) nanoparticles are stable for six on/off cycles independent of the illumination wavelength. For UV light of 378 nm the photocurrent density showed an overshoot at the beginning of the "on"-cycle.

The photocurrent density of a Au (6.6 nm, 2)/TiO<sub>2</sub> sample was stable for six consecutive on/off cycles. Under UV light, there are initial overshoots in the photocurrent density. The TiO<sub>2</sub> generates electrons and holes upon UV illumination that leads to the initial rise in photocurrent density. If the charge transfer is slow, the photo-generated electrons and holes will partially recombine, which results in a decrease of measured photocurrent density until an equilibrium is reached.